CHARACTERIZATION OF THERMO-FLUID TRANSPORT PROPERTIES OF COATED AND UNCOATED OPEN-CELL METAL FOAM MONOLITHS

by

Edward Anthony Thomas

A thesis submitted to the Department of Chemical Engineering

In conformity with the requirements for

the degree of Master of Applied Science

Queen's University

Kingston, Ontario, Canada

(December, 2011)

Abstract

An improved steady-state method combining experiment and mathematical modelling has been developed to characterize the scalable convective heat transfer coefficient, h_{vol} $\left(W \cdot m^{-3} \cdot K^{-1}\right)$, of uncoated and catalyst-support coated aluminium foam monoliths. The values of h_{vol} were recovered by parameter fitting its model values to experimental temperature data for steady-state air-cooled monoliths under a known heating flux. The model was built with experimentally recovered values of the monolith's thermal conductivity and fluid permeability along with known values for other physical parameters. The volumetric heat transfer coefficients of 10, 20 and 40 pore-per-inch uncoated aluminium foams were determined to range between 2,700 and 20,000 $W \cdot m^{-3} \cdot K^{-1}$ at channel Reynolds numbers between 85 and 1,700. The presence of a 76 micron-thick anodized layer of catalyst support on monolith foams effected a small but significant reduction in the value of h_{vol}. Coating with an anodized layer also reduced the permeabilities of the monoliths to air flow by 4-20%. Knowledge of the scalable parameter, h_{vol}, was used to model a steady-state non-isothermal, non-isobaric heat-coupled methanol reformer. The model shows that changes to the convective transfer coefficient due to coating the monolith with catalyst support may have significant consequences for the thermal profile of the model reactor and for the product yield.

Acknowledgements

In 2002 I left my career in business journalism to take an engineering degree. One thing led to another and in 2010, I submitted a masters thesis in chemical engineering. Thus far, my journey in higher education has been a great thrill and I have some important people to thank.

First my supervisor, Dr. Kunal Karan, for his willingness to embark on what turned out to be a rather open-ended problem in reactor modelling. Dr. Karan has always encouraged curiosity and (dare I say) fearlessness in tackling less-than-straightforward problems. Thank you.

My many colleagues and labmates over the years: Dr. Ben Kenny, my chief instigator and co-adventurer in sustainable energy research; your infectious zeal to try new challenges was more powerful than coffee. Craig Baker and Manny Resch who rounded out my community of numerical modelling sluggos; your ability to keep it fun through ridiculous loads of work is greatly appreciated. Dr. Misha Monder; you really helped me through a tricky modelling problem. My undergraduate research fellows 1) Jonas Gerson, you are my model engineer – persistent, creative and unfailingly undeterred. 2) Geoff Gates; thanks for letting the old man keep up with you on Highway 33. 3) Brandon Parsons; thanks for your willingness to try a few disparate things in the early going – it's the things that don't pan out that help us figure out where we need to go. To the rest of the gang who've shared my time at Queen's-RMC Fuel Cell Research Centre: Barbra Brousseau, Jason Wood, Rajesh Parmar, Adegboyega Babasola, Rajender Reddi, Dr. Jon Pharoah, Dr. Brant Peppley, Dr. Chris Thurgood, Andrea Van Bruinessen, Mike Lankin, Akit Gadi, Daniel Calabretta, Jan De Bakker, Alex Davis, Mohamed Abdul, Flora Lo, David Castagne, Brian Tysoe, Mark Van Doormaal, Adam St. John, Adam Shaw – thanks for making the whole thing a lot of fun.

And finally, the two most important people in my life. My mother, Gail, who fiercely championed my education and gave me a reason to get started on this thesis. My wife, Ingrid, the love of my life who believes in me, supports me and gave me a reason to finish what I started.

Table of Contents

Abstract ii
Acknowledgements iii
Table of Contents iv
List of Figures vii
List of Tables xiii
Nomenclature xiv
Chapter 1 : Introduction 1
1.1 Background and Motivation 1
1.2 Research Goals 4
1.3 Structure of Thesis 5
Chapter 2 : Literature Review 7
2.1 Introduction to Monolithic Reactors 7
2.2 Comparison of Key Characteristics of PBR and Monolith Reactors 8
2.2.1 Surface-Area-to Volume 8
2.2.2 Pressure Drop 8
2.2.3 Heat Transfer 8
2.2.4 Reactor Design 9
2.2.5 Manufacturability 9
2.3 Mechanical Properties of Metal Foams 13
2.3.1 Shape 15
2.3.2 Porosity 15
2.3.3 Metal Foam Mechanical Characteristics 16
2.4 Transport of Fluid Momentum Through Metal Foam 16
2.4.1 Fluid Flow Through a Metal Foam 16
2.4.2 Approaches to Modelling Fluid Flow Through a Metal Foam 17
2.5 Transport of Heat in a Metal Foam 18
2.5.1 Diffusive Heat Transfer 18
2.5.2 Convective Heat Transfer 19
2.5.3 Approaches to Modelling Heat Transfer in Open-Cell Monoliths 20
2.5.4 Determination of Metal Foam Interphasial (Convection) Coefficient 21
2.5.5 Heat Transfer Efficiency Criteria 25
Chapter 3 : Examining Steady-State Momentum and Heat Transfer Through a Metal-Foam Monolith Under Forced-Convection 29
3.1 Essential Objectives of a Convective Heat Transfer Study 29
3.1.1 Experimental Requirements 31
3.2 Physical Parameters of Interest and a Prototype Device for Measurements Thereof 33

3.2.1 Heat Transfer: Experimental Considerations 37
3.2.2 Momentum Transfer: Experimental Considerations 39
3.3 A Two-Phase Energy Balance Model for the Convection Experiment 39
3.3.1 Model Overview 39
3.3.2 Domain Description 40
3.3.3 Assumptions 41
3.3.4 Heat Transfer in the Solid Phase 42
3.3.5 Heat Transfer in the Fluid Phase 42
3.3.6 Momentum Transfer in the Fluid Phase 43
3.3.7 Boundary Conditions 45
3.4 Solution Method 47
3.5 Model Predictions 48
Chapter 4 : Experimental Protocol 53
4.1 Materials 53
4.2 Instrumentation 53
4.2.1 Pressure 53
4.2.2 Temperature 54
4.2.3 Fluid Velocity 54
4.3 Determination of Permeability 54
4.4 Determination of Effective Conductivity of Metal Foam 55
4.5 Determination of Convective Heat Transfer Coefficient 57
Chapter 5 : Experimental Results and Analysis 61
5.1 Momentum Transfer Coefficients 61
5.2 Effective Thermal Conductivity Coefficient 66
5.3 Convective Heat Transfer Coefficient 69
5.3.1 Methodology for Heat Transfer Coefficient Determination 69
5.3.2 Effect of Anodization on Convective Heat Transfer Coefficient 74
5.3.3 Pore-Scale vs. Bulk Scale Flow Characterization 78
5.3.4 Utility of Dimensional Dependency in Data Analysis 78
5.3.5 Comparison of Methodologies for Determining Volumetric Convection Coefficient 81
5.3.6 Comparisons of Experimental h_{vol} with Scalable Literature Values 88
5.3.7 Useful h_{vol} Correlations for Reactor Design 90
5.4 Thermal Efficiency 92
5.5 Assessment of Methodology for Convective Heat Transfer Coefficient Determination 93
5.5.1 Experimental Considerations 93
5.5.2 Experimental Scalability 95
5.5.3 Sensitivity of Experimental Results to Modelling Parameters 96
Chapter 6 : Reactor Design Using Experimental Data 111

6.1 A Coupled Heat-Exchange Combustion-Fired Methanol Steam Reformer 111
6.2 Domain Description.....112
6.2.1 Assumptions 112
6.2.2 Governing Equations.....113
6.2.3 Boundary Conditions.....114
6.3 Kinetics.....117
6.4 Physical Properties.....119
6.5 Solution Method.....121
6.6 Model Predictions.....121
Chapter 7 : Conclusions and Recommendations 126
References.....129
Appendix A : A Finite-Element Routine for Fitting h_{vol} to Experimental Data 139
Appendix B : Deployment of a Reactive Metal Foam Monolith for Fuel Reforming.....158
B 1 Deployment of a Reactive Metal Foam Monolith for Fuel Reforming.....158
B.1.1 Catalyst Preparation 159
B 1.2 Catalyst Support Coating.....161
B 1.2.1 Electrophoretic Deposition (EPD).....161
B 1.2.2 In-Situ Reactive Coating (Alkoxide Hydrolysis) 162
B 1.2.3 Electro-Oxidation 164
B 1.2.4 Spray Coating.....164
B 1.2.5 Dip coating 165
B 1.3 Post-Coating Treatments.....165
Appendix C : Testing and Characterization of Catalyst.....167
C 1.1 Catalyst Performance Criteria 167
C 1.2 In-situ Reaction Conversion Testing.....167
C 1.3 Active Catalyst Surface Area.....169

List of Figures

Figure 1: Monolith types, clockwise from top left: straight channel, screen mesh, open-cell foam, sintered packed beds, Kagome structures and honeycombs. 1
Figure 2: A conceptual heat-coupled integrated flow reactor. Feed gases for the exothermic reaction(s) are fed through the inner foam monolith, which is brazed to copper tube prior to catalyst coating. Heat evolved is conducted radially from the inner monolith to the tube and then to the shell monolith (also brazed to the tube). The endothermic feed gases are fed through the shell monolith. 3
Figure 3: Heat transport modes in the metal foam monolith used for a simple heterocatalytic fuel reforming reaction. In this case heat required for an endothermic reaction is drawn diffusively through the solid metal monolith and the surrounding catalyst support. Heat is supplied (or removed) from the catalyst support layer via convection with the gas stream flowing through the monolith. 4
Figure 4: An 80 ppi Incofoam nickel monolith 14
Figure 5: The internal cells of the metal foam typically take shapes that are either 20-faced or 14-faced polygons. Above, a 20-sided dodecahedron and a a 14-sided tetrakaidecahedron are projected as 2-D images onto the page. Foams can be characterized by their statistical geometry (e.g., a 12.7-sided metal foam cell). 14
Figure 6: Triagonal (left) and square (right) cross-sectional shapes of an 80 ppi nickel foam sample. 15
Figure 7: (Reproduced from from Paek et al. [66]) An apparatus for measuring the effective thermal conductivity (k_{eff}) of an alumimium foam. In this apparatus, uncertainties in the value of k_{eff} are related to the contact of foam ligaments and hot-reservoir/cold-reservoir plates. The uncertainties increase with the increasing pore size. 20
Figure 8: (Reproduced from from Tian et al. [18]) In this experimental system, heat is generated from a resistive heating pad, which conducts heat through its containment wall. 21
Figure 9: (Reproduced from Younis et al. [77]) Schematic representation of non-steady-state heating experiment with heated fluid passing through an initially cool metal-foam test sample. 25
Figure 10: (Taken from Tian [18]) Three thermal efficiency criteria represented graphically. Wire mesh compares favorably to regular-geometry Kagome structures and stochastic metal foams. 28
Figure 11: Schematic representation of constant heat flux experiment showing key variables 30
Figure 12: Schematic representation of heat transfer apparatus for determining the impact of catalyst coating on foams. In the steady-state the heat energy into the foam must be balanced by convective transfer from the foam to the air passing through. 32

Figure 13: A virtual prototype of the heat-transfer apparatus. Air passed through the heated monolith must have some temperature distribution related to the thermal efficiency of the monolith through which it passes. 35
Figure 14: Velocity field of the inlet tube (velocities through the porous monolith and outlet tube have similar fully developed profiles). 36
Figure 15: Temperature distribution of the heated monolith with air flowing through it (the monolith is heated by a single 50-Watt strip heater at the bottom)..... 36
Figure 16: Temperature distribution of air flowing through the outlet after heating through a porous foam heated at its bottom surface..... 37
Figure 17: Methods for connecting metal monoliths to heat transfer sinks (containment walls) for heat transfer studies and for integrated reactor prototyping. Above: non-reactive monolith is fit to the wall prior to catalyst coating of both monolith and wall. Below: reactive, coated monolith is fitted to the containment wall with thermal paste. 38
Figure 18: Schematic view of the system under study. Heat is driven into the bottom side of the foam monolith and the temperature of the fluid passing through the foam is monitored along the top midline. Model predictions are calculated for the 2D cross-section along the symmetry line of the monolith. 40
Figure 19: Twelve boundary conditions imposed on the two-phase forced convection model for air flowing through a metal foam. 45
Figure 20: An 842-element mesh used to solve three governing heat transfer equations in COMSOL 48
Figure 21: Model estimates for the isothermal profile inside the solid phase of a 10 ppi aluminium foam under 2.85 W heating with forced air at Reynolds number 180..... 49
Figure 22: Model estimates for the isothermal profile in the fluid phase of a 10 ppi aluminium foam under 2.85 W heating with forced air at Reynolds number 180. 49
Figure 23: Fluid temperature profiles at the upper boundary of the monolith domain (y=H) recovered using several meshes of the model of 10 ppi Aluminium foam under forced convection at $Re_C = 180$ and 2.85 W heating with h_{vol} of 10,000 $\left(W \cdot m^{-3} \cdot K^{-1}\right)$. 52
Figure 24: Schematic representation of the experimental setup for permeability measurement. A hot-wire anemometer was used to measure the air flow velocity after full development (mixing) through the porous monolith. Pressure drop was measured using a manometer. .. 55
Figure 25: The effective conductivity of the monoliths is determined by driving heat through a series-resistance between hot and cold reservoirs of water pumped at a steady flow rate. The known conductivity of the 4130 steel samples allows for the determination of the effective monolith conductivity at steady-state. 56
Figure 26: Forced air convection system used to determine volumetric convection coefficient of monolith samples (front view and side view section)..... 58

Figure 27: Photograph of the partially disassembled experimental heat exchange apparatus used in this work, with a view of the FLIR system, the clamping mechanism, a prototype insulation block and heating controls. 58
Figure 28: A thin layer of refractory cement is applied to the bottom face of the monolith (excess is trimmed and sanded down in last step). This thermally isolates the strip heater from the internal convective surfaces of the metal foam monolith. 59
Figure 29: Experimental data for pressure drop of air through metal foam samples with specified relative densities and coating treatments (uncoated or anodized). The pressure gradient is most affected by the pores-per-inch morphology of the foams with lower pressure drops corresponding to lower ppi. Lower relative densities also correspond to lower pressure drops. 62
Figure 30: Experimental data for pressure drop of air through metal foam samples of similar relative densities and average pore sizes (uncoated and anodized). Within the same relative density range and pore size, only the channel friction parameter, C_F is significantly affected by the presence of an anodized catalyst support layer while values of permeability, K, are similar between uncoated and anodized samples. 63
Figure 31: Experimental data for pressure drop of air through metal foam samples with varied relative densities and similar average pore sizes. The permeability, K, tends to decrease with increased relative density and with the addition of an anodized catalyst support layer. 64
Figure 32: Experimental data for pressure drop of air through metal foam samples with similar relative densities and varied average pore sizes. The permeability, K, and the channel friction factor, C_F, are much more sensitive to variation in average pore size than the presence of an anodized catalyst support layer. 65
Figure 33: Specific solid-phase temperature data (Ts_i and thermal differences observed over the course of a thermal conductivity experiment with metal foam samples). 67
Figure 34: Temperature data for the steady-state conductivity experiment (10 ppi uncoated Al foam with 0.08 relative density) 67
Figure 35: Experimental, modelled and literature values for the effective conductivity of a variety of metal foam samples. Effective conductivities are a strong function of the relative density (porosity) of the foam material. The conductivities are not correlated strongly to the number of pores per inch. 68
Figure 36: Specific fluid temperature (Tf_i), solid-phase (Ts_i and IR_i) and pressure data (P_i) taken over course of each convective-transport experiment. 70
Figure 37: FLIR image solid phase temperature data, IR1, IR2 and IR3 (left=inlet, right=outlet) for the 10 ppi uncoated aluminium metal foam (8.1% relative density) with coolant channel flow at Reynolds number of 400. 70
Figure 38: The effect of implementing Q-ratio tests on experimentally determined values of h_{vol} vs. values of h_{vol} recovered from non-filtered data. 72

Figure 39: Experimental vs. model predictions for air temperature along the top midline of a 10 ppi uncoated aluminium metal foam (8.1% relative density) with coolant channel Reynolds number of 400. One outlier data point is indicated in red..... 73
Figure 40: Experimental vs. model predictions for solid-phase temperature along exit face of 10 ppi aluminium metal foam (8.1% relative density) with coolant Reynolds number of 400... 73
Figure 41: Convective volumetric heat transfer coefficient as a function of channel Reynolds number for anodized and uncoated metal foams (48 experimental runs). The model was fit to minimize the sum of the squared errors between measured and predicted coolant temperatures..... 74
Figure 42: Impact of anodization on the pore-scale Nusselt number for 10 ppi foams..... 76
Figure 43: Impact of anodization on the pore-scale Nusselt number for 20 ppi foams..... 77
Figure 44: Impact of anodization on the pore-scale Nusselt number for 40 ppi foams..... 77
Figure 45: Volumetric convection coefficients for the uncoated and anodized foams related to the channel-scale Reynolds flow. 78
Figure 46: Volumetric convection coefficients for the uncoated and anodized foams related to the pore-scale Reynolds flow. 78
Figure 47: Estimates of convection coefficient h_{vol} to a spatially independent energy balance (fluid inlet temperature and outlet temperature with heating inputs) yields no distinction between the convection coefficient differences between coated vs. uncoated monoliths..... 80
Figure 48: Model-generated isothermal lines (black) for the fluid at ReC=400 and the solid monolith (light grey) through an 8.1% density foam monolith with 2.85 W of resistive heating through the bottom with modelled volumetric convection coefficient of 10,000 $W \cdot m^{-3} \cdot K^{-1}$ (top) and for 20,000 $W \cdot m^{-3} \cdot K^{-1}$ (bottom). 81
Figure 49: Estimated volumetric convection coefficient obtained via extrapolation of wall-convection data described in Equation (5.6) circled in blue, Equation (5.7) circled in red and via model fitting as described in Section 5.3.1 circled in yellow (colour regions applied manually as visual aides). 86
Figure 50: Estimated volumetric convection coefficient for anodized aluminium foams via extrapolation of wall-convection data described in Equation (5.6) circled in blue, Equation (5.7) circled in red and via model fitting as described in Section 5.3.1 circled in yellow (colour regions applied manually as visual aides). 87
Figure 51: Comparison of experimental heat transfer values for 10 ppi foam of $\varepsilon = 0.917$ against Hwang's pore-scale heat transfer correlation for 10 ppi foam of $\varepsilon = 0.95$ (correlation experimentally validated between $Re_P = 70$ and $Re_P = 300$)..... 89
Figure 52: A correlation of experimental heat transfer values for anodized 10 ppi foam of $\varepsilon = 0.917$ at flow rates of $Re_P = 1$ to 205..... 90

Figure 53: A correlation of experimental heat transfer values for anodized 20 ppi foam of ε = 0.890 to 0.910 at flow rates of Re_P = 10 to 50. 91
Figure 54: A correlation of experimental heat transfer values for anodized 40 ppi foam of ε = 0.910 to 0.920 at flow rates of Re_P = 6 to 22. 91
Figure 55: Thermal efficiency (as defined in Section 2.5.5) for tested foam monoliths as a function of Reynolds number. 93
Figure 56: The effect of adding the thermal diffuser to the model is shown to be insignificant. .. 98
Figure 57: The impact of adding a heat integrator on the y=H coolant temperature is shown to be minor with respect to the distribution of coolant temperature within the domain of interest (with insignificant consequences to the recovered convective heat transfer coefficient). 98
Figure 58: Effect of heat-flux split ratio (fluid phase) at y=0 on model coolant temperatures measured at y=H 101
Figure 59: Volumetric convective heat transfer coefficients change substantially depending on the fraction of total heat diffused into the monolith at y=0 (vs. heat convected away directly at the heating surface). 102
Figure 60: The fractional increase (or decrease) in fitted estimates of h_{vol} for coated/anodized foam monoliths plotted as a function of channel Reynolds number for different heat flux ratio ranging 0-100% 103
Figure 61: The fractional increase (or decrease) in fitted estimates of volumetric convection coefficients is larger for uncoated monoliths than for anodized monoliths as the modelled heat diffused into the fluid phase at y=0 increases from 0% to 100% 104
Figure 62: The fractional increase (or decrease) in fitted estimates of h_{vol} for anodized monoliths, with and without an insulating barrier between the heater and the monolith (Figure 28), as the modelled heat diffused into the fluid phase at y=0 increases from 0% to 100%. 105
Figure 63: The fractional increase (or decrease) in fitted estimates of volumetric convection coefficients for uncoated monoliths with and without an insulating barrier between the heater and the monolith (Figure 28), as the modelled heat diffused into the fluid phase at y=0 increases from 0% to 100% 106
Figure 64: A modified version of the heat-exchange model (solid-phase temperatures) with an added steel integrator and a "faulty" insulation layer (5 $Wm^{-1}K^{-1}$) 107
Figure 65: Introduction of insulation failure into the model has negligible impact on recovered values of h_{vol}. 108
Figure 66: (Taken from Hwang et al. [57]) Smoke thread images of non-plug-flow through a thin section of aluminium foam. 109
Figure 67: Velocity profiles of the experimental model system with plug flow assumption (top) and with an arbitrary fully developed turbulent flow distribution (bottom) 110

Figure 68: Fluid temperature profiles predicted by the plug flow and turbulent velocity profiles. 110
Figure 69: The model coupled heat-exchange fuel reforming system. 111
Figure 70: Twelve boundary conditions imposed on the two-phase forced convection model for air flowing through a metal foam. 114
Figure 71: A simple correlation of experimental h_{vol} for air-cooled 40 ppi anodized foams across a range of pore-scale Reynolds numbers. 121
Figure 72: Sample physical values from model CH18HC coated aluminium monolith reactor running at with a 50-50 feed of MeOH and H2O at 300 kPa and a pressure drop of 5 Pa. 123
Figure 73: Distribution of values for the volumetric heat transfer coefficient throughout the reactive monolith. 123
Figure 74: Maximum monolith temperature (x=L, y=h2 as per Figure 70) in the simulated reactor at varied "forced" values of the convective exchange coefficient, h_{vol} 124
Figure 75: Yields of hydrogen from methanol feedstock in the simulated reactor at varied "forced" values of the convective exchange coefficient, h_{vol} 125
Figure 76: Sequence of steps for the production of catalytically active metallic monoliths. Processes are shown in shaded hexagonal entries and production artifacts in rectangular boxes. 158
Figure 77: Schematic representation of platinum catalyst nanoparticles (blue) supported on a single ceramic particle (white). 159
Figure 78: Left (Taken from Lankin, M. [98]): electrophoretic deposition of suspended surface-positive ceramic particles on a direct-current cathode in a non-conducting fluid. Right: 100× magnification of an 80 ppi stainless steel mesh coated in an approximately 5 micron-thick EPD coating of α -alumina. 162
Figure 79: 40 ppi aluminium foam monoliths dip-coated in a glycerol-alumina suspension. Left, the wet green-body exhibits pooling around the edges of the cell monoliths. Right: the dried, calcined foam is coated unevenly with thickened regions where the wet green-body had pooled. 165
Figure 80: An 80 ppi stainless steel mesh before and after calcinations at 850 °C (raised at 2 °C/min.) Left: the green-body coating of alumina, deposited by EPD. Right: incompatible coefficients of thermal expansion between the steel and ceramic have shattered the coating. 166
Figure 81: Apparatus for conversion of a methanol vapour stream to carbon monoxide and hydrogen gas. Typically, flow is delivered to provide 20 seconds mean residence time for unreacted species. 168
Figure 82: Comparison of experimental conversion (packed bed) vs. temperature data to Imamura et al. The light-off curve for the Pt/Al2O3 catalyst is much steeper than that for the Pt/CeO2 catalyst used by Imamura et al. [101] 169

List of Tables

Table 1: Model input parameters for 10 ppi foam under 1.4W heating at $Re_C = 180$ 50
Table 2: Energy, mass and momentum balance in COMSOL heat-transfer model 51
Table 3: Sample experimental results for forced-air convection through metal foam monoliths... 65
Table 4: Correlations: foam parameters and convective heat exchange metrics 75
Table 5: Comparison of convective heat transfer coefficient determined from different methodologies 84
Table 6: Parameters for rate constants (Amphlett et al.) 119

Nomenclature

Symbol	Meaning	S.I. Units	Symbol	Meaning	S.I. Units
α_s	*Specific surface area*	m^{-1}	K	*Permeability*	m^2
k_s	*Solid-phase conductivity*	$W \cdot m^{-1} \cdot K^{-1}$	ε	*Porosity*	
ρ_s	*Solid-phase density*	$kg \cdot m^{-3}$	T_{ref}	*Reference temperature*	K
C_{p_f}	*Solid-phase heat capacity (constant pressure)*	$J \cdot kg^{-1} \cdot K^{-1}$	C_F	*Darcy-Forchheimer coefficient*	
T_s	*Solid-phase temperature*	K	μ	*Fluid viscosity*	$kg \cdot m^{-1} \cdot s^{-1}$
$\overline{T_f}$	*Average fluid temperature*	K	Re	*Reynolds number*	
C_{p_f}	*Heat capacity of fluid*	$J \cdot kg^{-1} \cdot K^{-1}$	Nu	*Nusselt number*	
ρ_f	*Density of air*	$kg \cdot m^{-3}$	A_s	*Solid-phase surface area*	m^2
$\overline{h_w}$	*Wall convection coefficient (Tian)*	$W \cdot m^{-2} \cdot K^{-1}$	$\overline{h_{vol}}$	*Volumetric wall convection coefficient*	$W \cdot m^{-3} \cdot K^{-1}$
$\overline{h_w^{\bullet}}$	*Average wall convection coefficient*	$W \cdot m^{-2} \cdot K^{-1}$	$\overline{h_w^{\bullet}}$	*Average wall convection coefficient*	$W \cdot m^{-3} \cdot K^{-1}$
h_{vol}	*Effective volumetric convection coefficient*	$W \cdot m^{-3} \cdot K^{-1}$	$\xi_{\dot{Q}}$	*Volumetric heat transfer efficiency*	
$\Delta T_{avg}^{\bullet}$	*Average driving temperature*	K			
k_{eff}	*Effective conductivity*	$W \cdot m^{-1} \cdot K^{-1}$	MR	*Monolithic reactor*	
Δt	*Finite time increment*	s	SR	*Steam reforming*	
Δx	*Finite x-distance increment*	m	MD	*Methanol decomposition*	
Δy	*Finite y-distance increment*	m	POx	*Partial oxidation*	
U_f	*Supeficial fluid velocity*	m	WGS	*Water-gas shift*	
$u_{f_{in}}$	*Velocity of air at inlet*	$m \cdot s^{-1}$	H	*Channel characteristic diameter*	m
$u_{f_{out}}$	*Velocity of air at outlet*	$m \cdot s^{-1}$	p	*Pressure*	$kg \cdot s^{-2} \cdot m^{-1}$

Chapter 1: Introduction

1.1 Background and Motivation

Catalytic packed-bed reactors (PBRs) have been used for gas-phase heterocatalytic reactions for more than a century. PBRs are composed of granular solids packed into a tube through which reactant feeds are passed. The granular solids may be catalytically active or may have solid catalyst particles dispersed on their exposed surfaces. These reactor systems are easy to build and can provide excellent mixing of reactant gas streams and they may also exhibit very high surface-area of catalyst per unit volume. However, these systems require a significant amount of pump/blower pressure to provide sufficient bulk transport of reactant/product gases and they generally do not allow for efficient heat transfer. For reactions that take advantage of efficient solid-phase heat transfer in low-pressure applications, it is advantageous to use a monolith as the substrate rather than a packed bed.

Andrzej Cybulski defines monolith reactors (MRs) as, "continuous unitary structures containing many narrow, parallel straight or zigzag passages"[1]. The word is derived from the Greek "mono" meaning single and "lithos" meaning stone. Monoliths vary in morphologies. Some examples of common monolith morphologies are shown in Figure 1.

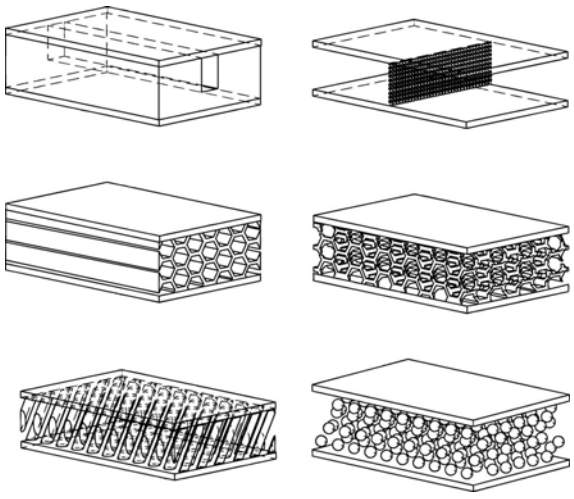

Figure 1: Monolith types, clockwise from top left: straight channel, screen mesh, open-cell foam, sintered packed beds, Kagome structures and honeycombs.

Monoliths are used in automotive catalytic converters, turbofan afterburners, industrial off-gas burners and hydrogen production [1]. The use of monolithic (single-piece) reactors for heterocatalysis of gas-phase reactions became widespread with the development of automotive catalytic converters in the late 1970s. Automotive catalytic monoliths are used to reduce nitrous oxides (NO_x) and to oxidize carbon monoxide and hydrocarbons from internal combustion engine exhaust. The automotive application requires very low pressure drop, very high flow rates and ease of reactor manufacture. Heat exchange designs for these monoliths have been focused on maintaining steady-state temperatures high enough to achieve full conversion of reactant feeds [1]. Recent advances in portable hydrogen-production from fossil fuels have motivated much more advanced thermal design criteria.

For fuel cell systems, an interesting application is the design of a fuel reformer (converting fuel to hydrogen) that can be coupled to an afterburner (oxidizing hydrogen containing anode off-gas). The reforming reaction can be endothermic, requiring heat input that can be provided (in part) by the heat generated in the afterburner. A compact, integrated design as shown in Figure 2 is proposed and is a conformal shell-and-tube reactor wherein the exothermic and endothermic gas-phase reactions occur in physically separated sections with heat transported primarily through the solid phase of the monoliths. The metallic monolith serves simultaneously as an effective transporter of heat and as a substrate for coating of catalysts. For effective reactor design in anysuch non-isothermal system, local reaction rates must be controlled. The rate of any chemical reaction depends on local reactant/product concentration and temperature; the latter affecting the reaction rate constant via Arrhenius type dependency. Further, an elementary reaction proceeds either with net generation or with net consumption of heat. The local reagent/product concentration depends on the balance between rate of mass/species transport and rate of reaction. The local temperature depends on the balance between heat transport and the rate of heat generated/consumed. The mass/species and heat transport effects are coupled to each other via the reaction rate. Thus, the net reactor performance is a result of coupled reaction-transport processes that are dictated by the local temperature and reactant concentrations within the monolith domain.

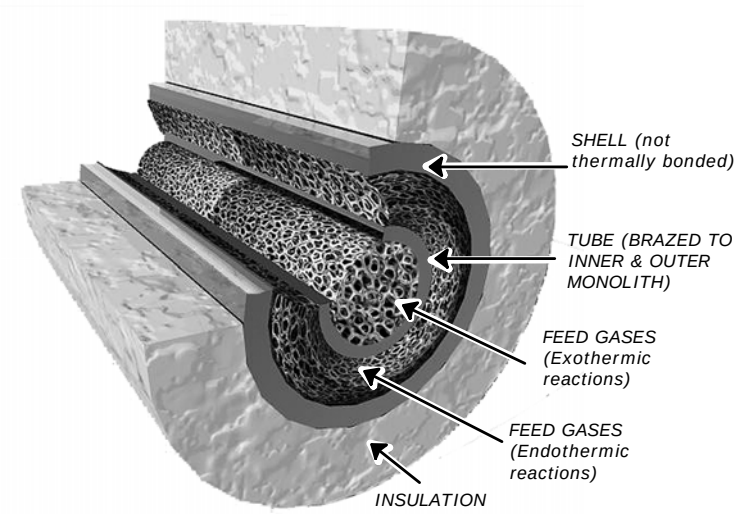

Figure 2: A conceptual heat-coupled integrated flow reactor. Feed gases for the exothermic reaction(s) are fed through the inner foam monolith, which is brazed to copper tube prior to catalyst coating. Heat evolved is conducted radially from the inner monolith to the tube and then to the shell monolith (also brazed to the tube). The endothermic feed gases are fed through the shell monolith.

To design monolith reactors, one must consider the relevant transport processes in addition to the reaction kinetics. Figure 3 shows the key transport processes occurring in the porous monolith are bulk and intra-pore mass transport, momentum transport and heat transport through the monolith as well as heat transfer between the fluid and the monolith. Mathematical modelling of heat transfer behaviour in monolith reactors requires scaleable parameters or transport coefficients. Specifically, the following transport coefficient parameters are required:

- The Darcy permeability, $\mathbf{K}$, of the monolith (for characterizing fluid flow) and, if relevant, the Darcy Forchheimer fitting coefficient, C_F to describe the momentum transport.
- The bulk effective thermal conductivity, k_{eff} to describe diffusive heat transport.
- The volumetric thermal convective coefficient, h_{vol} to describe the heat transfer from the fluid to the solid matrix of the monolith for a given fluid-flow regime.

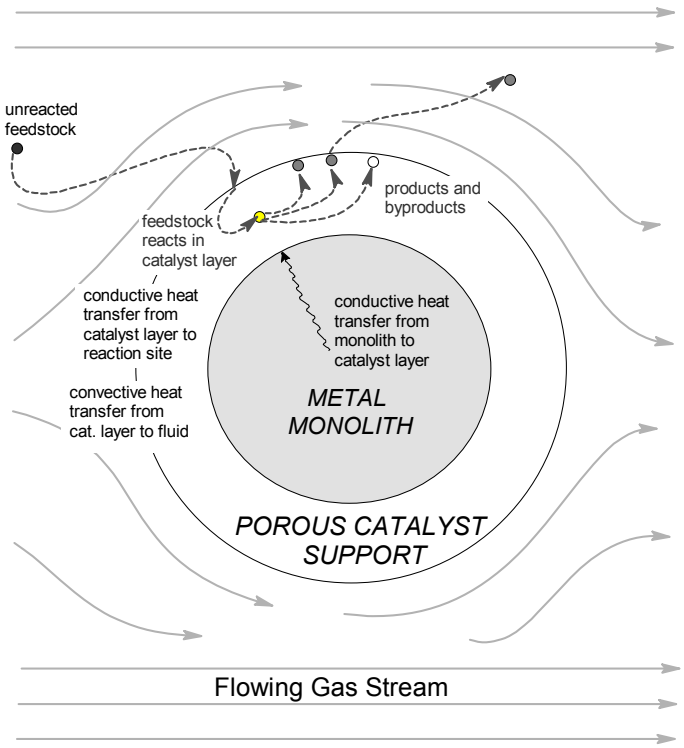

Figure 3: Heat transport modes in the metal foam monolith used for a simple heterocatalytic fuel reforming reaction. In this case heat required for an endothermic reaction is drawn diffusively through the solid metal monolith and the surrounding catalyst support. Heat is supplied (or removed) from the catalyst support layer via convection with the gas stream flowing through the monolith.

1.2 Research Goals

This work is concerned with the determination of scalable heat transfer parameters useful for designing a combined heat-transfer/reaction monolith based on an isotropic open-cell metallic foam substrate (metal foam).

Of particular interest are the following:

1. Improvements to experimental methods for investigating convective heat transfer in porous materials such as metal foams. In particular, development of a steady-state method that will yield accurate results at low flow rates consistent with application in "slow-kinetics" chemical processing.

2. The experimental characterization of heat and momentum transfer properties of both uncoated metal foams used in heat transfer and catalyst-support coated metal foams suitable for reaction engineering.
3. Understanding the role (if any) of monolith morphology/geometry and coating materials in microscale transport phenomena.
4. An assessment of the non-isothermal heat-transfer performance of a catalyst coated monolith via a selected heat-coupled model reaction.

1.3 Structure of Thesis

Chapter 2 of this thesis introduces the physical characteristics of metal-foam monoliths under convective heat transfer (compared to packed bed monoliths) and surveys the means by which foam heat exchange devices have been investigated in previous work.

Chapter 3 of this thesis identifies the experimental information required to meet the research goals of this work outlined in Section 1.2. This chapter develops an experimental strategy for recovering this information and quantifying it by comparing experimental observation with modelling analysis.

Chapter 4 of this thesis details the experimental protocol by which the required convective heat transfer coefficient, h_{vol}, for catalyst-support covered metal-foam monoliths was recovered.

Chapter 5 of this thesis details the experimental results and provides an analysis of their physical meaning and of indications for experimental sensitivities.

Chapter 6 of this thesis uses the physical information recovered in Chapter 4 and Chapter 5 to model a simple methanol steam reformer and to assess the heat-exchange impact of catalyst-support coating on the reactor temperature profile and reactor yield.

Chapter 7 offers conclusions from this work and suggests improvements for the experimental method.

Appendices to this work include: references, exemplary high-level code used to assess experimental phenomena, background information on methods for introducing a catalyst support onto the surface of a metal-foam monolith and brief discussion of methods for full experimental characterization of the physical and kinetic properties of a ceramic-supported catalyst layer on a metal foam monolith reactor.

Chapter 2: Literature Review

In this chapter, monolith characteristics relevant to reactor applications are first discussed (vs. characteristics of packed-bed reactors). Since this work is concerned with metal foam monoliths, the subsequent sub-sections present relevant literature on metal foams, including a discussion of manufacturing options, geometry, mechanical characteristics, and thermo-fluid transport properties. Methods of physical-parameter analysis and modeling are reviewed leading to a discussion of current literature for determining convection transport parameters for metal monoliths. The chapter ends with a brief discussion of an efficiency parameter for characterizing a metal foam monolith's suitability as a heat transfer agent for a coupled heat-exchange/reactor system.

2.1 Introduction to Monolithic Reactors

Monolithic substrates for heterocatalytic reactor applications can be fashioned from any rigid material, but most are either metal or ceramic. The ceramic supports have an advantage over metallic supports in that they can withstand higher temperatures, and, if suitably selected, can serve as a direct support for the catalyst. On the other hand, owing to higher thermal conductivity of the solid constituent, metal substrates have better heat transfer characteristics than ceramic substrates.

Automotive catalytic converter monoliths are mostly extruded ceramic honeycomb structures or steel honeycombs with washcoats of alumina-supported catalyst[2]. Metallic, catalyst-coated monoliths may employ foam, honeycomb, mesh, microchannel and wire type substrates upon which catalyst is deployed [2-5]. Since the early 1990s, metallic foam monoliths have occupied niche markets in motorcycle emissions control, passive ozone degradation and combustion of restaurant emissions [4], [6].

Incentives to use metal foam monoliths include low-pressure drops, the ability to build conformal reactors and the possibility of integrating reactors with heat exchange devices. Anticipated benefits include the reduction of thermal contact resistances, development of more

uniform steady-state temperature gradients and improvements to overall heat transfer efficiencies.

2.2 Comparison of Key Characteristics of PBR and Monolith Reactors

Conventionally, catalytic reactions are realized in packed bed reactors (PBRs). Thus, in choosing a monolithic reactor for a given application, a comparison with a PBR must be made. For design of a monolith reactor, consideration must be given to several factors including its pressure drop, heat transfer, mass transport, and surface area. The ease of fabrication and method for deployment of catalyst must also be considered.

2.2.1 Surface-Area-to Volume

Owing to the larger amount of catalyst in a given volume, packed bed reactors typically have larger catalyst surface-area-to-volume ratios than monolithic reactors. However, in many cases only the catalyst in the outer shell of a catalyst pellet may be effectively utilized due to intra-particle transport limitation. Due to the open structure of a monolithic reactor, the *effective* surface area utilized for reaction *may* be comparable to that in a PBR despite the significantly lower surface area density of the base structure.

2.2.2 Pressure Drop

The tight packing in a PBR inherently results in a relatively large pressure drop. Monoliths, which are open-structured and have high porosity, typically exhibit much lower pressure drops compared to packed bed reactors [7], reducing energy losses to reactant feed pumping.

2.2.3 Heat Transfer

It is generally accepted that monolithic designs employing metallic substrates have much better internal heat exchange than packed beds and that metallic monoliths have the potential to dissipate high heat loads in small volumes [8]. Comparisons of heat transfer of a monolith and a packed bed are dependent on the extent to which volumetric and mass densities differ between the two classes of reactors. Alstrohm-Silversand et al. [9] noted that packed pellet beds have

superior thermal response, defined as the ratio of thermal inertia (heat capacity) over total heat-transfer capacity owing to the large available convective heat transfer surface area of packed beds. Experimental and theoretical results showing greater thermal conductivity for packed beds per unit volume owing to higher solid-phase density than monoliths, while convective and overall heat transfer coefficients were higher in monoliths [1], [10].

2.2.4 Reactor Design

Foams afford more compact and easily conformable reactor designs for fast-kinetics processes than honeycomb monoliths [10]. While they suffer from much lower catalytic surface area than is achievable in a packed bed, their inherent behaviour as a static mixer provides relative advantage as reactive gas velocities increase and the effect of gas mixing in the foam improves local species transport. The possibility of using metallic foams as more compact, lighter weight, low backpressure reactor systems with excellent conductive heat transfer properties has motivated several studies on the feasibility of their use as a catalyst-support monolithic substrate (a structured catalyst) [11-17], such that combined heat transfer and mass transfer are accomplished. These studies have been confined to adiabatic cases with no consideration of internal heat transfer impacts due to the addition of a catalyst support to the internal surfaces of the metal foam monolith.

2.2.5 Manufacturability

Packed-bed reactors are more easily manufactured than metal monolithic reactors. Apart from the complications of manufacturing a suitable metal substrate, the manufacturability of a thermally conductive monolithic reactor depends on the thermal and chemical performance of the metal, the type of catalyst coating, and the geometric arrangement of the individual “pores”.

Thermal performance of the metal is a limiting design factor. For example, aluminium metal foam can be readily formed by investment casting, but cannot be easily coated with a ceramic powder due to limitations on curing temperatures. Also, chemical incompatibility with acidic platinum salts rules out wet impregnation treatment processes on aluminium supports, but not

on steel supports. Geometric orientation becomes important in anisotropic monoliths, such as sintered wire mesh monoliths with very effective heat transfer in one direction and inefficient transfer in another direction [18].

The fabrication methods for the monolith supports themselves are highly varied. Microchannel reactors can be built using simple micro-milling, complex laser-machining, hot stamping or photolithographic etching, depending on the size of channels and whether the substrate is metallic, ceramic or polymeric in nature. Monoliths of more complex structure, such as foams and meshes require special fabrication methods such as investment casting, sintering (foams), or a combination of weaving and sintering (meshes). The method for deployment of supported catalyst onto the surfaces of these monolithic structures may use one or more of the dip coating, sol-gel, spray coating chemical vapour deposition or anodization processes.

2.2.5.1 Metal Foam Manufacturability

Open cell metal foams (Figure 4) are made by several techniques. In some cases, the foam is made by injecting gas into a molten slurry and cooling the two-phase mixture such that the metal accumulates at the "gaps" between adjacent bubbles [19]. Investment casting is used to produce foams of Al, Cu, Mg and Zn alloys. More affordable copper, stainless steel and FeCrAlloy foams can be made from sintering metal into a polymer substrate and burning off the polymer at high temperature. Inco uses a proprietary carbonyl process to produce its line of nickel metal foams in which chemical vapour deposition (CVD) is used to deposit a feedstock of nickel tetracarbonyl onto a polyurethane substrate with subsequent burn-off of the organic material [20, 21]. Sputtering, electroplating and CVD can be used to coat pre-existing conductive foam structures with other metals.

2.2.5.1.1 Catalyzing Metal Foam Surfaces as Reactor Substrates

Catalysts may be deployed upon a monolithic substrate either directly or indirectly. In a direct method, catalyst can be directly deposited on the substrate. In the indirect method, the substrates, typically metal, are coated with a catalyst support material such as alumina or ceria

followed by deposition of the catalysts. A variation of the direct method is when catalyst adhered to fine particles of catalyst-support are deposited on the monolithic substrate.

A key concern for catalyst coating techniques is the mechanical stress placed on the coating through thermal cycles when the coefficient of thermal expansion for the support coating and the underlying metal monolith are different. The fracture strain of the coating will dominate the thermal-shock resistance of the supported catalyst [22].

2.2.5.1.1.1 Washcoating

Descriptions of washcoating techniques are abundant [23], [24]. A washcoat typically involves the percolation of a sol containing support particles through the porous monolith substrate. Careful control of rheological properties, flow rates and chemical conditions leaves a gel-film on the substrate and subsequent heating transforms the gel into a dense support layer.

2.2.5.1.1.2 Dip Coating

Dip coated monolith substrates are fabricated by immersion in a sol containing support particles and drawing it out at a specific velocity that controls the gel-layer thickness. The viscosity of the sol and the presence of binding agents is important in maximizing the mass of gel adhered to the monolith [25]. Again, the layer is heated, leaving a ceramic support behind. Additional details of dip coating attempted in this work are summarized in Appendix B.

2.2.5.1.1.3 Spray Coating

Spray coated monoliths are effectively "painted" by application of particles (often microdroplet sols suspended in air). Control of the size of the microdroplets and their density in the airstream and the bulk flow rate of the airstream allows for rough control of the rate of ceramic deposition. Spray coating may not allow for even coating, especially for the foam monolith surfaces that are hidden from the path of the spray. As a result consistent mechanical properties within the spray coat are difficult to achieve in complex geometries (see Figure 79 and Figure 80 of Appendix B). Shi et al. [22] investigated the mechanical properties of various spray coated ceramic-(alumina)-

on-metal layers, finding that the modulus, E, of the ceramic coating is dependent on the phase composition and porosity of the ceramic. Non-linear stress-strain behaviours depend on the laminar grain structure of the ceramic layers [22].

Spray coated foams can be used for microchannel structures and plasma spray [14] has also been used for foams. The surface area of a wire mesh monolith can be increased by a factor of 50 with thermal spray coating of alumina [9]. Thermal spray coating is a vastly superior treatment to washcoating, due to flakiness of the washcoated wire. Thermal spray coating does not leave a very porous ceramic layer, so some have used thermal spray as a base layer for washcoating [26].

Additional information on spray coatings performed in this work is detailed in Appendix B.

2.2.5.1.1.4 Electrochemical Methods

Electrochemical methods for coating with alumina and zirconia layers up to 80 microns are well established [27], [28], [29]. These methods are restricted to metal substrates, more specifically to metals that can be electrochemically oxidized into an oxide morphology suitable as catalyst support. An aluminium substrate can be anodized at high potentials to achieve nano-scale periodic porous structure. Al^{3+} and O^{2-} and OH^- ions are interchanged in the course of anodization [30].

Anodization has advantages over other alumina support strategies since the thickness can be controlled, there is excellent bonding and non-aluminium surfaces can be anodized very easily if an electro-deposited layer of Al is first laid down [31]. The porosities and thicknesses of the alumina layer can be controlled by potential and current density [2], [32].

2.2.5.1.1.5 Wet Impregnation

Wet impregnation relies on the direct physisorption of complex salts to a ceramic support surface (e.g., alumina, ceria, zirconia). The salts are then treated in place to leave only the catalytically active metal adsorbed on the support. The ceramic portion of the sols used to washcoat, dipcoat, spray coat or electrophoretically deposit a ceramic onto a metal foam monolith can be first wet impregnated to ensure that both catalyst and catalyst support are

deposited in the subsequent step. The physico-chemical mechanics of wet impregnation tend to be described in terms of parametric models. Spieker et al. have developed a parameterized, black-box model for applying catalyst to different substrates with different solvent/pH conditions [33]. Sadykov describes catalyst impregnation on a milli-reactor of γ-alumina [34]. Suzuki et al. [35] attempted wet impregnation of catalyst on a flat aluminium foil as well as on a silica microchannel with an electrodeposited aluminium layer. The foil product appeared to be more catalytically active than the microchannel. Additional details of wet impregnation methods are cited in Appendix B.

2.2.5.1.1.6 Other Coating Methods

Other methods such as sol-gel processes, chemical vapour deposition and sputtering are also methods of support coating a metal monolith.

2.3 Mechanical Properties of Metal Foams

This thesis is concerned with reticulated open-cell metal foam monoliths and all ensuing discussions are limited to characteristics and properties of these foams. Metal foams made of aluminium, copper and nickel alloys are desirable monolithic substrates for heat-coupled fuel reformers of the type conceived in Figure 2 on Page 3 because they have high conductive heat transfer coefficients (compared to other monolith materials), low pressure drop, they can be manufactured at reasonable cost and are easily machined into optimum conformal shapes required for heat-coupled systems.

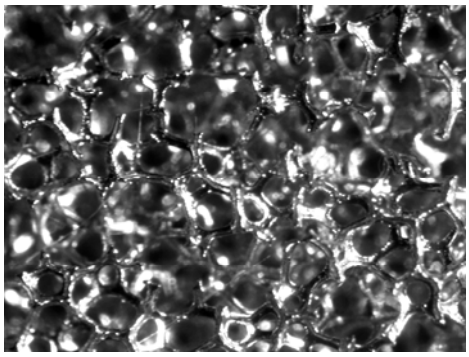

Figure 4: An 80 ppi Incofoam nickel monolith

Giani et al. [12] define the reticulated foams that are particularly well suited for fluid phase reactions: Open-celled foams are three-dimensional (3D) cellular materials made of interconnected solid struts, forming a network [36]. The unit cell in a foam resembles a polyhedron with pentagonal or hexagonal faces that limit a spherical-like inner space. For the sake of modelling, the open cells are often treated as an aggregation of either 14-sided polyhedra (tetrakaidecahedron) or 20-sided polyhedra (dodecahedron) seen in Figure 5. These 14-sided and 20-sided configurations yield minimal surface energies [37] for two-phase systems of bubbles where surface tension is the dominant force supporting the cellular bubbles in the foam. Each cell, defined by the hollow volume of the polyhedron, constitutes a "pore" [12].

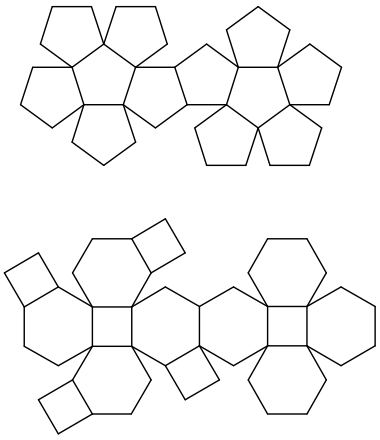

Figure 5: The internal cells of the metal foam typically take shapes that are either 20-faced or 14-faced polygons. Above, a 20-sided dodecahedron and a a 14-sided tetrakaidecahedron are projected as 2-D images onto the page. Foams can be characterized by their statistical geometry (e.g., a 12.7-sided metal foam cell).

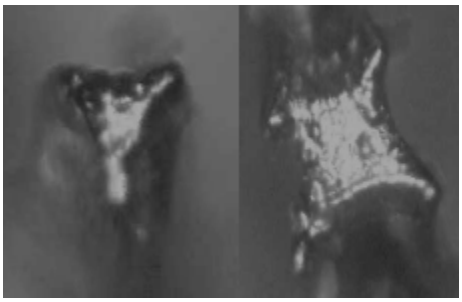

Figure 6: Triagonal (left) and square (right) cross-sectional shapes of an 80 ppi nickel foam sample.

2.3.1 Shape

The geometry of the open-cell metal foams considered here are the same as the shapes of polymer open cell foams. These polymer foams obey the same rules of surface tension stability published by Lord Kelvin in the 19th century [38]. These rules say that the average geometry of a foam is arranged in equally sized cells in such a way that overall surface area is minimized, which will also minimize the total surface tension [39]. Metal foam geometries are typically characterized as solid networks of 12 or 14-sided polyhedra [36]. The idealized polyhedral shape of most metal foams is shown in Figure 5. In open-cell geometry, the edges and vertices of the polyhedra are traced by metal "ligaments" and the faces of the polyhedra are voids. The cross-sectional shapes of the ligaments may be hollow, may have triagonal, square or other irregular shapes (Figure 6).

2.3.2 Porosity

Foams, or cellular solids, are characterized by their porosity, ε, which measures the fraction of bulk volume not occupied by solid. Typical foams have void fractions at or above 90% [40]. Open-cell metal foams typically have surface-area-to-volume ratios between *500* and *3,000* $m^2 \cdot m^{-3}$ [41]. The total surface area-to-volume ratio of a metal foam increases with an increase in the number of pores per unit volume.

2.3.3 Metal Foam Mechanical Characteristics

As the density of the foam increases (i.e., solid fraction increases), so does the tensile, compressive and shear strength. The bulk mechanical strength properties, such as tensile and shear strengths are, in the case of Aluminium alloy A356, two orders of magnitude lower than for the solid material of the same bulk dimensions [1]. The mechanical strength of metal foams is related to the porosity as an indirect consequence of the thickness of cell ligaments [42]. Under compression, the stress-strain curve of metal foams shows a short-lived linear-elastic deformation followed by a plateau of deformation at a nearly constant stress followed by a "region of densification as the cell walls are crushed together" [43].

2.4 Transport of Fluid Momentum Through Metal Foam

2.4.1 Fluid Flow Through a Metal Foam

Metal foams offer much lower pressure drops than packed beds. Air flowing at 800 feet per minute (fpm) through a 100 pore-per-inch reticulated foam will have a pressure drop of about five inches water per inch. At 200 fpm, the pressure drop is less than one inch [43]. The flow characteristics of fluids in foams are complex. Due to the required tortuous path a fluid must take through a reticulated foam, there is a very high level of mixing between fluid feed streams into foam monoliths [44]. Flow behaviour through foams is most often predicted through semi-empirical approaches employing an effective permeability to relate average flow rate and pressure drop (see Section 2.5.3). The permeability, K, is proportional to the ease of flow through a porous medium for a given fluid and it increases with pore diameter and overall porosity [45]. Several experimental studies have determined permeability values for a variety of metal foam monoliths [12, 46-55]. For most commercially available uncoated metal foams, typical permeability values range from $0.5 \times 10^{-7} m^{-2}$ to $1.5 \times 10^{-7} m^{-2}$.

[1] Material Property Data: www.matweb.com

2.4.2 Approaches to Modelling Fluid Flow Through a Metal Foam

In order to account for convective transport between the solid monolith and coolant throughout the entire domain of the monolith, it is necessary to have a proper model for momentum transport. Wall-convection models treat fluid velocities and densities as constant, but the pressure drop of fluid through the monolith will have consequences on both velocity and density. The quadratic extended Darcy flow model (also called the Darcy-Forchheimer model) has been used as the basis for work in solving the transport equations for the extended flow problem [56]. In Equation (2.1), V_f is the fluid velocity, K is the permeability, μ is the dynamic viscosity, ρ_f is the fluid density and C_F is the Forchheimer coefficient. The one-dimensional Darcy-Forchheimer pressure-velocity correlation is:

$$\frac{\Delta P}{L} = \frac{\mu}{K} V_f + \rho_f C_F V_f^2 \tag{2.1}$$

Hwang [57] showed that the channel friction factor (the Forchheimer coefficient) , C_F, for a fluid-through-monolith decreases with increasing Reynolds number due to less channel blockage and lower surface drag.

The Brinkmann equation (2.2), developed in 1947-48, considers the Stokes drag on a sphere in a packed bed, including fluid effects from the drag on neighbouring spheres where p is the local pressure, μ_{eff} is an "effective" viscosity term accounting for flow through pores within the sphere itself, and $\mathbf{u}_D$ is the fluid flux [56].

$$\nabla p = -\frac{\mu}{\mathrm{K}} \mathbf{u}_D + \mu_{eff} \nabla^2 \mathbf{u}_D \tag{2.2}$$

Traditional models, like the Darcy, Darcy-Forchheimer and Brinkmann extended model use semi-empirical correlations to predict the behaviour of porous flow. The development of the general model proposed by Tien and Vafai [58], Cheng and Hsu [59] and Nithiarasu and Seetharamu [60], has allowed the inclusion of all fluid forces and the solid drag force into the momentum equation. The Darcy and Brinkmann equations are limiting cases of the general

transport model. The general model is similar to the Navier-Stokes model and can be used to solve transient systems. However, due to the problem of deriving analytical solutions, it, like the Navier-Stokes equation, can only be approximated numerically.

2.5 Transport of Heat in a Metal Foam

The conductive and diffusive transport phenomenon seen in microchannel reactors also applies to the general case in high-porosity metal foams [61]. Metal foams have the potential for three-dimensional radiative and convective [mass] heat transfer that is not possible in straight-channel monoliths [17]. This can lead to reduced temperature gradients in the foam reactor. Zumbrunnen et al. found from volume averaged numerical modelling that radiative heat transfer is only important when the thickness of the foam (in the direction of dominant effective transfer) is large relative to pore diameter [62]. In this work the discussion is restricted to conduction and convection modes of heat transport.

2.5.1 Diffusive Heat Transfer

Solid-phase transport of heat in metal foams is dominated by diffusion (conduction). Depending on the fluid flowing through the foam, convection may be important to bulk heat transfer (solid and fluid phases). In addition, transfer of heat between the solid phase of the foam and interfacing fluid must be considered. Effective thermal conductivity and volumetric heat transfer coefficients are the required parameters to characterize the heat transport and interphasial heat transfer, respectively of the foam.

Typical metal foams have effective thermal conductivities that are one-third to one-half the product of their relative density times the conductivity of the constituent metal [63]. The effective thermal conductivity coefficient, k_{eff}, is readily measured as a bulk property of foam (and its fluid contents) by using several steady-state apparatuses [64], [53], [65]. In the case of pores occupied with gases, the thermal conductivity of the bulk foam is dominated by the thermal conductivity properties of its solid component [19].

The effective thermal conductivity is a strong function of the overall porosity, ε (relative void volume), but has no systematic relationship with pore density (number of pores, or open cells, per unit volume). Paek found k_{eff} depended on porosity but not on pore density (size of pores for a given porosity, ε) [66]. Fuller found that for monoliths of the same material property that bulk volumetric heat transfer increases with decreasing pore size [65] as did Hwang et al. [52].

2.5.2 Convective Heat Transfer

Volumetric heat transfer improvements in metal foams over other materials are due to two factors: 1) The foams cause the flow to be more turbulent, which improves heat transfer and 2) The foams provide an extended surface for heat transfer via thermal conductivity through the solid ligaments [65]. The friction factor and volumetric heat transfer coefficients increase with decreasing pore sizes (which in turn are correlated to overall porosity, ε). The volumetric heat transfer coefficient, h_{vol}, at fixed Reynolds number, increases with decreasing porosity, "due to an increase in local fluid velocity and, partly, the enhancement of turbulent transport inside the foam" [52]. The values of h_{vol}, (using non-steady-state methods) for 95% and 70% porous aluminium foams range between 27,000 to 42,500 $W \cdot m^{-3} \cdot K^{-1}$ at a channel Reynolds number, Re_C, of 1,900 [57].

Tian found that fluid flow characteristics in meshes are dominated by orientation and monolith type [18]. Friction factors were independent of velocity. The results are reproduced in Figure 10. When channel height was chosen as the characteristic length, the friction factor was found to depend on pore size and flow direction. Heat transfer was observed to depend on solid conduction and forced convection. For a fixed Reynolds number, porosity and surface area density were the key heat transfer parameters. As the porosity increased, conductive transport was found to decrease while convective heat transport increased.

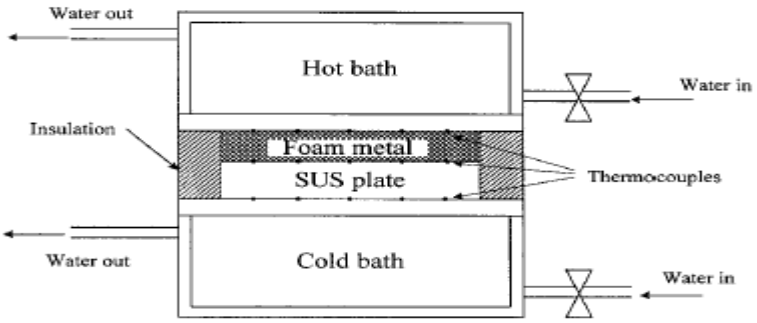

Fig. 1. A schematic diagram of an experimental apparatus for the measurement of effective thermal conductivity.

Figure 7: (Reproduced from from Paek et al. [66]) An apparatus for measuring the effective thermal conductivity (k_{eff}) of an alumimium foam. In this apparatus, uncertainties in the value of k_{eff} are related to the contact of foam ligaments and hot-reservoir/cold-reservoir plates. The uncertainties increase with the increasing pore size.

2.5.3 Approaches to Modelling Heat Transfer in Open-Cell Monoliths

Empirical models of effective heat transfer may or may not deal with radiative heat transfer and most of the models ignore natural convection transfer if the cells are less than 4 mm in diameter [67].

Flow through porous media involves three scales: the pore scale, the representative elementary volume (REV) and the domain scale. The REV is much larger than the pore scale, but smaller than the domain scale. The REV is the length scale at which the characteristics of porous flow hold [68]. For the purposes of this work, transport properties (heat, mass and momentum) are considered to have averaged-volume values at the REV and system models are generated from this scale.

2.5.4 Determination of Metal Foam Interphasial (Convection) Coefficient

2.5.4.1 The Steady-State Determination of the Wall-Convection Coefficient

The steady-state thermal gradient across a monolith under forced-convection cooling cannot be directly observed, since it is not possible to interrogate all the internal surfaces without either disrupting fluid flow or adding thermal mass. It is possible to infer the relative convective effects of one monolith against another by determining the wall convection coefficient, h_w. The wall-convection coefficient is defined by considering the temperature drop along a heat-flux boundary where all heat put into the system must be removed by fluid convection. Several thermal studies of metal foam monoliths have used this method [18, 47, 51, 54, 69, 70].

Tian et al. examined heat transfer and pressure drop for several types of metallic monoliths and packed beds [18]. The group assessed the heat transfer characteristics in terms of Nusselt number and the pressure drop in terms of friction factor. They employed a flow cell (Figure 8) to measure the temperature differential and pressure drop at various Reynolds number values. At steady-state all heat must be removed by convective transfer between the solid surfaces of the wall-bounded monolith and the air passing through. By measuring the temperature drop along the wall and the average change in air temperature across the foam, the authors found the wall-convection coefficient, h_w. The wall-convective coefficient approach has been the dominant mode of steady-state heat transfer experimentation for forced convection in metal foams [18, 47, 51, 54, 64, 65, 70-74].

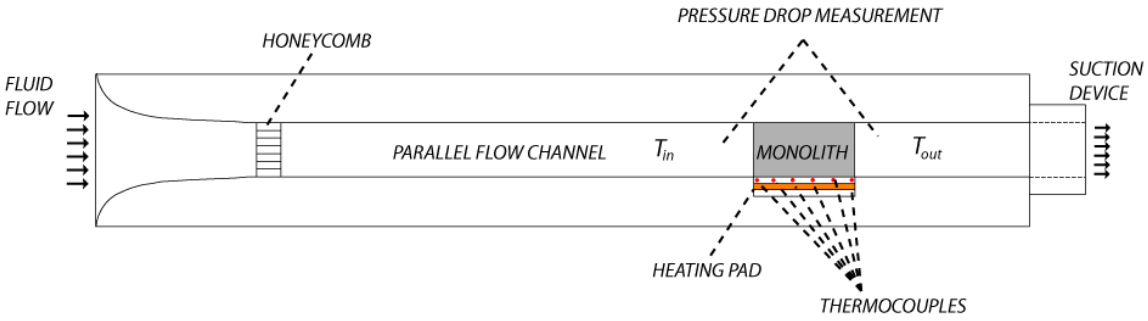

Figure 8: (Reproduced from from Tian et al. [18]) In this experimental system, heat is generated from a resistive heating pad, which conducts heat through its containment wall.

In heat transfer studies of h_w for one-dimensional coolant flow through honeycomb monoliths [75], the local convective heat transfer between a monolith wall and air passing over it is calculated simply as in Equation (2.3):

$$h_w(z) = \frac{q}{T_w(z) - T_f(z)} \tag{2.3}$$

where q is the heat flux into the bottom of the monolith, T_w is the temperature of the wall surface into which heat is flowing, T_f is the temperature of the fluid, ρ_f is the density of the coolant fluid, U_f is its superficial average channel velocity for a characteristic dimension, H, C_{p_f} is the heat capacity of the fluid and z is the dimension along the axis of the coolant flow. The local fluid temperature in (2.3) is calculated through an energy balance between the coolant (air) and the monolith along the length of the convection channel, as per Equation (2.4):

$$T_f(z) = T_{f_{in}} + \frac{q}{\rho_f U_{f_{in}} H C_{p_f}} z \tag{2.4}$$

The average convection coefficient is then taken as a weighted sum of the local convective coefficients in Equation (2.5).

$$\overline{h_w} = \frac{1}{L}\sum_{1}^{n} h(z)\Delta z \tag{2.5}$$

A similar approach is taken to forced convection through a metallic foam monolith. The heat transfer correlation under consideration for the forced-convection foam is outlined in Equations (2.6)-(2.7). Here, the driving force for convection is expressed as ΔT_{avg}.

$$\Delta T_{avg} = \frac{\sum_{i=1}^{n} T_{w_i}}{n} - T_{in} \tag{2.6}$$

$$\overline{h_w} = \frac{q}{A\Delta T_{avg}} \tag{2.7}$$

The energy balances in Equations (2.6)-(2.7) do not try to account for the true convective exchange between the fluid and the solid monolith at all locations within the monolith. However, this method of analysis does provide useful correlation data for heat exchanger design. Tian uses the wall-convection Nusselt number [Equation (2.8)] divided by the cube-root friction factor as a useful heat exchange efficiency number which considers the convective potential for various monoliths of a given effective conductivity against the required kinetic energy inputs to the coolant pumped through it (see Figure 10).

$$Nu = \frac{\overline{h_w} D}{k_f} \tag{2.8}$$

The principal criticism of the wall-convection coefficient is that the convection-parameter, $\overline{h_w}$, is not scalable. Moffat notes: "While undeniably useful in describing the heat transfer from a particular specimen, this approach yields almost no insight into how to make better use of the foam from which the specimen was made. The results apply only for the one specimen size tested and with the foam bonded to the primary surface in one way)" [76]. This work is concerned with improving the steady-state method of recovering the convective parameter in a scalable fashion via comparison of conjugate multi-phase numerical solution of local temperature data (Chapter 3 and Chapter 4).

Steady-state experimental derivation of $\overline{h_w}$ in the literature is generally restricted to high flow rates (within the turbulent Reynolds regime), which is strictly motivated by coolant/heating applications. This work will address low flow rates pertinent to "slow-kinetics" chemical reaction systems (where flow is motivated by mean residence time of reacting species in the monolith).

2.5.4.2 The Non-Steady-State Determination of the Volumetric Convection Coefficient

Another method for deducing the convective heat transfer coefficient is to monitor the transient temperature change of a metal foam placed in the path of a heated fluid stream. These methods monitor the time dependent heating of initially uniform-temperature solid monoliths when placed into a stream of uniform-temperature heating fluid (see Figure 9) in a variation of the "single-blow" transient technique – i.e., hot fluid is used to heat up the porous medium and heat transfer characteristics are measured via the transient of the outlet fluid temperature and the temperature distribution of the wall. These methods assume a one-dimensional thermal gradient in both the fluid and the solid phase through the monolith. This simplification is based on plug flows of fluid and minimal interference from the wall as a heat exchange surface for the air.

Younis describes the fluid [Equation (2.9)] and solid-phase [Equation (2.10)] accumulation of heat energy in the system where the fluid (air) is assumed to have very small thermal mass (so that the rate of heat accumulation in the fluid phase is considered to be negligible) [77]. Similar experimental systems have been paired with more fundamental momentum-balance modelling by Calmidi and Mahajan and/or transient heat transfer treatements by Hwang et al. and Golombock [49],[57], [78].

Steady-state method results are highly dependent on the thermal conductivity of the foam itself, but the transient methods yield coefficients largely independent of conductivity [65]. The transient methods cited are subject to several experimental controls and assumptions aimed at reducing the heat transfer problem to one dimension. The principal criticism of non-steady-state methods similar to the scheme depicted in Figure 9 is that the transient behaviour of the fluid and solid phases do not account for heat transfer between the monolith and containment wall. This problem has been addressed by Jeng's semi-empirical methods to identify convective heat exchange within the monolith vs. heat exchange with containment walls and heater contact surfaces [79] and by Moffat's impedence technique for isolating thermal responses of the monolith to a cooling fluid flow from the contact resistance response of the interface between the monolith and the heating surface [76]. One other issue of reducing the system model to one-dimension is

that the thermal profile of the solid phase boundary must be retro-fitted to the modelled outputs, rather than be treated as an experimental observation. In [79] this fitting is accomplished by introducing fitting factors into the boundary conditions for Equations (2.9) and (2.10). In principle, these fitting factors can account for unique momentum boundary effects at the inlet/outlet of the monolith, but will not capture momentum effects within the foam monolith.

Non-steady-state experimental derivation of $h_{vol}^{'}$ in the literature is generally restricted to high flow rates (within the turbulent Reynolds regime), which is strictly motivated by coolant/heating applications. This work will address low flow rates pertinent to "slow-kinetics" chemical reaction systems (where flow is motivated by mean residence time of reacting species in the monolith).

$$\rho_f C_{p_f} U_f \frac{\partial T_f}{\partial x} = h_{vol}^{'}\left(T_s - T_f\right) \tag{2.9}$$

$$\rho_s C_{p_s} \frac{\partial T_s}{\partial t} = \frac{\partial}{\partial x}\left(k_s \frac{\partial T_s}{\partial x}\right) + h_{vol}^{'}\left(T_f - T_s\right) \tag{2.10}$$

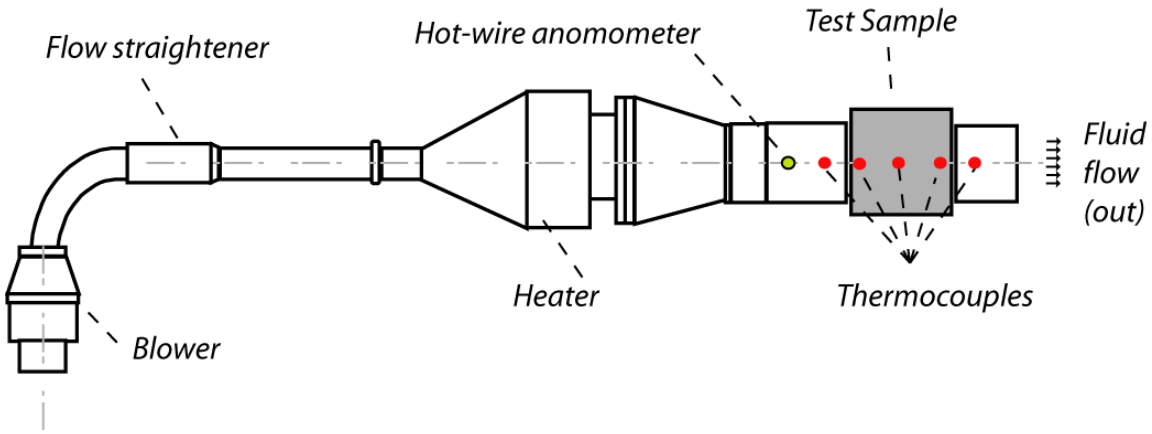

Figure 9: (Reproduced from Younis et al. [77]) Schematic representation of non-steady-state heating experiment with heated fluid passing through an initially cool metal-foam test sample.

2.5.5 Heat Transfer Efficiency Criteria

Metal monolith substrates must provide high surface areas for catalyst support, but they must also conduct heat evolved or absorbed by the reactions at their surfaces. Traditional studies in

heat transfer for meshes and foams have focused on single-purpose heat exchange systems evaluated in terms of fluid-to-monolith heat transfer vs. kinetic losses for turbulent flows ($Nu \cdot f^{-1}$ at high Re_C). Dimensional analysis suggests the use of ($Nu \cdot f^{-1/3}$) to evaluate pump losses [18].

It is widely noted in heat exchange studies that the high volumetric heat dissipation of sintered wire meshes and metal foams is owed in large part to high micro-scale thermal conductivity, which is characterized by the Nusselt number, where $Nu_w = \overline{h_w} \cdot D \cdot k_f^{-1}$ and $\overline{h_w}$ is the surface (wall) convection coefficient $\left(W \cdot m^{-2} \cdot K^{-1}\right)$, D is the characteristic diameter of the flow channel under examination and k_f is the effective thermal conductivity constant of heat-exchange fluid. Figure 10 from [18] illustrates common values of Nu_w for a wide class of open-cell monolith materials including aluminium metal foams.

Since the efficiency of a reactor monolith is a function of reaction rate (proportional to active surface area) and heat transfer, a surface-area-density-weighted volumetric thermal efficiency index is proposed in this work, where α_s is a factor capturing the available convective transport surface area. The dimensional analysis in this case considers a volumetric convective heat transfer coefficient $h_{vol}\left(W \cdot m^{-3} \cdot K^{-1}\right)$ and specific surface area parameter $\alpha_s\left(m^2 \cdot m^{-3}\right)$. The proposed volumetric thermal efficiency quantity, ξ_Q , described in Equation (2.11), captures the ability of a 3D monolith to dissipate heat while minimizing pumping losses for coolant fluid where D is the characteristic diameter for the monolith domain where coolant flows, k_f is the thermal conductivity of the heat exchange fluid, f_H is the friction factor for fluid passing through a monolith-domain channel, ΔP is the average pressure drop through the flow domain, L is the domain fluid-flow length (i.e., length through which the heat-exchange fluid flows through the monolith) , ρ_f is the fluid density and U_{f_m} is the superficial mean bulk velocity of fluid flowing through the monolith.

$$\xi_{\dot{Q}} = \alpha_s^{-1} \cdot \frac{Nu_{vol}}{\sqrt[3]{f_H}}$$

$$Nu_{vol} = \frac{h_{vol} D}{k_f} \tag{2.11}$$

$$f_H = \left(\frac{\Delta P}{L} \cdot D \right) \left(\frac{1}{\frac{1}{2} \rho_f \cdot U_{f_m}^2} \right)$$

The performance metrics of a reactive heat exchange system to be considered in this work are:

- thermal conductivity
- total area for convective heat transfer (surface area of base metallic structure)
- pressure drop of a fluid flowing through the monolith

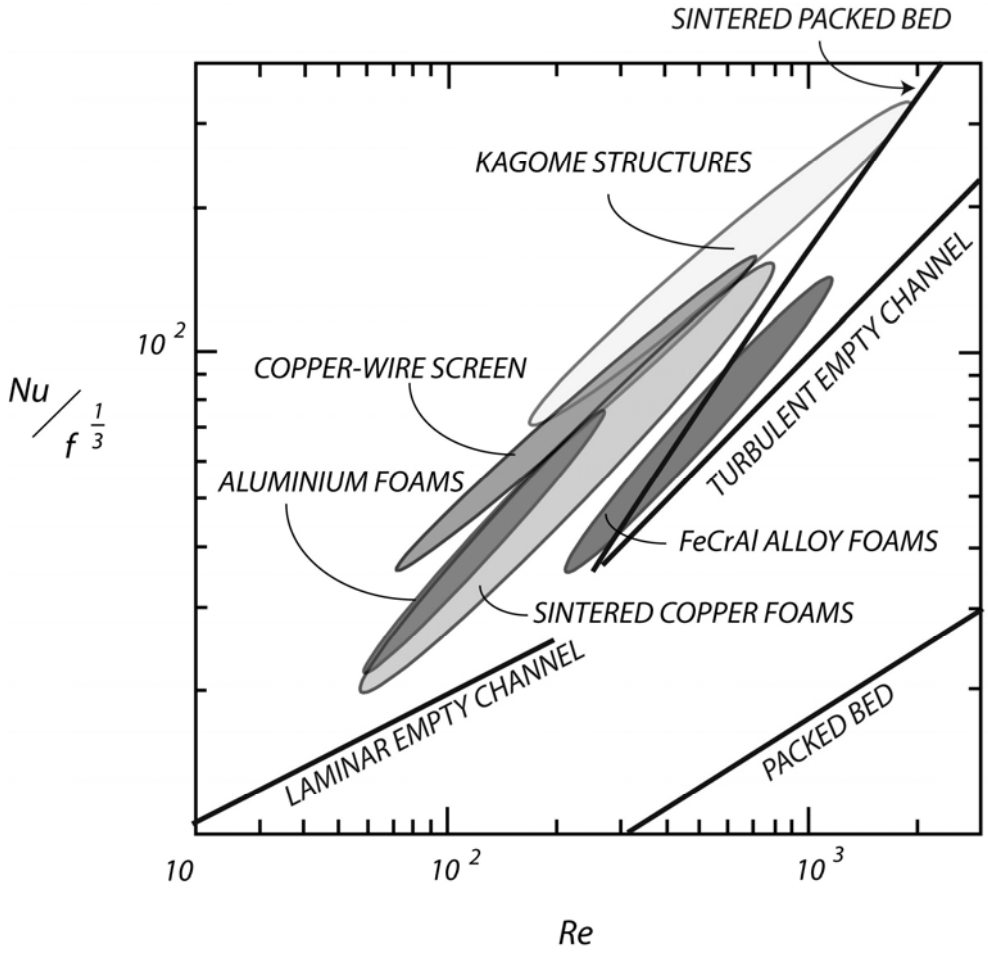

Figure 10: (Taken from Tian [18]) Three thermal efficiency criteria represented graphically. Wire mesh compares favorably to regular-geometry Kagome structures and stochastic metal foams.

Chapter 3: Examining Steady-State Momentum and Heat Transfer Through a Metal-Foam Monolith Under Forced-Convection

In this chapter, the experimental challenge of determining the impact of catalyst coating on convective heat transfer between a metal foam monolith and the reacting fluid flowing through it is introduced. The problem is reduced to the simple case of convective heat transfer between a metal foam monolith and a non-reactive fluid. An experimental strategy is introduced for identifying the convective heat transfer coefficient, h_{vol}, via the fit of observed temperature data with that predicted by a physical model describing the transfer of energy from a controlled solid phase heat flux into a monolith to coolant flowing through that monolith (forced convection). The governing equations and boundary conditions for the physical model are developed and a sample numerical approximation of the model system is demonstrated.

3.1 Essential Objectives of a Convective Heat Transfer Study

The principle objective of this work is to improve the quantitative determination of convective heat transfer in a metallic foam monolith in order to derive a scalable, volumetric convection parameter, h_{vol}, for heat-coupled monolithic reactor design. The essential design of any heat transfer experiment is based on: either (Option A) the establishment of a known thermal gradient in a physical domain and monitoring of the flow of heat from one physical location to another along that gradient, or (Option B) the establishment of a known heat flux into a physical domain and measurement of resulting thermal gradients. Option B is the most practical strategy for monitoring convective heat transfer in a monolith. The required physical information for the convection problem, superficially, is shown (two-dimensionally) in Figure 11 and Figure 12 where $T_{f_{in}}$ and $T_{f_{out}}$ are the temperatures of the coolant fluid, $T_{f(z)}$ is a spatially dependent value of coolant temperature, $T_{w(z)}$ is a solid phase spatially dependent temperature, U_m is a characteristic velocity of the coolant and q is the known heat flux into the solid phase of the

monolith. In this case, a known flux of heat is delivered into the solid phase of a monolith with a known flow of coolant at a known inlet and outlet temperature (and therefore a known increase of heat equal to the known flux, gained via convective exchange with the monolith surfaces). If the heating/cooling system can be driven to steady-state, the thermal gradient will not change with time, and the experimental goal, as per Option B, is reduced to using one or more of the observed temperature gradients to deduce the convective transfer coefficient, h_{vol}.

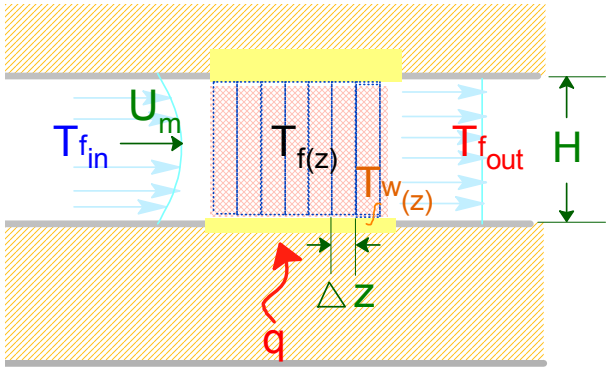

Figure 11: Schematic representation of constant heat flux experiment showing key variables

As per Figure 11, heat convected from the solid to fluid phase of this system must, at steady-state, be equivalent to the known flux, q. Resulting temperature gradients (fluid and solid phase) must be affected by the rate of flow of coolant (i.e., the local velocity of the fluid) and by the solid-phase diffusion (conduction) of heat through the monolith. At any single point within the monolith, provided the velocity of coolant and the solid phase thermal gradient is known, the local convective transfer can be deduced. The temperature gradients can be determined by taking sample temperature data and fitting these to an appropriate model, such that the model gradients (inferred) reconstruct the observed temperature data (observed). In this way a determination of the local convective transport coefficient, h_{vol}, is based on fitting a heat transfer model to observed temperatures in the steady-state system.

3.1.1 Experimental Requirements

Since known solid phase heat flux and known fluid velocity are to be used to deduce a convective heat transfer parameter, key parameters of control in Figure 12 should include:

- a means for controlling the heat flowing into the monolith
- a means for measuring the heat flowing out of the system, via the heated fluid
- a means for determining the steady-state thermal gradients introduced by the heating regime.

Previous steady-state experimental methodologies of recovering the wall-convection coefficient, h_w [18, 47, 51, 54, 64, 65, 70-74] cited in Section 2.5.4.1 have two key drawbacks:

a. Wall-convection methods are only concerned with an apparent two-dimensional heat transfer from the surface of the known heat flux boundary and do not effectively separate fluid-solid convection on the internal monolith surfaces from fluid-solid convection on the heating surface. This means that the parameter h_w is effectively a lumped convection parameter that is valid for a particular foam monolith morphology and dimensional geometry, but may not be useful as a scalable parameter for designing combined heat exchange-reactor devices.

b. Gradient boundary conditions are not accounted for in previous experiments, thereby, preventing the decoupling of the internal monolith-surfaces/coolant convection from heating surface/coolant convection.

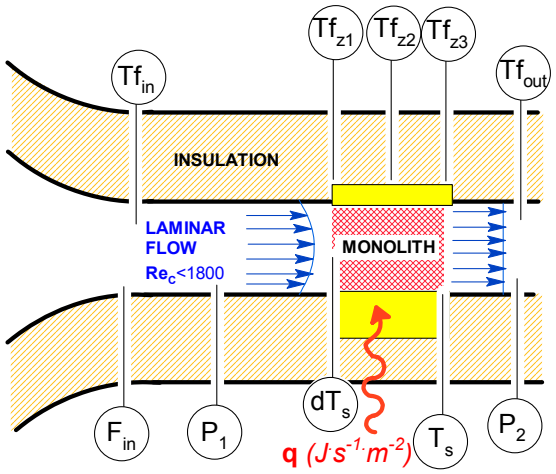

Figure 12: Schematic representation of heat transfer apparatus for determining the impact of catalyst coating on foams. In the steady-state the heat energy into the foam must be balanced by convective transfer from the foam to the air passing through.

The conceptual apparatus in Figure 12 (and rendered as a virtual prototype in Figure 13) introduces a means to overcome points a. and b. above by introducing conductive heat into the bottom of a monolithic foam and monitoring convective transport of heat from the foam to a known quantity of air. The heat conducted into the foam can be set as a steady-state value, q. Measurement of a pressure drop from P_1 and P_2 across the monolith allows sufficient characterization of the fluid flow through the porous media in order to correlate fluid motion with convective heat exchange when fluid temperatures $T_{f_{in}}$, T_{z_i} and $T_{f_{out}}$ are known. Knowledge of the solid-phase temperature boundaries (gradients) at steady-state, particularly the gradient at the monolith entrance, provides the remaining information required to solve the required local convective transfer, $h_{vol}\left(T_{s_z} - T_{f_z}\right)$, required to balance the overall heat transfer in Equation (3.1) from a known flux, $q\left(J \cdot s^{-1}\right)$, to a coolant fluid with a mass flow rate, $F_f\left(kg \cdot s^{-1}\right)$ and heat capacity $Cp_f\left(J \cdot kg^{-1} \cdot K^{-1}\right)$:

$$q = \Delta T_f Cp_f F_f = \sum h_{vol}\left(T_{s_z} - T_{f_z}\right) \tag{3.1}$$

A much more detailed treatment of this generalized heat balance model is outlined in Section 3.3.

Any prototype used to resolve the convective heat transfer parameter must provide sufficient thermal information to decouple diffusive (conductive) heat transfer through the solid phase of the monolith from convective transfer between the solid phase and the fluid phase. An ability to characterize these phenomena will allow an observer to deduce the value of the scalable (geometry independent) convective coefficient, h_{vol}, and to examine the effect catalyst coating has on convective transfer properties.

3.2 Physical Parameters of Interest and a Prototype Device for Measurements Thereof

Driving heat into a solid monolith under forced convective cooling will result in a thermal gradient in both the solid and fluid phases of the system at steady-state. Depending on the geometry and location/direction of heat flux, the thermal gradients can exist in direction both parallel and transverse to the fluid flow. It is possible to correlate the overall convective heat transfer coefficient, h_{vol}, with these observed thermal gradients. The conceptual apparatus required to accomplish this steady-state observation is shown in Figure 12. The observable phenomena of experimental interest in Figure 12 are:

- the spatial distribution of temperatures in the gas phase (temperature gradient)
- the spatial distribution of temperatures in the solid phase (temperature gradient)
- the spatial distribution of fluid velocities in the system, which must be directly related to the amount of heat removed via convective transfer from the steady-state system, equal to heat flux, q, supplied to the system

In a three-dimensional and non-isothermal heat exchanger suggested in Figure 12, the convective heat transfer $h_{vol}\left(T_{s_z} - T_{f_z}\right)$ depends on the local temperature of the solid-phase monolith and the local temperature of coolant in contact with the monolith. It is impractical to examine all internal solid-phase surfaces, and the internal temperatures of the coolant are likewise

impossible to monitor directly. However, the temperatures in either the solid or fluid phase at the boundaries are easy enough to observe. If an appropriate model is used to predict the transfer of heat through internal solid and coolant phases within the monolith body, then the experimental observation of the boundary gradient can be used to infer the value of h_{vol} required for the observed gradient under conditions of known forced heat flux, q, fluid flow rates, F_f, and diffusive transfer parameters for the solid and fluid phases. The ideal boundary gradient under observation will have high ΔT along the observed boundary and a minimum measurement uncertainty. The measurement of ΔT should also be experimentally feasible for a range of monolith samples (wide pore and narrow pore morphologies, coated with catalyst support or not), which suggests that observation of a boundary temperature gradient in the solid phase is not desirable as it would require reproduceable physical contacting of temperature probes with individual strands of metal foam. These considerations were used to build a virtual-apparatus to determine conditions under which measurement of a fluid temperature gradient along the monolith boundary (with no disruptions of flow) would be sufficient to identify h_{vol} in a forced convection system. Figure 13 through Figure 16, show a virtual prototype of the steady-state system of Figure 12. The virtual-prototype apparatus (modelled in COMSOL), solved a simplified system of equations describing the diffusive flux of heat into a solid monolith (see Section 3.3.4 for a description of the physical phenomena) and the convective transfer of that heat into a fluid passing through the monolith at a steady velocity. The virtual prototype was used to estimate the size of observable thermal gradients along monolith boundaries at steady-state (both solid phase and fluid phase). When the conformation of the virtual prototype was altered (such that the monolith was lying flat along the path of the fluid), thermal gradients in the fluid phase were sufficiently high to allow for model fitting the convection parameter, h_{vol} (using the physical model discussed in Section 3.3). The detailed description of how h_{vol} can be deduced from these observations is described at length in Sections 3.3 and 4.5.

Once h_{vol} is determined experimentally (with full model accounting of internal convection surfaces), scaled heat transfer in more complex systems can be modelled where model values h_{vol} are scaled functions of the local pore-Reynolds number for flow through a porous material, or as permeability dependent Reynolds number flows as defined by Kaviany [56] from Equation (3.2) where ρ_f is the fluid density, K is the permeability of the monolith, $\mathbf{u_f}$ is the local velocity of flow and μ is the viscosity of the fluid:

$$\mathrm{Re}_K = \frac{\rho_f \mathbf{u_f} \sqrt{K}}{\mu} \tag{3.2}$$

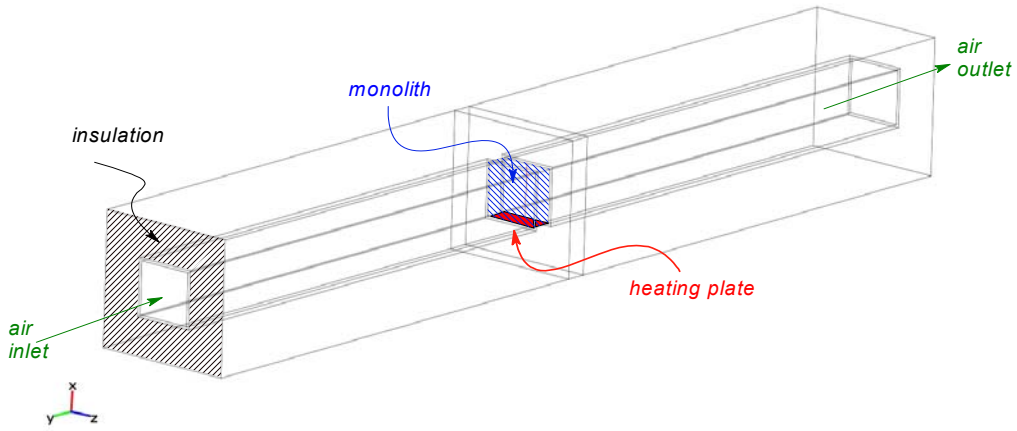

Figure 13: A virtual prototype of the heat-transfer apparatus. Air passed through the heated monolith must have some temperature distribution related to the thermal efficiency of the monolith through which it passes.

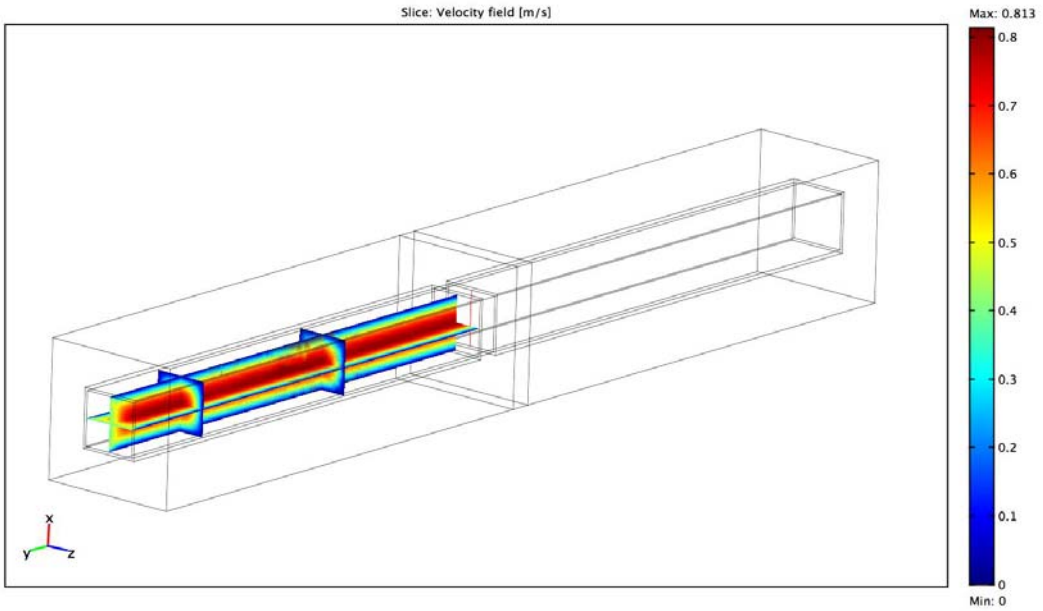

Figure 14: Velocity field of the inlet tube (velocities through the porous monolith and outlet tube have similar fully developed profiles).

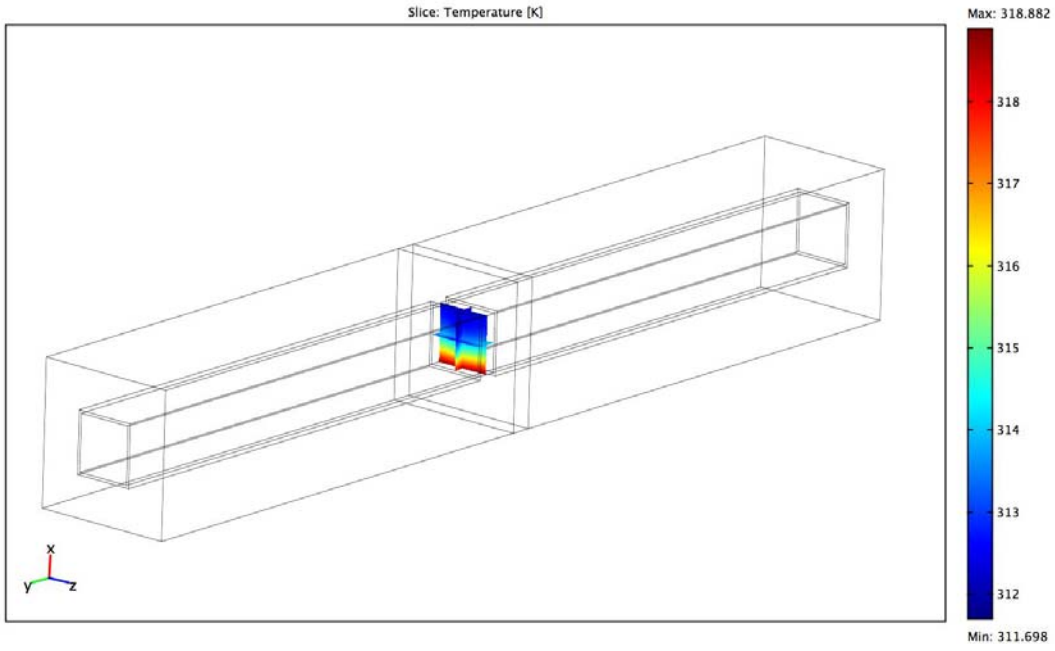

Figure 15: Temperature distribution of the heated monolith with air flowing through it (the monolith is heated by a single 50-Watt strip heater at the bottom).

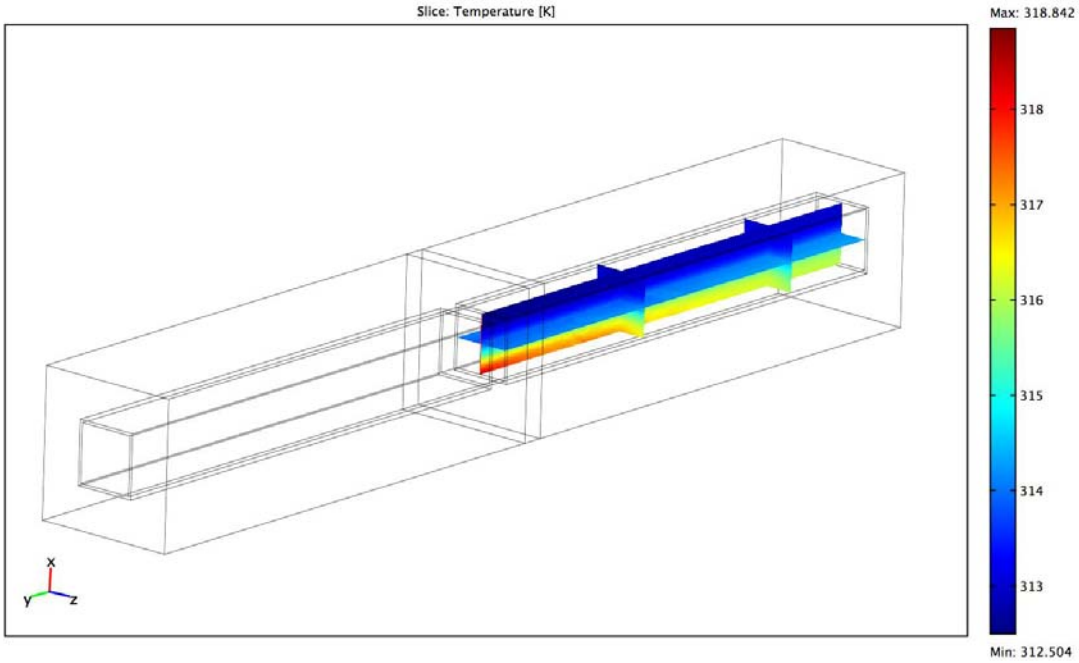

Figure 16: Temperature distribution of air flowing through the outlet after heating through a porous foam heated at its bottom surface.

3.2.1 Heat Transfer: Experimental Considerations

Studies of heat transfer require that contact resistances between the monoliths and heating surfaces are as uniform as possible. The methods of establishing thermal contact include:

- Press-fitting of monolith to heating surface prior to coating of both the monolith and containment wall (Figure 17).
- Use of thermal paste with subsequent press-fitting of coated monolith to bare containment wall (Figure 17).
- Brazing of monolith to heating surface prior to coating of both the monolith and containment wall. This was ruled out because of a need to test a variety of monoliths using the same heating surface (wide pore and narrow pore morphologies, coated with catalyst support or not) in order to determine the relative impact of metal foam morphology vs. catalyst support coating to the values of h_{vol}.

As discussed in Section 3.1.1 the observation of a suitable boundary temperature gradient suggests that fluid temperature measurements at steady-state are desirable because they eliminate the necessity of physically contacting temperature probes (calibrated T-type thermocouples) with strands of metal foam via brazing (and inherent problems for reproducibility and multi-factor analysis across a variety of metal foam morphologies and surface treatments). The non-heating boundaries of the solid phase will need to be insulated to simplify boundary conditions, although the entry and exit boundaries will require knowledge (at least) of the solid-phase temperature gradients at steady-state.

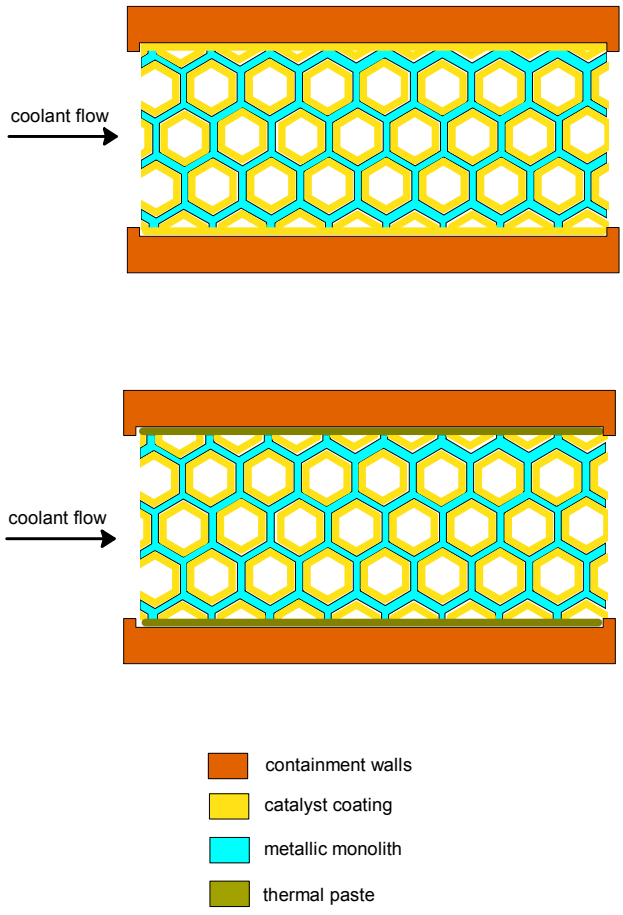

Figure 17: Methods for connecting metal monoliths to heat transfer sinks (containment walls) for heat transfer studies and for integrated reactor prototyping. Above: non-reactive monolith is fit to the wall prior to catalyst coating of both monolith and wall. Below: reactive, coated monolith is fitted to the containment wall with thermal paste.

3.2.2 Momentum Transfer: Experimental Considerations

Key fluid flow criteria for experimentation include:

- Knowledge of local coolant flow velocities, since the overall heat balance requires accounting of the heat exchanged to the gas phase in the forced-convection system.
- The difference in local velocities for the system under test should be minimized in order to maintain the scalability of the relationship between h_{vol} and local Reynolds number as described in Equation (3.2). This relationship is useful for design purposes when the local value of h_{vol} changes in reactive systems due to mass-change (generation and consumption of "coolant" species) as described in Chapter 6.

For the purposes of this work, the stochastic nature of the metal foam monolith is assumed to promote near-plug flow velocity profiles at any flow rates above creeping flow as it is not computationally feasible to model entire coupled transport systems with full resolution of the complex flow field of a coolant through a metal foam (although the uncoupled flow fields are solvable using Lattice-Boltzmann solution algorithms).

3.3 A Two-Phase Energy Balance Model for the Convection Experiment

3.3.1 Model Overview

As discussed in Section 3.2, a model of the heat transfer in the solid phase, heat transfer in the fluid phase and momentum transfer of the fluid flowing through the monolith is required to determine the value of the convective transfer parameter, h_{vol}, based on observation of coolant temperatures along the monolith boundary. The two heat transfer phenomena and one momentum transfer phenomenon are accounted using a physical model of fundamental equations (or experimentally valid empirical approximations) with suitable boundary conditions. Finite-element analysis (FEA) is used to approximate the transport equations in piecewise fashion over the domain of interest where the model-convergence criterion is continuity of the approximate solution over the domain such that boundary conditions are met.

3.3.2 Domain Description

The domain of the model heat exchanger under consideration is a two-dimensional cross-section of a three-dimensional, two-phase (solid/fluid) system with a known heat flux entering the solid phase at one face via conductive transfer. This is depicted as a schematic in Figure 18. For computational purposes, the model domain considered is a two-dimensional symmetry plane through a three-dimensional monolith system measuring 5.08 cm × 3.81 cm × 1.27 cm. A pressure-driven flow of fluid is forced though the model cross-section. The fluid phase has a known amount of heat at the entry and exchanges heat with the solid phase via convection. A normal diffusive heat source is supplied on the bottom boundary. Full boundary conditions for the system are described in Section 3.3.7 and in Figure 19 on Page 45.

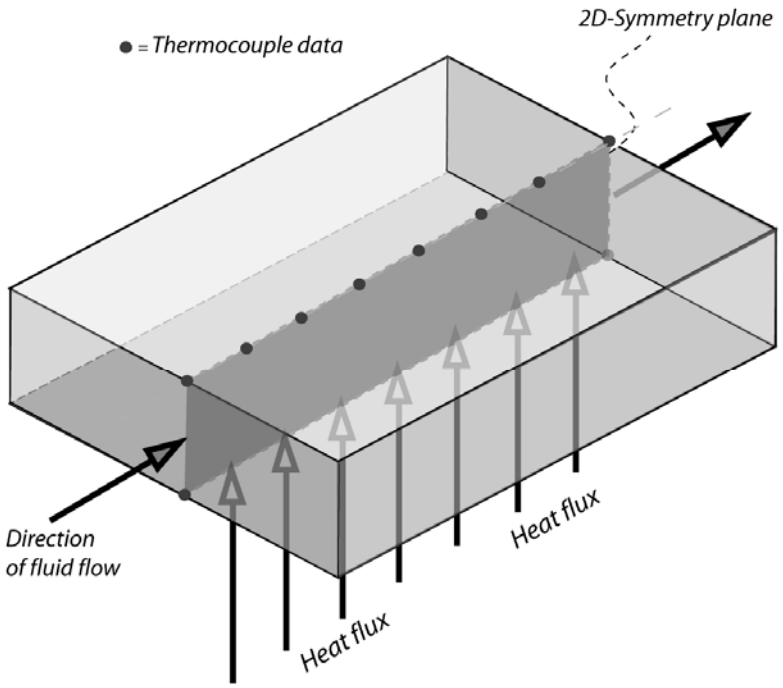

Figure 18: Schematic view of the system under study. Heat is driven into the bottom side of the foam monolith and the temperature of the fluid passing through the foam is monitored along the top midline. Model predictions are calculated for the 2D cross-section along the symmetry line of the monolith.

3.3.3 Assumptions

- There is no solid-phase convective transport of heat. All solid-phase transport is via diffusion (conduction) only and heat is added or removed to the solid phase via convection with the fluid phase.
- The velocity and thermal entry length of fluid inside the domain is negligible [56].
- Flow through porous media involves three scales: the pore scale, the representative elementary volume (REV) and the domain scale. The REV is much larger than the pore scale, but smaller than the domain scale. The REV is the length scale at which the characteristics of porous flow hold [68]. For the purposes of this work, transport properties (heat, mass and momentum) are considered to have averaged-volume values at the REV and system models are generated from this scale.
- Local fluid mixing (due to the tortuous path) is ignored in this model.
- No convective or conductive heat transfer occurs at insulated boundaries.
- All significant heat flux into the system is via conduction into the heated boundary.
- Convective heat transfer parameters are temperature-independent.
- Convection heat transfer parameters are independent of the solid-phase heat flux into the domain [49].
- Fluid flow has a plug profile through all space within the domain beyond the entry length for velocity.
- All heat flux into the system is removed via convection of fluid (i.e., there is no accumulation of heat inside the domain of interest).
- The thermal conductivity of the solid phase does not vary with temperature within the operating conditions simulated here.
- No radiative heat transfer occurs within the experimental parameters of this work.

The model considers thermal, mass and momentum transport in the fluid phase, thermal transport in the solid phase, and interphasial heat transfer between the fluid and solid phase. A description of the individual transport processes and associated governing equations are presented in the following sub-sections.

3.3.4 Heat Transfer in the Solid Phase

The generalized conduction-convection heat transport equation can be written as follows:

$$\nabla \bullet \left(-k_{eff} \nabla T_s + \rho_s C_{p_s} \mathbf{v}_s T_s \right) = Q \tag{3.3}$$

where k_s is the thermal conductivity of aluminium, ε is the porosity of the foam monolith and $k_{eff} = f\left(k_s, \varepsilon\right)$, T_s is the temperature of the solid, ρ_s is the mass density of the foam such that $\rho_s = \left(1 - \varepsilon\right) \rho_{Al}$ where ρ_{Al} is the density of aluminium, C_{p_s} is the constant-pressure thermal capacity of aluminium and $\mathbf{v}_s$ is the velocity of the solid phase and Q is the heat-source term. Since the solid phase has no velocity the equation is simplified:

$$\nabla \bullet \left(-k_{eff} \nabla T_s \right) = Q \tag{3.4}$$

In a steady-state system, the source term, Q, must be equivalent to the interphasial heat transfer between the solid phase and the fluid passing through it over the domain in question, so we write:

$$\nabla \bullet \left(-k_{eff} \nabla T_s \right) = h_{vol} \left(T_s - T_f \right) \tag{3.5}$$

where h_{vol} is the effective volumetric convective coefficient between the solid phase and the coolant fluid in units of $W \cdot m^{-3} \cdot K^{-1}$ and T_f is the temperature of the fluid phase.

3.3.5 Heat Transfer in the Fluid Phase

In the case of the fluid phase, we do not discount fluid velocity and recognize that the heat source term between the fluid and the monolith must be opposite to that in Equation (3.5). We are left with Equation (3.6), where $\rho_f = \varepsilon \rho_{air}$ and $k_f = \varepsilon k_{air}$ (where ε is the porosity of the

foam monolith) and $\mathbf{v}_f$ is the velocity vector of the coolant fluid flow through the porous monolith.

$$\nabla\bullet\left(-k_f\nabla T_f + \rho_f C_{p_f}\mathbf{v}_f T_f\right) = h_{vol}\left(T_f - T_s\right) \tag{3.6}$$

3.3.6 Momentum Transfer in the Fluid Phase

The fluid velocity in the monolith must be computed to solve the energy balance equation (3.6) for the fluid phase. The Darcy-Forchheimer equation captures momentum-transfer behaviour of fluid where the bulk movement resemples a plug flow. The Darcy-Forchheimer equation of Equation (2.1) can be re-written in vector notation:

$$-\nabla\mathbf{P} = \frac{\mu}{\mathrm{K}}\mathbf{v} + C_F\rho|\mathbf{v}|\mathbf{v} \tag{3.7}$$

The problem of resolving the pressure-velocity coupling is remedied by solving the quadratic function in for the velocity vector and then substituting this value into the continuity equation (3.8), which must be satisfied in a conservative fluid flow field [80-82].

$$\nabla\bullet(\rho\mathbf{v}) = 0 \tag{3.8}$$

In Equation (3.7) the velocity vector, $\mathbf{v}$, is a function of the magnitude of the pressure gradient as well as its direction.

Let

$$\mathbf{v} = -f\left(|\nabla\mathbf{P}|\right)\nabla\mathbf{P} \tag{3.9}$$

and

$$|\mathbf{v}| = f\left(|\nabla\mathbf{P}|\right)|\nabla\mathbf{P}| \tag{3.10}$$

and substitute into (3.7) gives:

$$-\nabla\mathbf{P} = \frac{\mu}{\mathrm{K}}\left(-f\left(|\nabla\mathbf{P}|\right)\nabla\mathbf{P}\right) + C_F\left(f\left(|\nabla\mathbf{P}|\right)|\nabla\mathbf{P}|\right)\left(-f\left(|\nabla\mathbf{P}|\right)\nabla\mathbf{P}\right) \tag{3.11}$$

Equation (3.11) simplifies to

$$C_F \left|\nabla \mathbf{P}\right| \left(f\left(\left|\nabla \mathbf{P}\right|\right)\right)^2 + \frac{\mu}{\mathrm{K}} \left(f\left(\left|\nabla \mathbf{P}\right|\right)\right) - 1 = 0 \tag{3.12}$$

The quadratic root of Equation (3.12) has one real solution:

$$f\left(\left|\nabla \mathbf{P}\right|\right) = \frac{2}{\frac{\mu}{\mathrm{K}} + \sqrt{\left(\frac{\mu}{\mathrm{K}}\right)^2 + 4C_F \left|\nabla \mathbf{P}\right|}} \tag{3.13}$$

Substituting $\mathbf{v} = -f\left(\left|\nabla \mathbf{P}\right|\right)\nabla \mathbf{P}$ into (3.8) gives the final governing equation for momentum transfer. By inspection, it can be seen that when the Forchheimer coefficient, C_F, is 0, the governing equation reduces to the momentum transfer governing equation for Darcy model flows.

$$\nabla \bullet \left(\frac{2\rho_f}{\frac{\mu}{\mathrm{K}} + \sqrt{\left(\frac{\mu}{\mathrm{K}}\right)^2 + 4C_F \left|\nabla \mathbf{P}\right|}} \left(-\nabla \mathbf{P}\right) \right) = 0 \tag{3.14}$$

The three governing equations (3.5), (3.6) and (3.14) are coupled through the temperature, pressure and velocity variables. The material properties of the solid phase are considered constant over the range of temperatures and pressures investigated, but the properties of the compressible fluid vary with temperature and pressure, where T_f is in degrees Kelvin, p_f in Pascals. The fluid density of air is calculated from the ideal gas law in Equation (3.15). Sample empirical relationships for the properties of air are given in Equations (3.16)-(3.18).

$$\rho_{air} = MW_{air} \frac{p_{air}}{R T_{air}} \tag{3.15}$$

$$k_{air} = 10^{0.8616 \ \log_{10}\left(\left|T_{air}\right|\right) - 3.7142} \tag{3.16}$$

$$C_{p_{air}} = 0.0769 \ T_{air} + 1076.9 \tag{3.17}$$

$$\mu_{air} = -7.887 \times 10^{-12} T_{air}^2 + 4.427 \times 10^{-8} T_{air} + 5.204 \times 10^{-6} \tag{3.18}$$

3.3.7 Boundary Conditions

The following boundary conditions are imposed on the above model. All boundary conditions chosen are physically meaningful and/or experimentally realizable conditions. The four boundaries and the flow directions are shown in Figure 19 below:

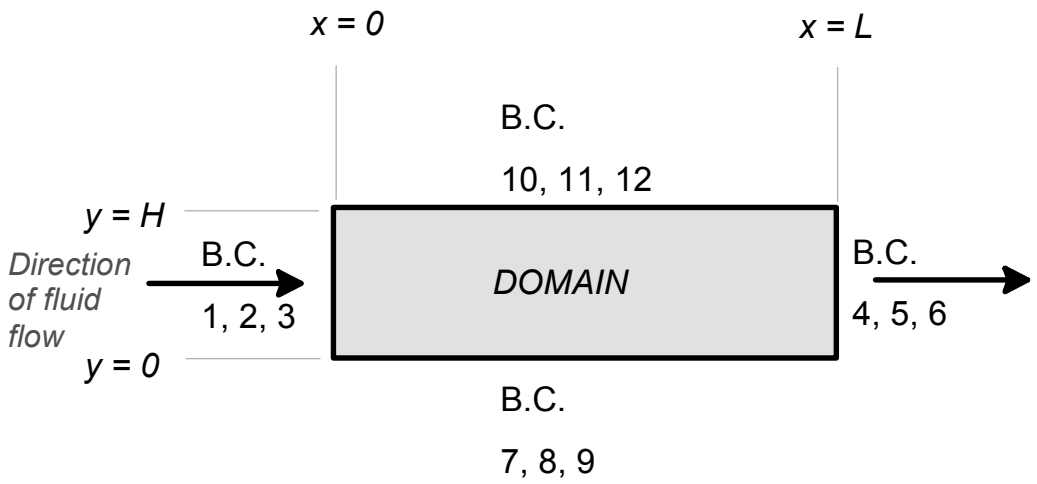

Figure 19: Twelve boundary conditions imposed on the two-phase forced convection model for air flowing through a metal foam.

3.3.7.1 Left Boundary for *x=0*, for *y=0* to *H*

B.C. 1 (Known inlet face temperature [solid phase according to an observed temperature gradient from experimental data and modelled as a second-order polynomial, $f\left(y, Ts|_{x=0,y=0}\right)$])

$$\left.\frac{dT_s}{dy}\right|_{x=0} = f\left(y, T_s|_{x=0,y=0}\right)$$

B.C. 2 (Known inlet temperature of fluid stream)

$$T_f|_{x=0} = T_{f_{in}}$$

B.C. 3 (Known pressure at inlet)

$$p\big|_{x=0} = p_{in}$$

3.3.7.2 Right Boundary for *x=L*, for *y=0* to *H*

B.C. 4 (Zero solid phase heat flux at the boundary.)

$$-k_s \left.\frac{dT_s}{dx}\right|_{x=L} = 0$$

B.C. 5 (Heat removed from the system is contained in the fluid phase with no solid- phase contribution and that this heat is removed exclusively via convection).

$$-k_f \left.\frac{dT_f}{dx}\right|_{x=L} = 0$$

B.C. 6 (Known pressure at outlet)

$$p\big|_{x=L} = p_{out}$$

3.3.7.3 Bottom Boundary for *y=0*, and *x=0* to *L*

B.C. 7 (Known, uniform, heat flux into system)

$$-k_s A_h \left.\frac{dT_s}{dy}\right|_{y=0} = q_{in}$$

B.C. 8 (Insulated boundary)

$$-k_f A_h \left.\frac{dT_f}{dy}\right|_{y=0} = 0$$

B.C. 9 (No normal pressure gradient at boundary)

$$\left.\frac{dp}{dy}\right|_{y=0} = 0$$

3.3.7.4 Top Boundary for *y=H*, and *x=0* to *L*

B.C. 10 (Insulated boundary)

$$-k_s A_h \left.\frac{dT_s}{dy}\right|_{y=H} = 0$$

B.C. 11 (Insulated boundary)

$$-k_f A_h \left.\frac{dT_f}{dy}\right|_{y=H} = 0$$

B.C. 12 (No normal pressure gradient at boundary)

$$\left.\frac{dp}{dy}\right|_{y=H} = 0$$

3.4 Solution Method

The governing Equations (3.5), (3.6) and (3.14), along with their required boundary conditions, were solved using COMSOL Multiphysics, a commercial multiphysics finite-element PDE solver. The UMFPACK linear direct numerical solver in COMSOL was used on an 842-node monolith domain whose boundaries and governing equations are described in Section 3.3. The model was tested to demonstrate that the fitted solutions to the governing equations subject to boundary conditions 1-12 do not change due to changes in internal grid geometry. The model was also

tested to ensure that it obeyed conservation of mass, momentum and energy in the model outputs.

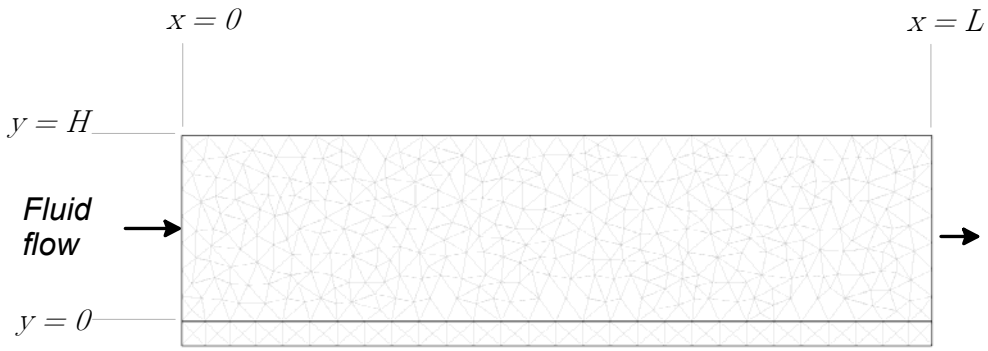

Figure 20: An 842-element mesh used to solve three governing heat transfer equations in COMSOL

3.5 Model Predictions

A sample prediction of the model is presented for a 10 ppi uncoated aluminium foam sample with dimensions of 5.08 cm × 3.81cm × 1.27 cm cooled with air at a flow condition of Re_C=180 and 2.85 W of heating on the bottom surface. The specific boundary conditions are entered in Table 1.

Example results of the model predictions are shown in Figure 21 and Figure 22, which show the 2-D solid and fluid-phase isotherms through the monolith's midline cross-section (as indicated in Figure 18). Solid-phase and fluid-phase temperature gradients are significant in both the horizontal and vertical directions through much of the monolith as illustrated. The model prediction of internal solid-phase temperature gradients is useful for predicting the temperature-sensitive reaction kinetics of any working heat-coupled reactor. It is notable that there are substantial solid-phase temperature gradients at the entrance of the monolith, which one would expect to amplify effects on heat-evolving mass-transfer kinetics.

In Figure 23, the value of fluid phase temperatures at the boundary $y=H$ (as per Figure 20) are recorded for several grid mesh configurations. The results of the coarse meshes and finer meshes are in accordance, indicating that the model is self-consistent. As reported in Table 2, the integral of the inlet and outlet values for heat (diffusive + convective flux) are balanced as are those for mass & momentum, indicating that the model is does not violate conservation.

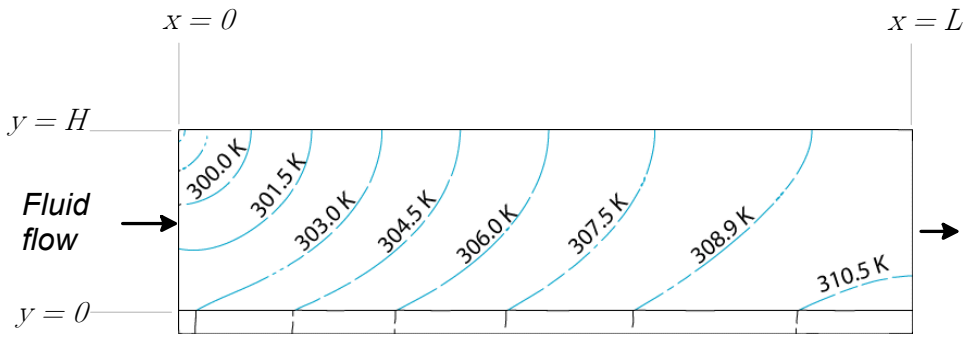

Figure 21: Model estimates for the isothermal profile inside the solid phase of a 10 ppi aluminium foam under 2.85 W heating with forced air at Reynolds number 180.

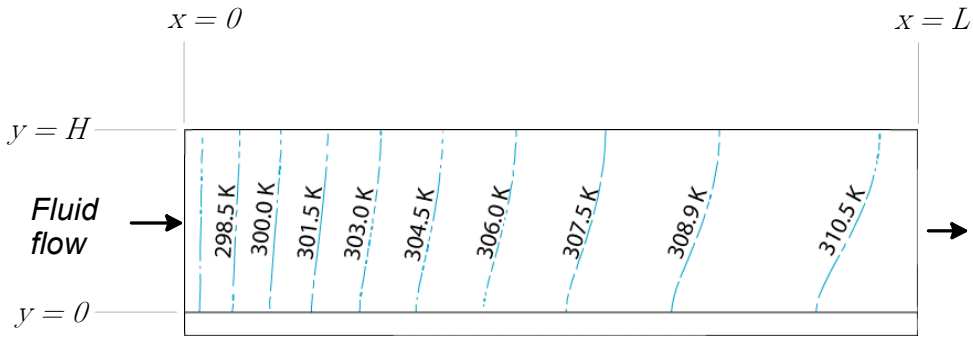

Figure 22: Model estimates for the isothermal profile in the fluid phase of a 10 ppi aluminium foam under 2.85 W heating with forced air at Reynolds number 180.

Table 1: Model input parameters for 10 ppi foam under 1.4W heating at $Re_C = 180$

INLET TEMPERATURE	*Temp (K)*	*x = (m)*	*y = (m)*
Ts_{in}	*307.65*	*0*	*H*
Ts_{in}	*309.25*	*0*	*H/2*
Ts_{in}	*310.04*	*0*	*0*
Ts_{in}	*296.27*	*0*	*all*
OUTLET TEMPERATURE	*Temp (K)*	*x = (m)*	*y = (m)*
Ts_{out}	*313.18*	*L*	*0*
BOTTOM FLUX	*$W{\cdot}m^{-2}{\cdot}s^{-1}$*	*x=(m)*	*y=(m)*
q	*1477*	*0..L (m)*	*0 (m)*
PRESSURE	*Pa*	*x=(m)*	*y=(m)*
p_{in}	*101329.7*	*0*	*0..H*
p_{out}	*101325*	*L*	*0..H*
PHYSICAL PARAMETERS	*Value*	*Units*	*Location*
C_F	*69*		*all*
K	*3.0E-08*	m^2	*all*
k_{eff}	*6.22809*	$W{\cdot}m^{-1}{\cdot}K^{-1}$	*all*
ε	*0.081*	*0.929*	*all*
h_{vol}	*10,000*	$W{\cdot}m^{-3}{\cdot}K^{-1}$	*all*
ρ_s	*271*	$kg{\cdot}m^{-3}$	*all*
Cp_s	*6.885*	$J{\cdot}kg^{-1}{\cdot}K^{-1}$	*all*
PHYSICAL CORRELATIONS		*Units*	*Location*
$\rho_{air} = MW_{air} p \cdot \left(RT_f\right)^{-1}$		$kg{\cdot}m^{-3}$	*all*
$\mu_{air} = -7.887 \times 10^{-12} T_{air}^2 + 4.427 \times 10^{-8} T_{air} + 5.204 \times 10^{-6}$		$kg{\cdot}m^{-1}{\cdot}s^{-1}$	*all*
$C_{p_{air}} = 0.0769\ T_{air} + 1076.9$		$J{\cdot}kg^{-1}{\cdot}K^{-1}$	*all*
$k_{air} = 10^{0.8616\ \log_{10}(\lvert T_{air}\rvert)-3.7142}$		$W{\cdot}m^{-1}{\cdot}K^{-1}$	*local*

Table 2: Energy, mass and momentum balance in COMSOL heat-transfer model

ENERGY BALANCE				
No. of elements	*292*	*842*	*3368*	*13472*
$J \cdot m^2 \cdot s^{-1}$ at x=0 (in)	*701.83029*	*701.36998*	*701.19849*	*701.11786*
$J \cdot m^2 \cdot s^{-1}$ at x=L (out)	*742.27615*	*742.41235*	*742.32987*	*742.33268*
$J \cdot m^2 \cdot s^{-1}$ at y=H (out)	*1.03915*	*0.53950*	*0.25606*	*0.12365*
$J \cdot m^2 \cdot s^{-1}$ y=0 (in)	*41.00051*	*40.98486*	*41.17904*	*41.24611*
NET BALANCE	*-0.484504*	*-0.597007*	*-0.208396*	*-0.092364*

MASS & MOMENTUM BALANCE				
No. of elements	*292*	*842*	*3368*	*13472*
$kg \cdot m^2 \cdot s^{-1}$ at x=0 (in)	*0.00217*	*0.00217*	*0.00217*	*0.00217*
$kg \cdot m^2 \cdot s^{-1}$ at x=L (out)	*0.00217*	*0.00217*	*0.00217*	*0.00217*
NET BALANCE	*0.00000*	*0.00000*	*0.00000*	*0.00000*

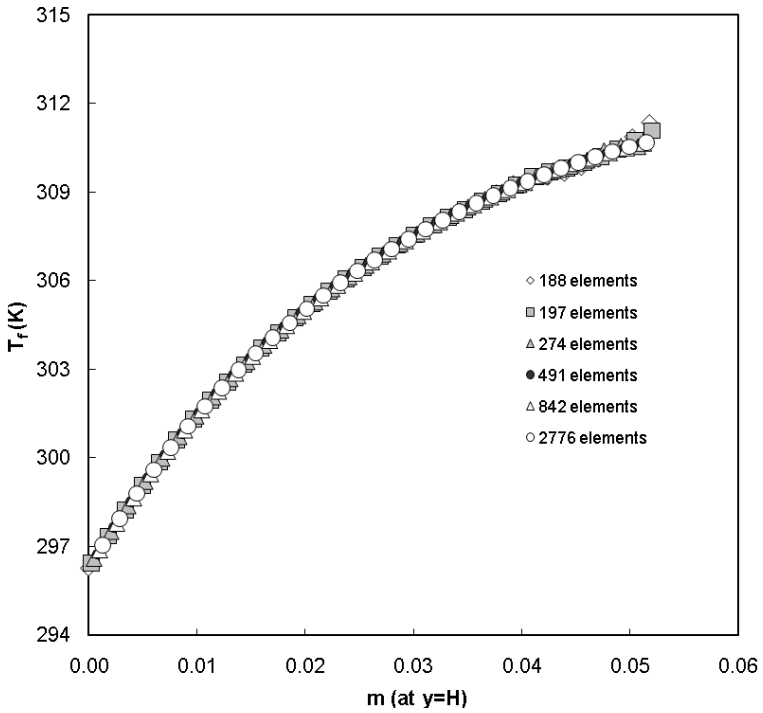

Figure 23: Fluid temperature profiles at the upper boundary of the monolith domain (y=H) recovered using several meshes of the model of 10 ppi aluminium foam under forced convection at $Re_C = 180$ and 2.85 W heating with h_{vol} of 10,000 $\left(W \cdot m^{-3} \cdot K^{-1}\right)$.

Chapter 4: Experimental Protocol

In Chapter 4, the experimental procedure used to determine the Darcy-Forchheimer flow parameters, K and C_F; the conductive heat transfer coefficient of experimental metal foam, k_{eff}; and the convective heat transfer coefficient, h_{vol}, is discussed.

4.1 Materials

Aluminium metal foam samples were acquired from ERG (ERG Materials and Aerospace, (Oakland, CA, U.S.). Samples tested were 6101-T6 aluminium alloy metal foams in 10, 20 and 40 pore-per-inch (ppi) morphologies at relative densities ranging from 8% to 12%. Half of the samples were surface modified by anodization (Type III anodization performed by the manufacturer to a specification of a 76-micron thick layer of Al_2O_3 catalyst support). The anodized layer specification was one order of magnitude smaller than the diameter of the metal strands of the monolith which connect the pores together. All metal foam samples had dimensions of approximately 13mm×38 mm×51 mm. with a volume of 25 cm^3. Where thermal contact was required for heat transfer experiments, Wakefield Type 120 (Wakefield Solutions, Pelham, NH, U.S.) thermal joint compound grease was applied to fill microcracks and maximize heat transfer area between flat surfaces. Insulation materials consisted of Owens Corning Cellfortec 300 polystyrene (Owens Corning Canada, Scarborough, ON, Can.) with insulated joints formed from Rutland refractory furnace cement (Rutland Fire Clay Company, Rutland, VT, U.S.).

4.2 Instrumentation

4.2.1 Pressure

Pressure drops were monitored with a Dwyer Mark II Model 25 liquid-tube manometer or an Omega PX275 digital differential pressure transducer (Omega Engineering Inc., Stamford, CT,

U.S.). The digital transducer signal was calibrated against the liquid-tube manometer, which is dependent on the physical density of a stable fluid.

4.2.2 Temperature

Contact-surface and flowing-fluid temperatures were measured with Omega 36-gauge T-type insulated thermocouples (Omega Engineering Inc.) whose voltage is monitored by an Automation Direct Terminator Input-Output control module mated to LabView through an OPC (*Object-Embedded Linking for Process Control*) network. The thermocouples were encapsulated in thin plastic and individually two-point calibrated in melting ice water and boiling water against a glass-mercury thermometer (known to have a linear temperature response) at $2°C$ intervals between $0°C$ and $100°C$. The calibrated voltage outputs were logged to a lookup table for reference. Surface gradients were measured using a FLIR Thermovision A40 camera (FLIR Systems Inc., Portland, OR, U.S.) with emissivity calibrated to a contact thermocouple-monitored aluminium sheet at known temperature and also to the same aluminium sheet coated with an infrared transparent black tape (to calibrate to the black coated anodized metal foams)..

4.2.3 Fluid Velocity

Fluid velocities were measured with an Alnor Type 8500 hotwire anemometer with a platinum resistance wire (TSI/Alnor Instrument Company, Shoreview, MN, U.S.). The unit was recalibrated to zero velocity before each measurement. Higher velocity readings were validated by measurement of a known air-flow (differential pressure drop of room-temperature air through a large duct of known diameter and negligible wall friction).

4.3 Determination of Permeability

The experimental setup for the determination of permeability characteristics of metal foams is shown in Figure 24. The basic experimental measurements include pressure drop across the foam sample and fluid flow rate. The foam samples were placed in a milled foam channel made of insulating polystyrene with air forced through them lengthwise (51 mm). The pressure drop

between the foam entry and foam exit were recorded on a Dwyer Mark II manometer (Dwyer Instruments, Michigan City, IN, U.S.) with 3 mm pressure taps placed 5 mm before the entrance and 5 mm beyond the exit of the monolith. The superficial Darcy velocity, $\mathbf{v}_f$, was measured using an Alnar Type 8500 hot-wire anemometer placed 25 mm past the fluid exit of the foam along the flow midline of the foam (Figure 24). Pressure-velocity values were noted for a range of flow rates between 0 and 0.8 m s^{-1}, corresponding to channel-based Reynolds numbers of 0 to 1,000. This data was then regressed against the Darcy-Forchheimer relationship (2.1) to recover the permeability K, and the Forchheimer coefficient, C_F for varied channel-scale Reynolds numbers Re_C and pore-scale Reynolds numbers Re_P. The recovered permeability and Forchheimer parameters were subsequently used to model the pressure drop of fluid passing through the monolith.

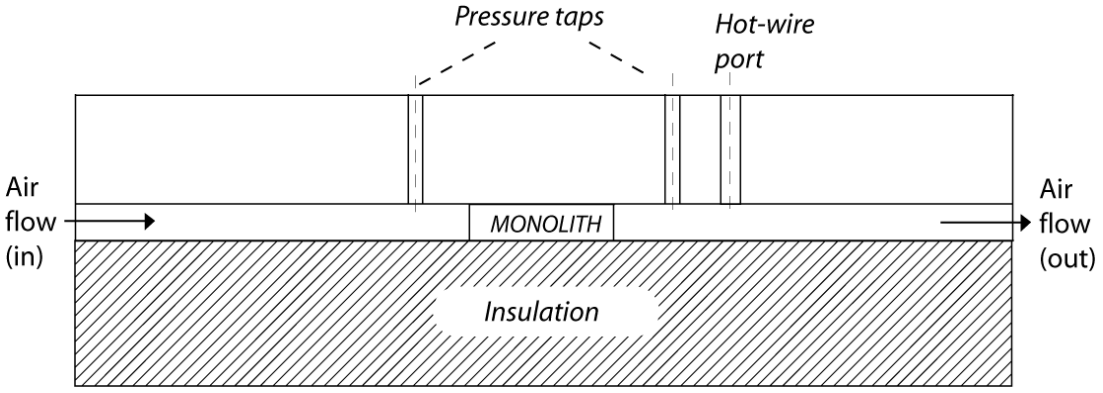

Figure 24: Schematic representation of the experimental setup for permeability measurement. A hot-wire anemometer was used to measure the air flow velocity after full development (mixing) through the porous monolith. Pressure drop was measured using a manometer.

4.4 Determination of Effective Conductivity of Metal Foam

The effective conductivity of the metal foam monoliths was determined using the experimental setup shown in Figure 25, which is based on the Searle's-bar method that uses the equivalence of heat fluxes into and out of the foam at steady-state to infer the foam conductivity [53]. The monolith sample was placed between two 4130 steel alloy samples of known thermal

conductivity. One steel sample is in thermal contact with an isothermal stream of cold water and the other with a stream of hot water.

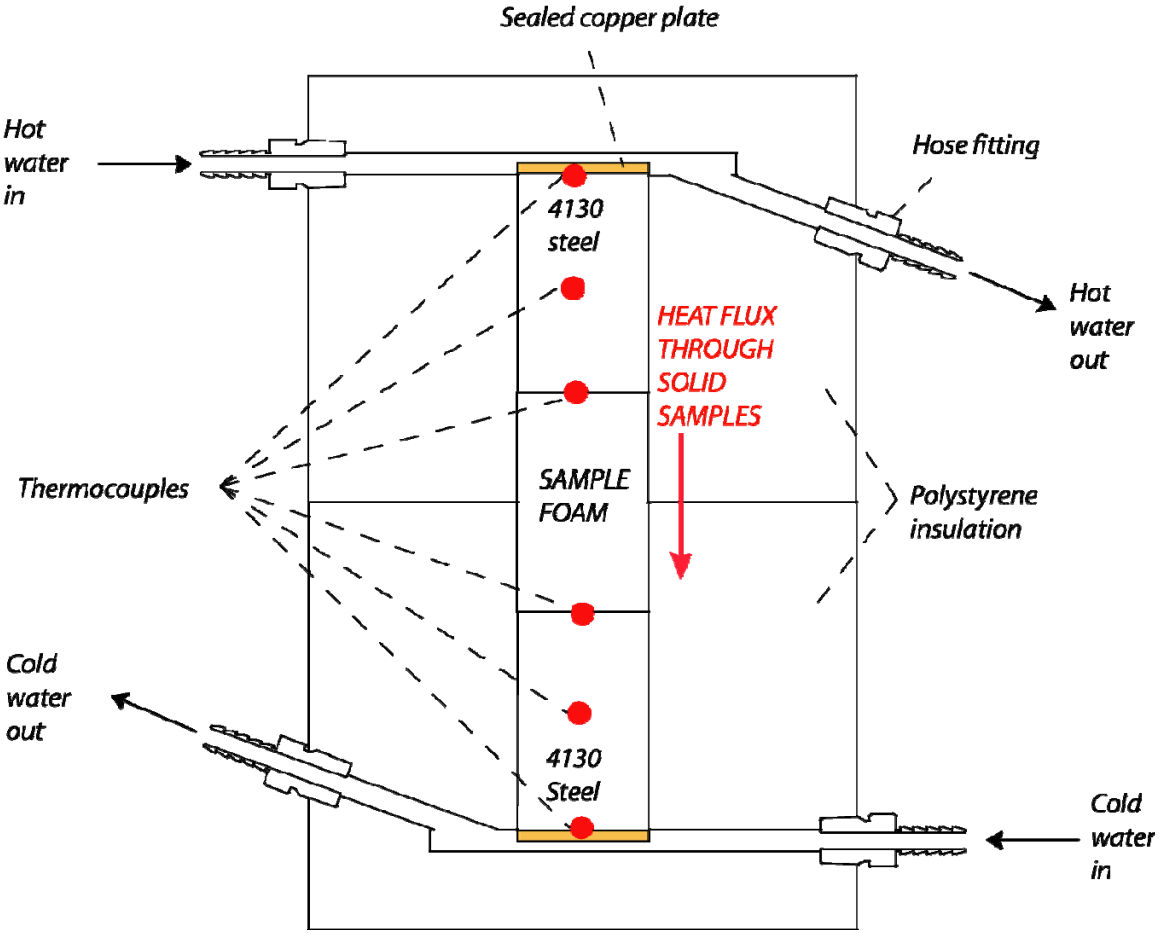

Figure 25: The effective conductivity of the monoliths is determined by driving heat through a series-resistance between hot and cold reservoirs of water pumped at a steady flow rate. The known conductivity of the 4130 steel samples allows for the determination of the effective monolith conductivity at steady-state.

All thermal contact surfaces were made by press fitting samples and known standards to 110-alloy copper sheet using Wakefield Type 120 thermal joint compound. In the case of coated foams, flux-surface Al_2O_3 was removed with fine sandpaper in order to allow direct thermal contact with the bare aluminium underneath. Temperature and pressure data was logged using Omega 36-gauge T-type insulated thermocouples and an Automation Direct Terminator Input-Output control module mated to LabView through an OPC (*Object-Embedded Linking for Process Control*) network.

The system was driven to steady-state and the equivalence of fluxes across interfaces allowed for the determination of the effective conductivity of the monolith, k_{eff}, through a (simple steady-state experiment) where T-type thermocouples are placed on the hot and cold sides of a foam/4130-steel sandwich at steady-state (linear temperature profile and equivalent flux at the boundary, with known conductive coefficient of copper). At steady state, the system must obey the equivalent flux relationship of Equation (4.1) where k_{4130} is the known thermal conductivity constant of the steel, k_{eff} is the unknown thermal conductivity constant of the metal foam, A is the interfacial area between the steel and foam and ΔT is the temperature difference measured across the distance ΔH in each thermal sub-domain.

$$-k_{4130}A\frac{\Delta T_{4130}^{hot}}{\Delta H_{4130}^{hot}} = -k_{eff}A\frac{\Delta T_{foam}}{\Delta H_{foam}} = -k_{4130}A\frac{\Delta T_{4130}^{cold}}{\Delta H_{4130}^{cold}} \tag{4.1}$$

4.5 Determination of Convective Heat Transfer Coefficient

The experimental apparatus for determination of convective heat transfer coefficient is shown in Figure 26. The coated and uncoated metal foams were placed into a smooth insulated polystyrene channel with variable flow rates of air passed lengthwise through the monolith, which was heated diffusively from below with a rubberized foil strip heater. The power dissipation of the heater (and subsequent heat flux) was determined by monitoring the average voltage and current supplied at steady-state. Thermocouples were placed to determine the air temperature along the top surface of the foam (Figure 26). Thermocouples were glued to the entrance and to the exit of the monolith to monitor the temperature of the monolith at the inlet and outlet of the heat-flux wall. A Thermovision FLIR camera was used to monitor the temperature and thermal gradient at the entry face of the monolith (Figure 27). The exit monolith temperature (and gradient) was measured by reversing the flow of air through the monolith and recording the steady-state. The convection coefficient air flow into the monolith was "pulled" by supplying negative fan pressure from the downstream side of the monolith-cooling assembly.

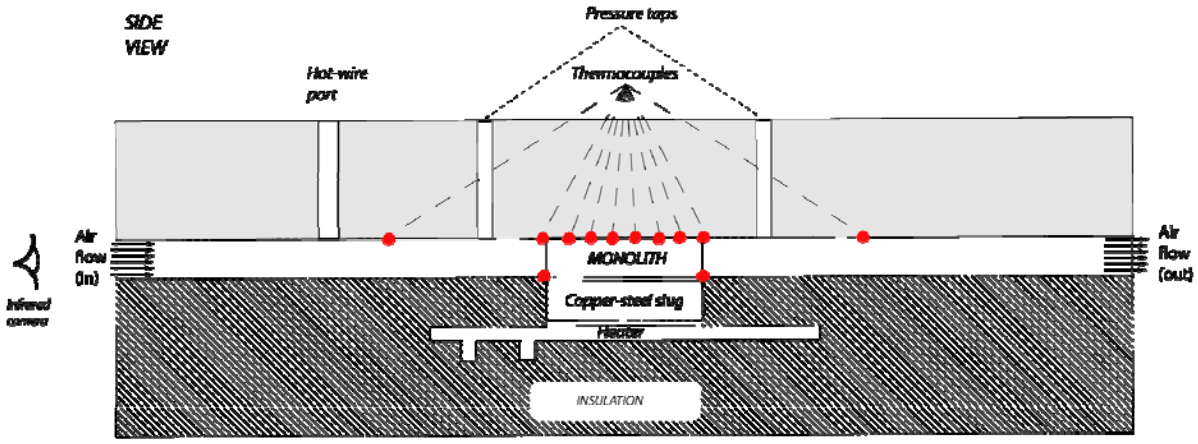

Figure 26: Forced air convection system used to determine volumetric convection coefficient of monolith samples (front view and side view section).

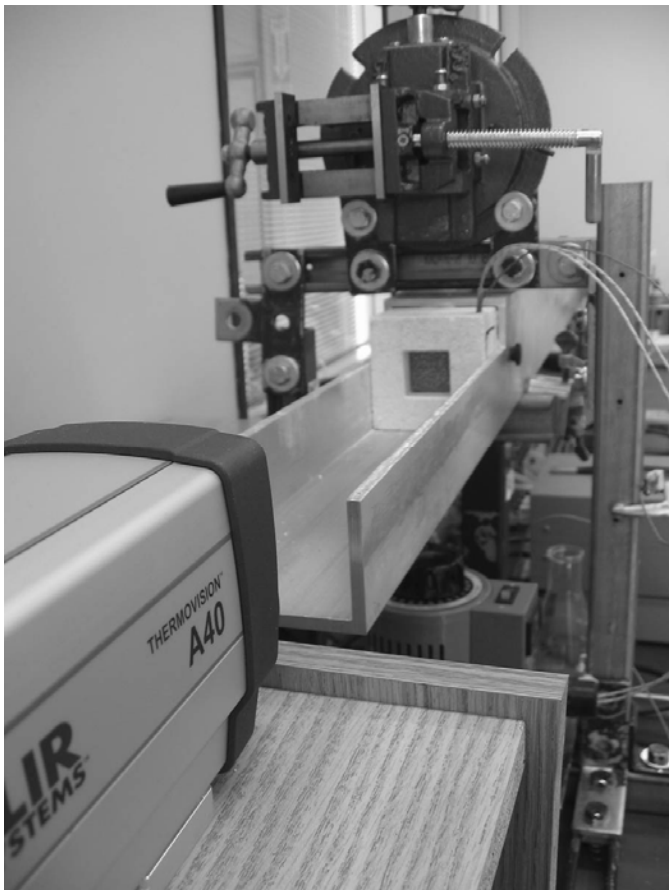

Figure 27: Photograph of the partially disassembled experimental heat exchange apparatus used in this work, with a view of the FLIR system, the clamping mechanism, a prototype insulation block and heating controls.

A steel and copper plate dampened small fluctuations in heat flow from the strip heater to the monolith and thermal contact was maintained by clamping the insulation in place above and below the sample and using Wakefield 120 thermal grease in the joints between the heater, steel strip, copper plate and metal foam. In several of the monolith samples, the void-fraction bottom face of the foam was layered with a thin shell of insulating refractory cement in order to prevent direct heating from the copper contacting plate and the coolant fluid (Figure 28). The bottom of this refractory shell was sanded down to ensure that the solid portion of the metal foam face was in direct thermal contact with the heating surface[2]. All heat removed from the system entered the foam via solid diffusion and left the system via convective transfer with the coolant.

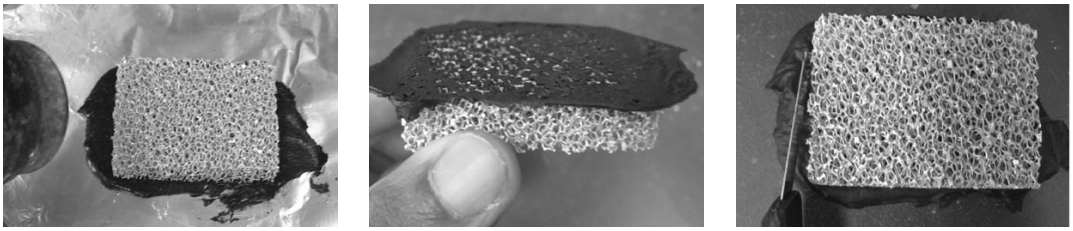

Figure 28: A thin layer of refractory cement is applied to the bottom face of the monolith (excess is trimmed and sanded down in last step). This thermally isolates the strip heater from the internal convective surfaces of the metal foam monolith.

A forward looking infrared (FLIR) camera was used to capture thermal data on the entry and exit sides of the monolith, while the heater's wall-boundary conditions were estimated from thermocouples cemented to the base of the monolith on the entrance and exit sides. Pressure taps were included to measure the pressure drop across the foam with a Dwyer Mark II Model 25 manometer. A probe port for a hot-wire anemometer allowed for direct measurement of the Darcian velocity of the mixed fluid stream in order to verify model-predicted fluid velocities.

[2] This method was found to have a negligible effect on overall heat transfer, due to the very small relative surface area of wall-to-fluid contact compared to the total surface area of the metal foam available for convective heat transfer.

The volumetric convection constant was determined by fitting the measured temperature profile of the coolant fluid with that predicted by the mathematical model for the system (see Section 5.3.1 on Page 69).

Chapter 5: Experimental Results and Analysis

In Chapter 5, the experimental results of procedures outlined in Chapter 4 are reported and discussed. Results for required experimental parameters for fluid transport and solid-phase diffusive transport are recovered and then used in the model system of Section 3.3 to derive values of the convective transport parameter, h_{vol}*, for metal foams with and without catalyst support coating, for metal foams of varied internal morphology and for metal foam systems with and without an insulating boundary between the boundary heating surface and the coolant fluid (Figure 28). Analytical attention is focused on comparison of results developed in this work vs. results recovered using previously published methods. Experimental sensitivity to experimental conditions and to modelling assumptions is considered.*

5.1 Momentum Transfer Coefficients

To determine the metal foam permeability, as discussed in Section 4.3, the pressure drop across the foam for a range of air flow velocities was measured (all foam samples used were cut to an identical width, length and height and oriented as illustrated in Figure 18). The measured data is presented in Figure 29. A non-linear dependency of pressure drop on air velocity can be noted, suggesting that the linear version of Darcy's law is not sufficient to describe the flow behaviour. Accordingly, the Darcy Forchheimer relationship (2.1) was fit to the data by plotting the ratio of the observed pressure drop over the length of foam tested as a function of the measured average velocity of the air passing through at the entrance, where the slope of the linear portion of the relationship is equal to μ/K. With K deduced, the value of C_F is deduced by examining the slope of the plot of $\Delta P/L \cdot V_f$ against V_f. The recovered K and C_F parameters are reported in Table 3 on Page 65. The permeabilities are comparable to those reported by previous investigations [47, 49, 50, 53]. It should be noted that the Forchheimer coefficients determined in this work, conducted at relatively low Reynolds numbers, are slightly higher than those determined elsewhere under conditions of high fluid flow rates [47].

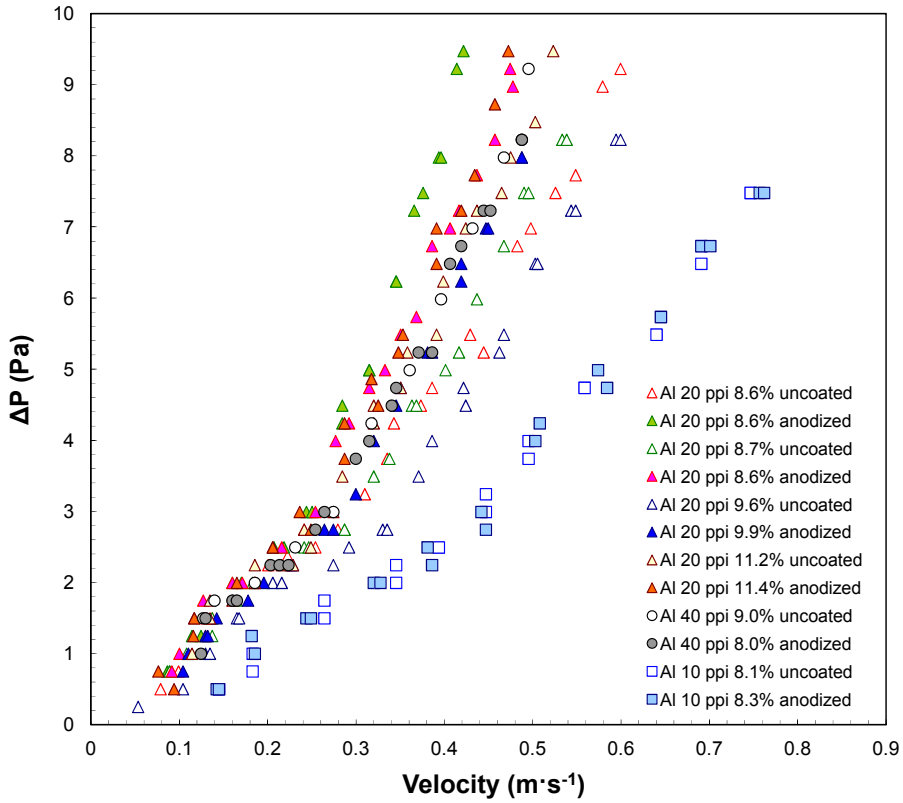

Figure 29: Experimental data for pressure drop of air through metal foam samples with specified relative densities and coating treatments (uncoated or anodized). The pressure gradient is most affected by the pores-per-inch morphology of the foams with lower pressure drops corresponding to lower ppi. Lower relative densities also correspond to lower pressure drops.

Figure 30 and Figure 32 show that permeability, K, shows a stronger variability with respect to average pore-size (measured as the number of pores per inch) than to the relative density, or porosity, ε, of the foam material. It is also clear that anodization of the foams reduces the permeability of the foams (Figure 31). This anodization effect may be due to slight constriction of the pore channels due to the coating of internal surfaces and to micro-roughening of the anodized surfaces on the foam, which would tend to increase the Fanning friction factor for fluid passing over the foam ligaments, which would tend to raise the value of C_F. The friction effect may manifest as micro-scale thickening of the fluid boundary layer, which will tend to reduce the mass flow rate of coolant passing over the boundary layer of the internal foam surfaces at a given pressure differential.

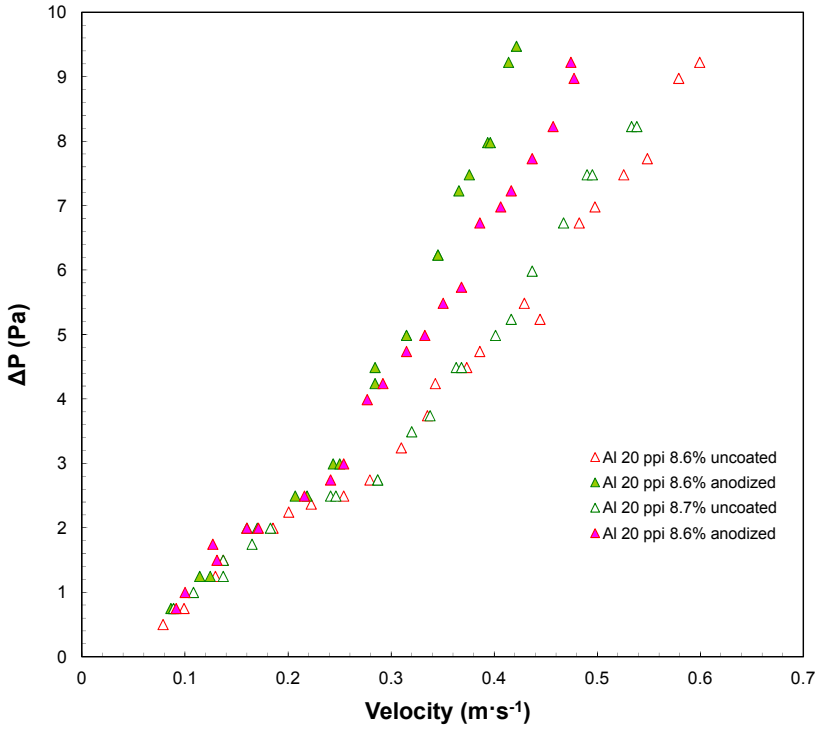

Figure 30: Experimental data for pressure drop of air through metal foam samples of similar relative densities and average pore sizes (uncoated and anodized). Within the same relative density range and pore size, only the channel friction parameter, C_F is significantly affected by the presence of an anodized catalyst support layer while values of permeability, K, are similar between uncoated and anodized samples.

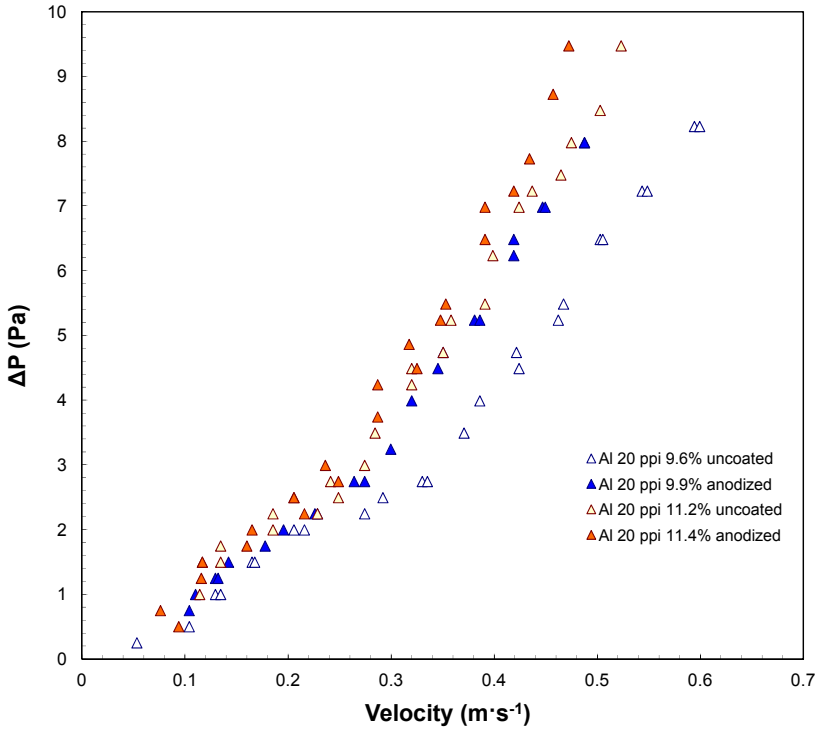

Figure 31: Experimental data for pressure drop of air through metal foam samples with varied relative densities and similar average pore sizes. The permeability, K, tends to decrease with increased relative density and with the addition of an anodized catalyst support layer.

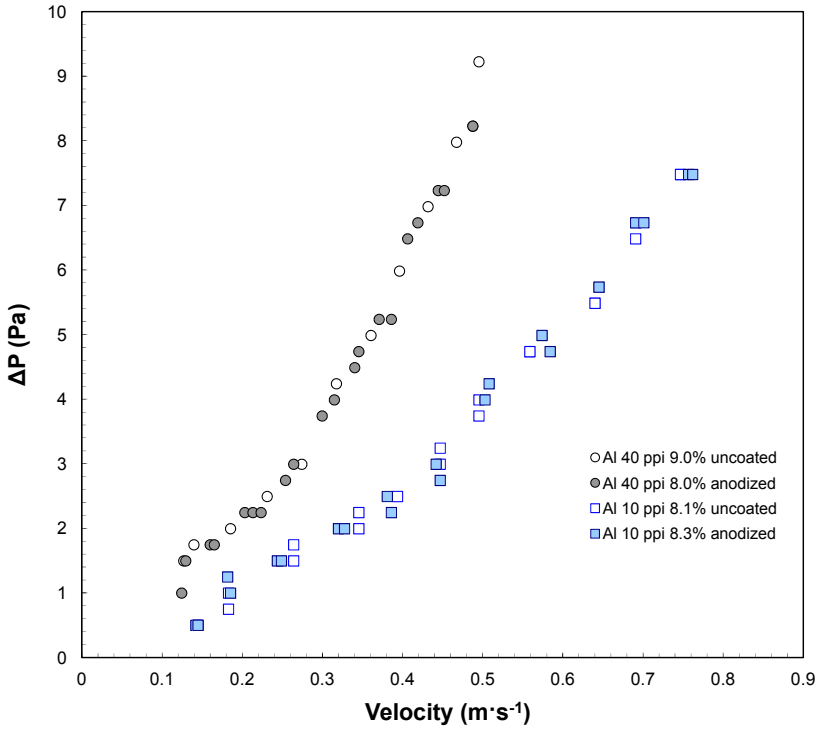

Figure 32: Experimental data for pressure drop of air through metal foam samples with similar relative densities and varied average pore sizes. The permeability, K, and the channel friction factor, C_F, are much more sensitive to variation in average pore size than the presence of an anodized catalyst support layer.

Table 3: Sample experimental results for forced-air convection through metal foam monoliths

ppi	Coating	Rel. density	K × 10^8 (m^2)	C_F
10	uncoated	8.1	9.1 ± 0.5	52 ± 6
10	anodized	8.3	8.7 ± 0.8	46 ± 10
20	uncoated	8.7	3.8 ± 0.2	62 ± 11
20	anodized	8.6	3.6 ± 0.2	136 ± 17
20	uncoated	9.6	4.3 ± 0.2	50 ± 10
20	anodized	9.9	3.3 ± 0.2	67 ± 10
20	uncoated	11.2	3.4 ± 0.2	88 ± 14
20	anodized	11.4	2.7 ± 0.2	73 ± 18
40	uncoated	8.0	3.3 ± 0.2	91 ± 13
40	anodized	9.0	3.0 ± 0.2	69 ± 10

5.2 Effective Thermal Conductivity Coefficient

The thermal conductivity for aluminium foams was measured using the apparatus described in Section 4.4. The experimental apparatus is reproduced in Figure 33 where the diagram is annotated with the experimental solid-state temperature data collected and the thermal gradients under observation.

The experiment depended on establishing a steady sate flux that can be inferred via Equation (4.1). Because of the minor perturbations of the steady-state due to dynamic changes in heating and coolant water at the 1-10 min. time scale, a large data sample was taken such that the 10-100 min. time scale averaged steady-state values of $\Delta T_{4130}^{hot} = \Delta T1 + \Delta T2$, ΔT_{foam} and $\Delta T_{4130}^{cold} = \Delta T4 + \Delta T5$ could be recovered as shown in (raw experimental data for a sample 10 ppi foam with $\varepsilon = 0.919$ shown in Figure 34). Internal flux equivalencies through hot-side and cold-side domains provided experimental validation that steady-state fluxes had, in fact, been achieved, for example: $-k_{4130}^{hot}\Delta T1 \cdot \left(0.5\Delta H_{4130}^{hot}\right)^{-1} = -k_{4130}\Delta T2 \cdot \left(0.5H_{4130}^{hot}\right)^{-1}$, where H_{4130}^{hot} represents the height of the 4130 steel control on the hot side of the foam under test.

The results of all experiments for the aluminium metal foams are presented in Figure 35. For comparison's sake, data reported by other researchers has also been plotted. As well, effective thermal conductivity calculated by the following simple linear correlation proposed by ERG [42] is also shown in Figure 35:

$$k_{mono} = \left(k_{solid}\right)\left(\frac{\rho_{mono}}{\rho_{solid}}\right)(0.33) \tag{5.1}$$

According to the empirical relationship of Equation (5.1), the conductivity is predicted to be a function of the relative volumetric mass density, the intrinsic conductivity of the solid (non-porous) metal from which the foam is derived, and a constant tortuosity factor that corrects for the extended path heat energy must take in flowing through the monolith in Equation (4.1).

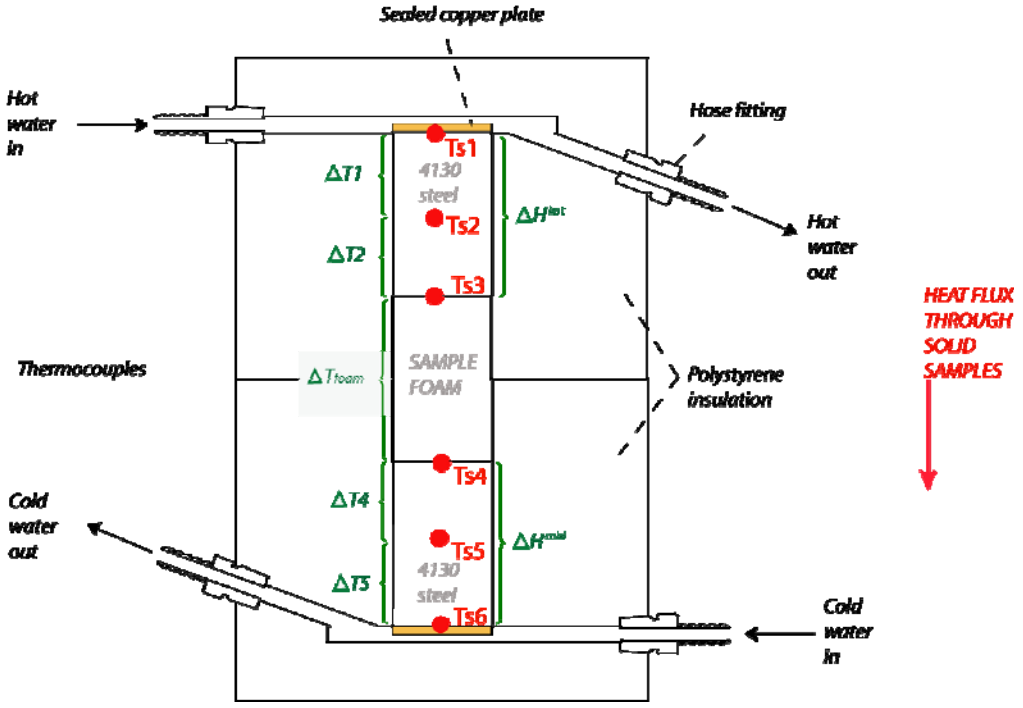

Figure 33: Specific solid-phase temperature data (Ts_i and thermal differences observed over the course of a thermal conductivity experiment with metal foam samples).

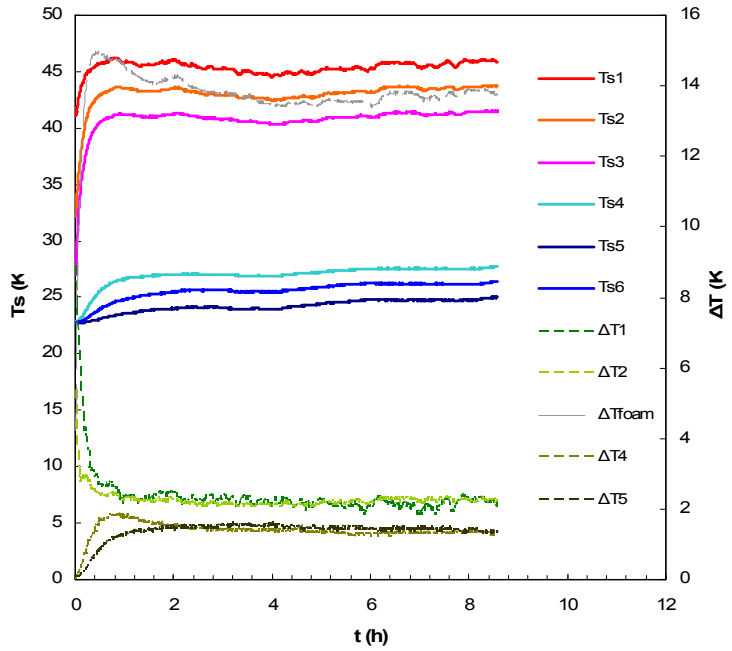

Figure 34: Temperature data for the steady-state conductivity experiment (10 ppi uncoated Al foam with 0.08 relative density).

From Figure 35, it can be noted that the effective thermal conductivities measured in this study compare well with values reported by others. Further, the values calculated from the correlation describe the measured effective conductivity adequately. The thermal conductivities of metal foams are strongly correlated to the relative density of the foam relative to the solid metal material from which they are made. In steady-state thermal diffusion (conduction), the size of the pores does not have a strongly correlated effect on the conductivity of the material. It is reasonable to assume, therefore, that adding a thin, low-conductivity coating to a metal foam will have a very small effect on the thermal conductivity. As such, for models of convective heat transfer in the metal foams, the coated metal foams under forced convection were assumed to have the same effective solid-phase conductivity as the uncoated foam of the same relative density as the coated monolith. The ERG correlation was applied to compute the effective conductivity.

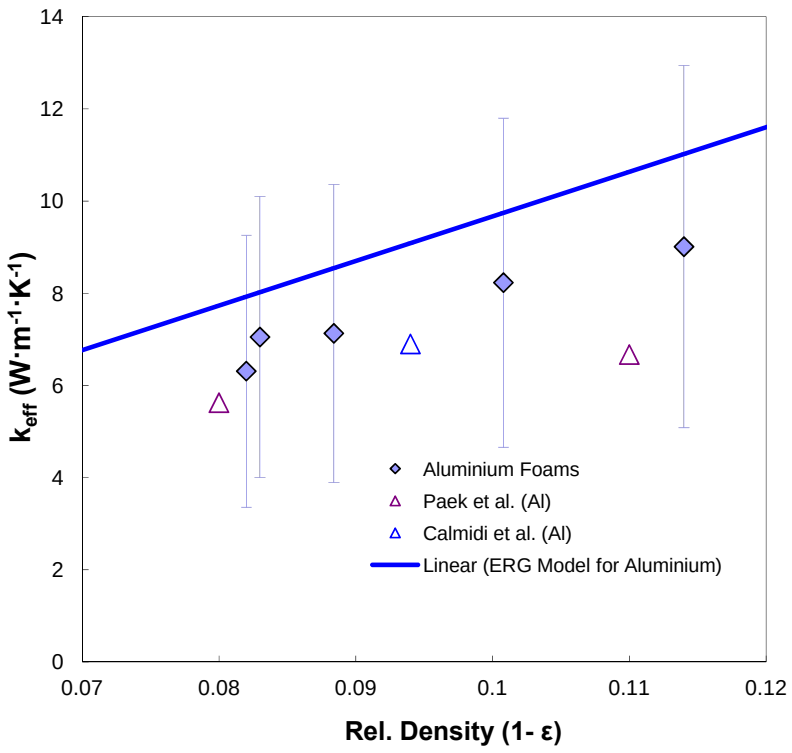

Figure 35: Experimental, modelled and literature values for the effective conductivity of a variety of metal foam samples. Effective conductivities are a strong function of the relative density (porosity) of the foam material. The conductivities are not correlated strongly to the number of pores per inch.

5.3 Convective Heat Transfer Coefficient

5.3.1 Methodology for Heat Transfer Coefficient Determination

The volumetric convection constant was determined by fitting the measured temperature profile of the coolant fluid with that predicted by the mathematical model for the system described in Chapter 3. The apparatus of Figure 26 was run to a steady-state using a known mass flow of air measured by hot-wire anomometer. The temperatures and pressures measured experimentally included point measurements indicated in Figure 36, accounting for observations made of thermocouple measurements of fluid temperatures (Tf_i), thermocouple measurements of solid-phase temperatures (Ts_i), and infrared camera monitoring of solid phase temperatures (IR_i). The infrared temperature measurements were made using a FLIR Thermovision camera that had been single-point calibrated to the emissivity of an aluminium blank covered with a single layer of black electrical tape (IR transparent and interfering-wavelengths opaque). The inlet solid phase temperature was measured as three data points from the FLIR camera with the point at $y=0$, $x=0$ re-calibrated against an in-situ thermocouple measurement for each experimental run. The three data points were fitted to a second order polynomial as a close-approximation of the thermal gradient boundary condition B.C. 1 of Section 3.3.7. The thermal data from a sample FLIR image is shown in Figure 37. Note that the "exit" solid phase temperature profile was generated experimentally by reversing the flow of air through the heated monolith and observing the steady-state temperature.

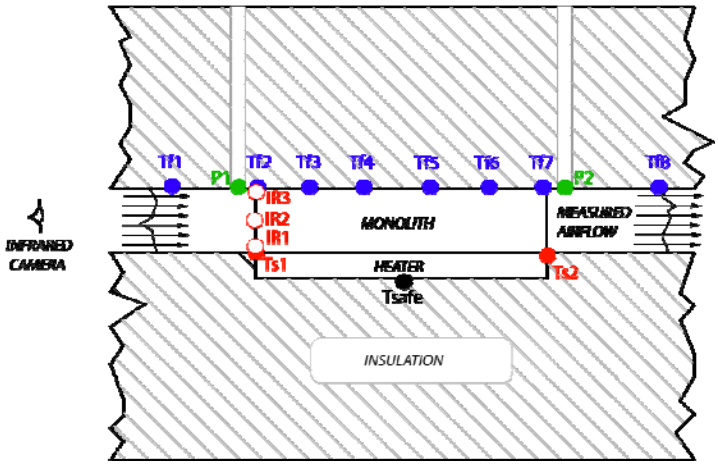

Figure 36: Specific fluid temperature (Tf_i), solid-phase (Ts_i and IR_i) and pressure data (P_i) taken over course of each convective-transport experiment.

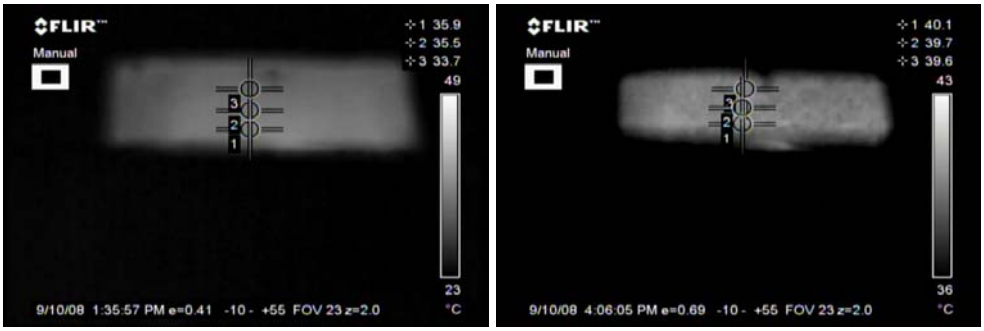

Figure 37: FLIR image solid phase temperature data, IR1, IR2 and IR3 (left=inlet, right=outlet) for the 10 ppi uncoated aluminium metal foam (8.1% relative density) with coolant channel flow at Reynolds number of 400.

The experimental values for IR_i, Ts_i, Tf_{in}, $P1$ and $P2$ were used to generate boundary conditions for the three-PDE model system at each experimental condition (see model parameters listed in Table 1) for values of h_{vol} scanned from 500 to 25,000 $W \cdot m^{-3} \cdot K^{-1}$ in steps of 500 $W \cdot m^{-3} \cdot K^{-1}$. For each stepwise value of h_{vol} used to solve the PDE system, the sum of squared errors was calculated between experimental fluid temperatures, T_{f_i}, and model predictions, $T_{f_i}^{'}$, at eight points along the upper boundary of the monolith $y=H$ and along its length $x=0$ to $x=L$. Up to one experimental temperature value, T_{f_i}, per experiment was rejected

if the error value, $e_i = \left| T_{f_i} - T_{f_i}^{'} \right|$ led to a Q-ratio value above the 90% certainty level according to Equation (5.2) based on the Dixon Q-ratio test devised in 1951 [83], [84]. If an experimental data point was discarded, the scan of h_{vol} was performed again and the h_{vol} leading to the minimum sum of squared errors was stored as the resulting value for the experiment.

$$Q_i = \frac{\left| e_i - e_{i-1} \right|}{range(e)} \tag{5.2}$$

The Dixon Q-ratio test employed has been shown to potentially cause experimentalists to reject important data, and the ratio values for given confidence ratios have subsequently been shown to be inaccurate [85]. Of particular concern is the (potential) loss of data (discarded as outlier points) that contain information about inflections in phenomenological trends. For this reason, the impact of using a Q-ratio test needs to be assessed. Figure 38 shows that the effect of Q-ratio rejection of outlier data is very small and has not significantly changed the recovered estimates of h_{vol}.

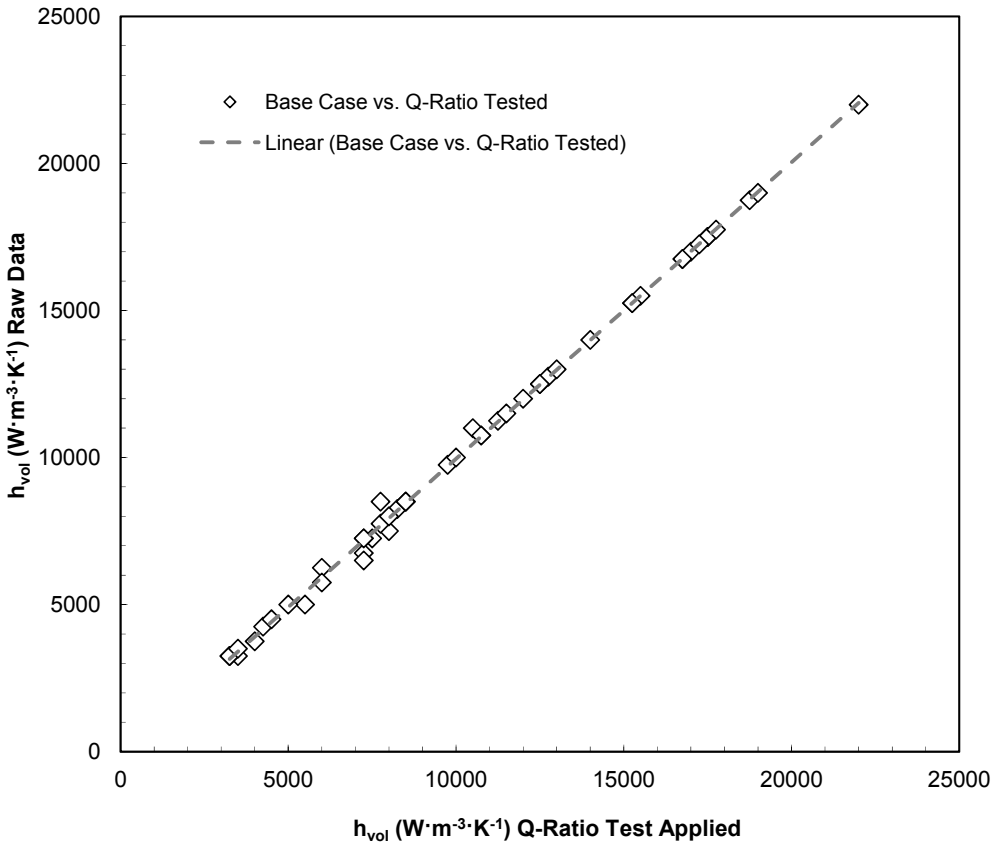

Figure 38: The effect of implementing Q-ratio tests on experimentally determined values of h_{vol} vs. values of h_{vol} recovered from non-filtered data.

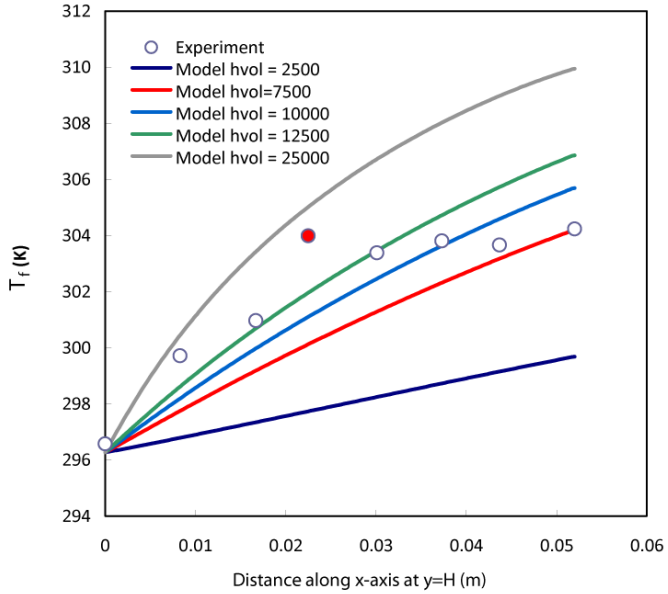

Figure 39: Experimental vs. model predictions for air temperature along the top midline of a 10 ppi uncoated aluminium metal foam (8.1% relative density) with coolant channel Reynolds number of 400. One outlier data point is indicated in red.

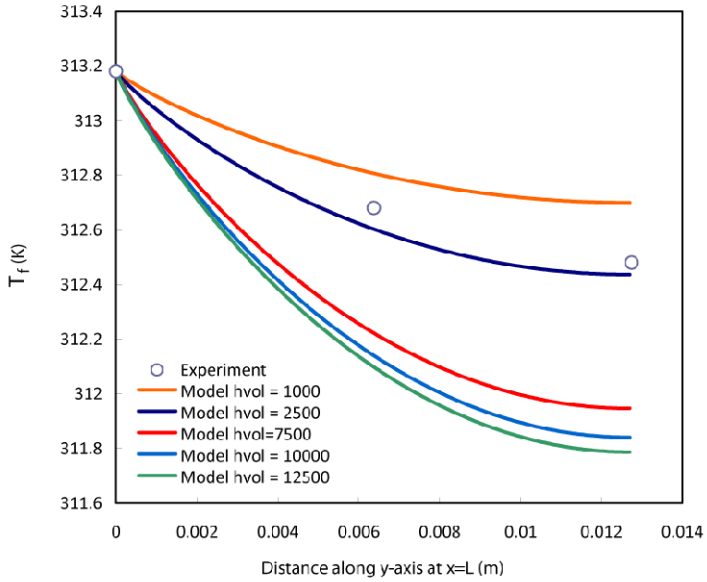

Figure 40: Experimental vs. model predictions for solid-phase temperature along exit face of 10 ppi aluminium metal foam (8.1% relative density) with coolant Reynolds number of 400.

5.3.2 Effect of Anodization on Convective Heat Transfer Coefficient

The experimental protocol of Section 4.5 and analysis method of 5.3.1 was employed to determine the effect of anodization on the volumetric heat transfer coefficient of an open-cell metal foam. Experimentally determined convective heating coefficients, h_{vol}, for uncoated and anodized (Type III) aluminium foams under coolant flows between Re_c between 100 and 1,700 are reported in Figure 41. The effect of coating the foam with a 76-micron thick layer of aluminium oxide is to decrease the effective convective transfer at a given rate of flow (i.e., higher convective transfer for higher flow regimes).

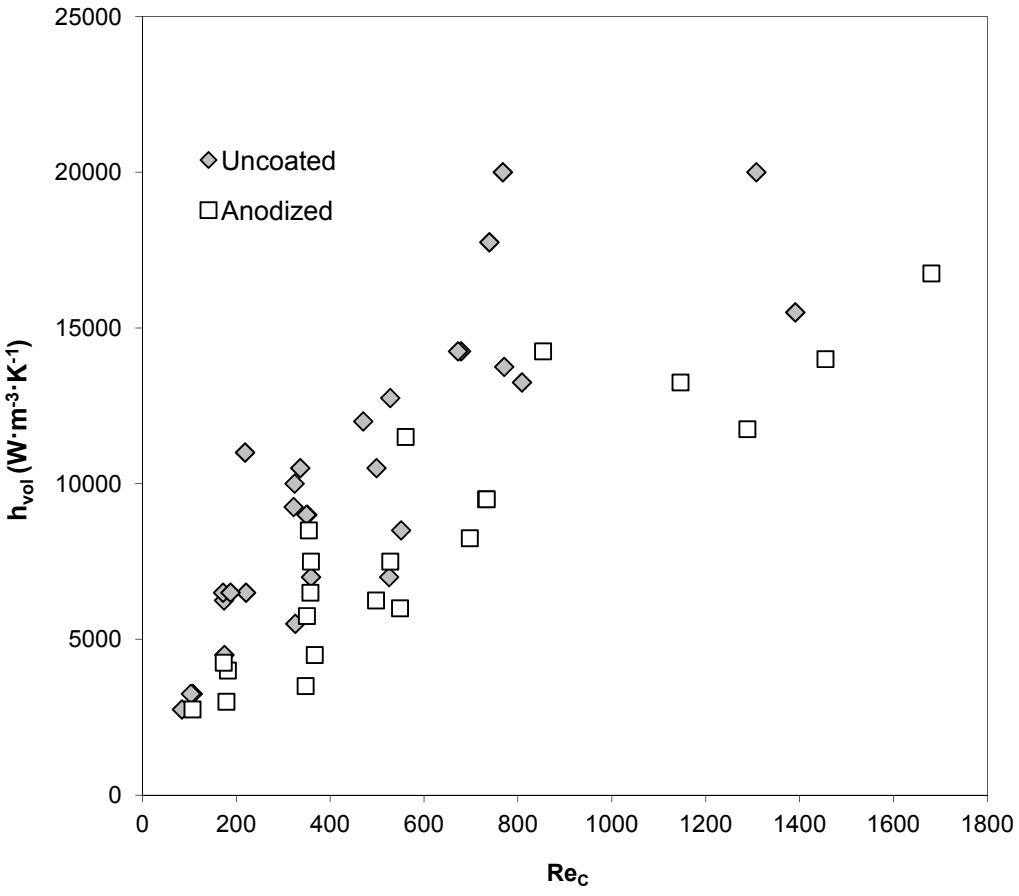

Figure 41: Convective volumetric heat transfer coefficient as a function of channel Reynolds number for anodized and uncoated metal foams (48 experimental runs). The model was fit to minimize the sum of the squared errors between measured and predicted coolant temperatures.

A correlation analysis (*Table 4*) of more than 50 model-fitted values for h_{vol} shows that the presence of an anodized layer is related to the volumetric convection coefficient, but not as strongly as the rate of fluid flow (at either the channel or the pore scale) or as strongly correlated as the morphology (pores per inch) of the foam itself (which should have an impact on the efficiency of fluid mixing in the entrance of the foam).

Table 4: Correlations: foam parameters and convective heat exchange metrics

	hvol	ppi	Density	Anodized	ReC	ReP
hvol	1.0000	-0.3676	-0.0937	-0.2090	0.7738	0.7100
ppi	-0.3676	1.0000	0.0363	0.0180	-0.3539	-0.5827
Density	-0.0937	0.0363	1.0000	0.1079	-0.1798	-0.3850
Anodized	-0.2090	0.0180	0.1079	1.0000	0.1940	0.1499
ReC	0.7738	-0.3539	-0.1798	0.1940	1.0000	0.9138
ReP	0.7100	-0.5827	-0.3850	0.1499	0.9138	1.0000

While anodization may increase the surface roughness (and hence the available surface area) for heat transfer, the low-conductivity Al_2O_3 surface may have poor micro-diffusion heat transfer within the coolant boundary layer. The thermal conductivity of Al_2O_3 is an order of magnitude lower than that of aluminium metal. At a thickness of 76 microns, the low-conductivity catalyst support adds nearly 20% to the radius of an individual metal foam ligament with a diameter of 800 microns. This thick layer may pose some diffusion limitations to effective heat transfer between the fluid stream and the underlying metal, although such an effect should (at the pore-scale) be limited to the non-steady-state case. It is very likely that the net effect of enhanced surface roughness and decreased flow permeability impact the local mixing quality of the foam leading to the decreased h_{vol} observed in anodized foam samples. Results for other coated and uncoated aluminium foams in the work are presented in Table 5 on Page 84.

There is no strong correlation between foam bulk density (porosity) and the volumetric heat transfer coefficient, which may be a manifestation of low experimental sensitivity to these parameters, or interdependence of surface area with other effects, such as effective conductivity and fluid mixing within the foam. Because the porosity is strongly correlated to the specific

surface area density of the foams this suggests that fluid-flow effects of the foams (i.e., mixing) may have a greater impact on heat transfer than available surface area within the low-flow regimes tested in this work.

The impact of anodization, taking pore-size, thermal conductivity (of the foam) and flow conditions is shown in Figure 42, Figure 43 and Figure 44, where the pore-scale Nusselt number $\left(h_{vol} d_P \cdot k_{eff}^{-1}\right)$ is plotted against the pore-scale Reynolds number, Re_{P}, where d_P is the average pore size of 10, 20 and 40 ppi foams and k_{eff} is the effective thermal conductivity of the foam samples.

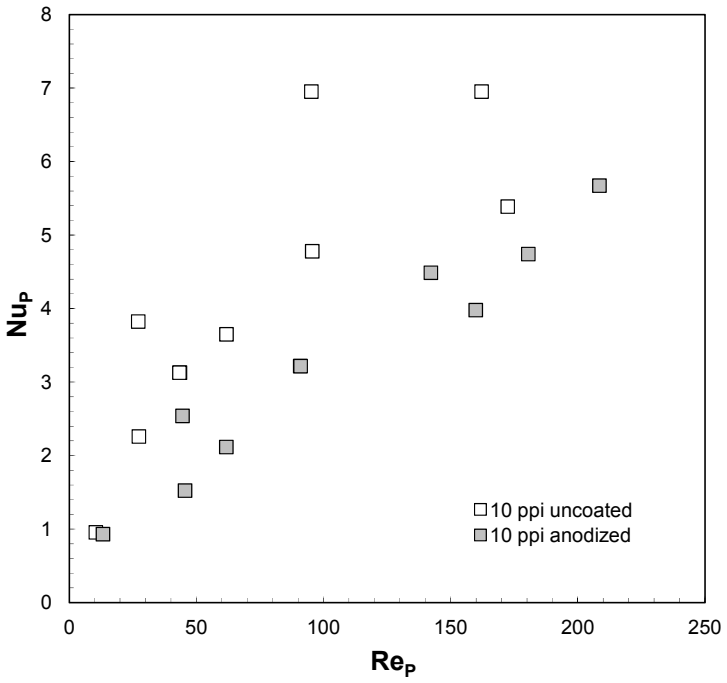

Figure 42: Impact of anodization on the pore-scale Nusselt number for 10 ppi foams.

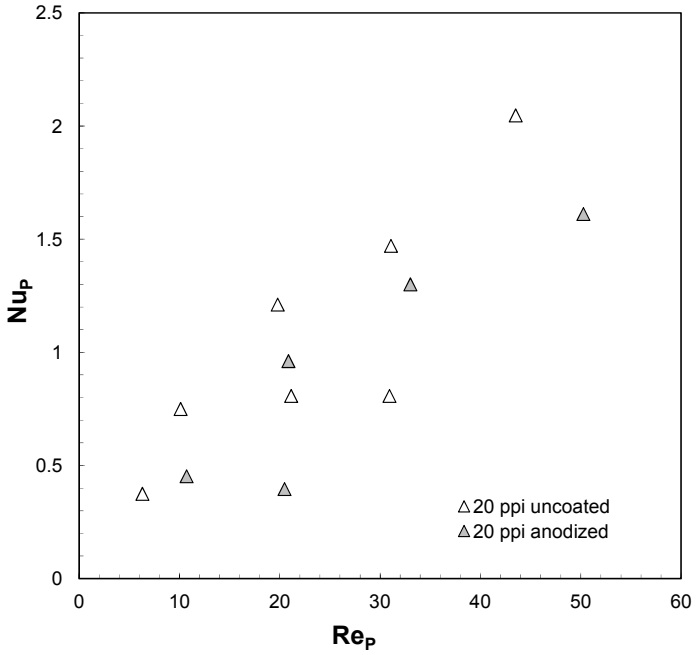

Figure 43: Impact of anodization on the pore-scale Nusselt number for 20 ppi foams.

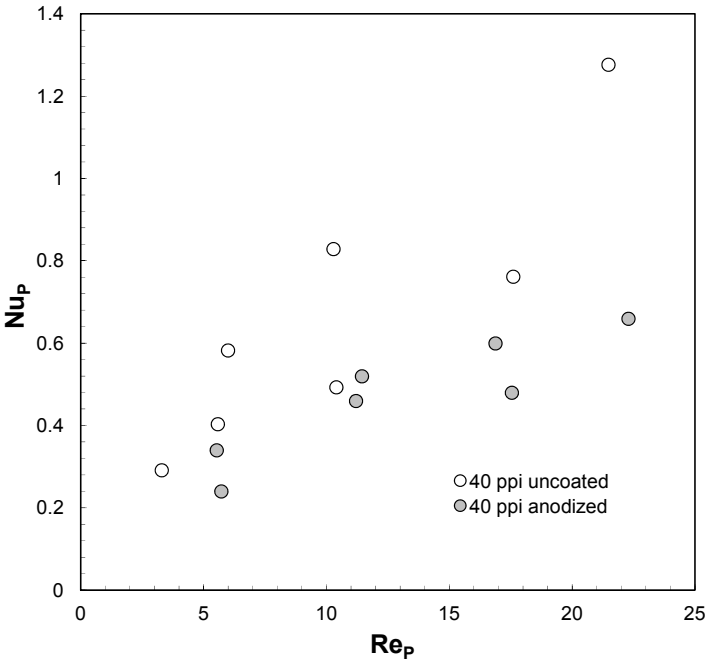

Figure 44: Impact of anodization on the pore-scale Nusselt number for 40 ppi foams.

5.3.3 Pore-Scale vs. Bulk Scale Flow Characterization

The effects of anodization can be related to pore-scale flow phenomena, by plotting fitted values of h_{vol} against the pore scale Reynolds number outlined in Equation (5.3), where ρ_f is the fluid density, U_f is the superficial bulk-fluid velocity, d_P is the mean diameter of internal pores (measurement provided by manufacturer), μ is the fluid viscosity and ε is the void-fraction (porosity) of the monolithic foam.

$$\mathrm{Re}_P = \frac{\rho_f U_f d_P}{\varepsilon \mu} \tag{5.3}$$

The proportionality of the relationship between h_{vol} and Reynolds number is preserved at the full-domain (channel) scale and at the pore scale as illustrated in Figure 45 and Figure 46.

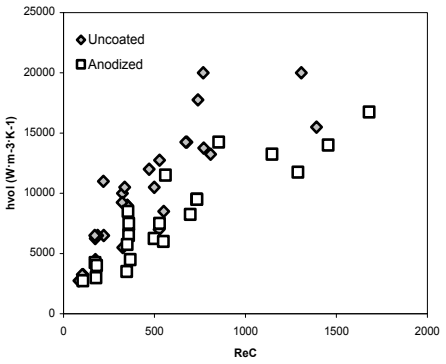

Figure 45: Volumetric convection coefficients for the uncoated and anodized foams related to the channel-scale Reynolds flow.

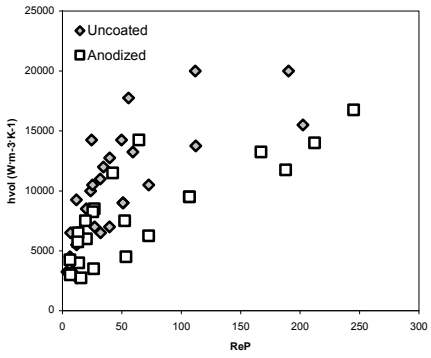

Figure 46: Volumetric convection coefficients for the uncoated and anodized foams related to the pore-scale Reynolds flow.

5.3.4 Utility of Dimensional Dependency in Data Analysis

Determination of h_{vol} allows for the calculation of convection efficiencies described in Section 2.5.5, even in cases where non-equivalent quantities of heat must be dissipated. The advantages of fitting h_{vol} for thermal observations throughout the monolith domain are apparent from examination of Figure 47, which shows h_{vol} values that are only fitted to minimize the error

between the experimental and the model-derived temperature of bulk air exiting the monolith – that is, for values of h_{vol} derived from an overall energy balance of the system. In this case, the energy balance requirement for overall convective transfer of heat is met, but agreement between the model system prediction for temperature gradients (inside the monolith domain and at the boundaries of the domain) and the experimentally determined distribution of fluid and solid temperatures (at the boundaries of the monolith domain) are ignored. In such a scheme, no useful information is obtained about the effect of anodizing the monolith with a catalyst support since Figure 48 demonstrates that even with identical flow conditions and total energy inputs, a change in the volumetric convection coefficient h_{vol} will disturb the distribution of fluid-phase and solid-phase temperatures within the domain. This h_{vol} information is required for design of coupled reaction and heat exchange schemes using porous monoliths since small variations in temperature may have large consequences for local reaction yields and selectivity. These local variations are not an important design consideration for nominally isothermal reactors, or "one-pot" autothermal reactors, but they will have a considerable impact on reactor schemes where heat transfer between regions of high exothermic reaction rates and high endothermic reaction rates is to be optimized.

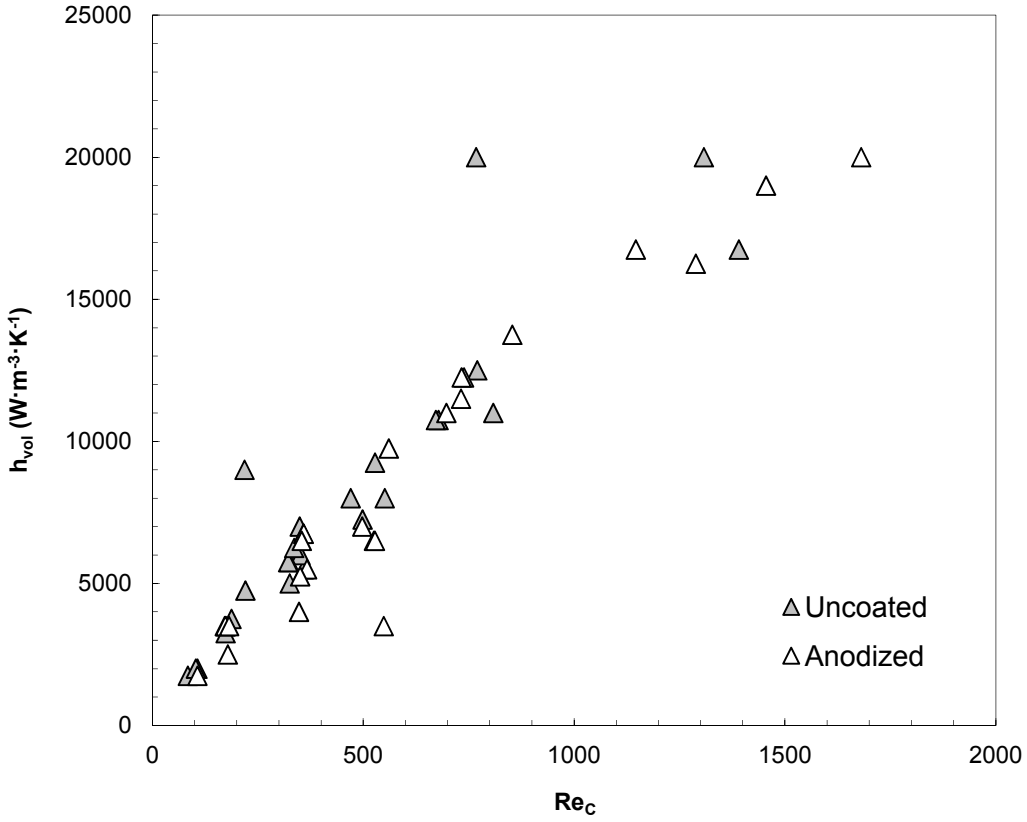

Figure 47: Estimates of convection coefficient h_{vol} to a spatially independent energy balance (fluid inlet temperature and outlet temperature with heating inputs) yields no distinction between the convection coefficient differences between coated vs. uncoated monoliths.

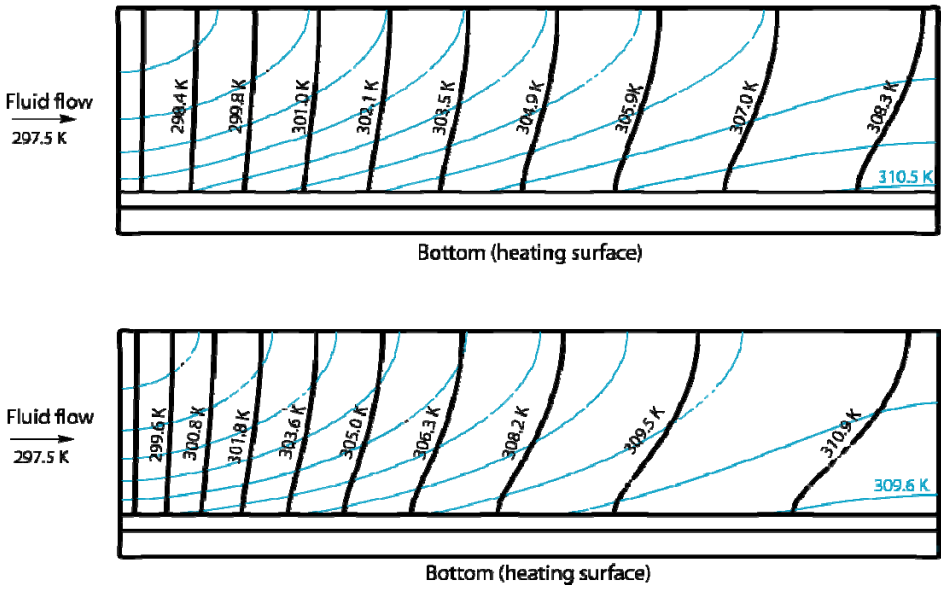

Figure 48: Model-generated isothermal lines (black) for the fluid at ReC=400 and the solid monolith (light grey) through an 8.1% density foam monolith with 2.85 W of resistive heating through the bottom with modelled volumetric convection coefficient of 10,000 $W{\cdot}m^{-3}{\cdot}K^{-1}$ (top) and for 20,000 $W{\cdot}m^{-3}{\cdot}K^{-1}$ (bottom).

5.3.5 Comparison of Methodologies for Determining Volumetric Convection Coefficient

The experimental steady-state results for uncoated foams are similar to previous work to determine the wall-convection coefficient, $\overline{h_w}$. Tian et al. [18] reported a wall-convection coefficient of 115 $W{\cdot}m^{-2}{\cdot}K^{-1}$ for 6 to 10 ppi Aluminium foams at a channel Reynolds number of 570, which is similar to the values cited in Table 5 for experiments performed under similar conditions. Results for an analogous average wall-convection coefficient, $\overline{h_w^{\bullet}}$, are included in Table 5 and are discussed below.

The volumetric convective coefficients are plotted as a function of the channel Reynolds number in Figure 49. The convection-parameter model fit values are presented along with two values for separate treatments of wall-bounded convective heat exchange coefficients $\overline{h_w^{\bullet}}$ and $\overline{h_w}$ $\left(W \cdot m^{-2} \cdot K^{-1}\right)$ extrapolated to volumetric wall-bounded coefficients $\overline{h_{vol}^{\bullet}}$ and $\overline{h_{vol}}$

($W \cdot m^{-3} \cdot K^{-1}$), by multiplying the surface area of the wall contact by the depth of the foam monolith sample.

The analogous wall-convection coefficient, $\overline{h_w^{\bullet}}$, reported alongside $\overline{h_w}$ in this work treats the average driving temperature, $\Delta T_{avg}^{\bullet}$, as the difference between the wall temperature (i.e., the surface along which the monolith is heated) and the average bulk fluid temperature, as averaged at the inlet of the foam and at the outlet [Equation (5.4)]. This slight modification from Equation (5.5) used in previous work allows for a more accurate estimate of wall convection coefficient at low Reynolds number regime that would occur in a heat coupled heterocatalytic reactor in which endothermic reaction kinetics have relatively long time scales. At lower Reynolds numbers, the temperature difference between the coolant and the monolith at the exit will be substantially lower than at the entrance, an effect which will tend to give higher wall convection values than would be otherwise estimated using Equation (5.5).

$$\overline{h_w^{\bullet}} = \frac{q}{A\Delta T_{avg}^{\bullet}}$$
$$\Delta T_{avg}^{\bullet} = \frac{\sum_{i=1}^{n} T_{w_i} - T_{f_{bulk_i}}}{n} \tag{5.4}$$

$$\overline{h_w} = \frac{q}{A\Delta T_{avg}}$$
$$\Delta T_{avg} = \frac{\sum_{i=1}^{n} T_{w_i}}{n} - T_{f_{in}} \tag{5.5}$$

It must be noted that the area, A, of convective transfer for the wall-convection analysis is taken as the nominal area of the heater contacting the monolith domain, whereas the actual area of convective transfer in this study varied from 10 to 35 times the nominal wall-surface contact area due to the large area-to-volume ratio of the foam monoliths' internal surfaces. The two

schemes for evaluating the wall-convection coefficients in (5.4) and (5.5) can be used to calculate average volumetric coefficients via Equations (5.6) and (5.7), where V is the bulk volume of the monolith.

$$\overline{h_{vol}^{\bullet}} = \frac{q}{V \Delta T_{avg}^{\bullet}} \tag{5.6}$$

$$\overline{h_{vol}} = \frac{q}{V \Delta T_{avg}} \tag{5.7}$$

In Figure 49, the calculated average volumetric convection coefficients $\overline{h_{vol}^{\bullet}}$ and $\overline{h_{vol}}$ for each foam [Equations (5.6) and (5.7)] are plotted against the model-fitted convection coefficients h_{vol} derived from the method of Section 4.5. The method of calculating a volumetric average convection coefficient, $\overline{h_{vol}}$, by considering the local wall-bounded driving convection force ΔT_{avg} as in previous work, tends to underestimate the volumetric coefficient, while the calculation of $\overline{h_{vol}^{\bullet}}$ using $\Delta T_{avg}^{\bullet}$, tends to more closely approximate the model-fitted result, h_{vol}.

Table 5: Comparison of convective heat transfer coefficient determined from different methodologies

ppi	Coating	ε	$\mathrm{Re_C}$ $\left(\frac{U_f \rho_f D_h}{\mu_f}\right)$	$\mathrm{Re_P}$ $\left(\frac{\rho_f U_f d_P}{\varepsilon \mu}\right)$	h_{vol} $\left(\frac{W}{m^3 \cdot K}\right)$	$\overline{h_w^{\bullet}}$ $\left(\frac{W}{m^2 \cdot K}\right)$	$\overline{h_w}$ $\left(\frac{W}{m^2 \cdot K}\right)$	$\xi_{\dot{Q}}$ $\times 10^{-3}$
10	uncoated	0.92	84	12	2750	68	45	4.2
10	anodized	0.92	107	16	2750	60	42	3.9
10	uncoated	0.92	219	32	11000	77	55	6.5
10	uncoated	0.92	221	32	6500	95	66	8.1
10	uncoated	0.92	349	51	9000	119	84	12
10	uncoated	0.92	351	51	9000	119	83	12
10	anodized	0.92	359	52	7500	105	74	9.9
10	anodized	0.92	367	53	4500	106	78	10
10	anodized	0.92	498	73	6250	113	85	12
10	uncoated	0.92	499	73	10500	135	96	15
10	anodized	0.92	732	107	9500	133	100	16
10	anodized	0.92	733	107	9500	141	105	16
10	uncoated	0.92	768	112	20000	142	105	18
10	uncoated	0.92	771	112	13750	148	113	18
10	anodized	0.92	1146	167	13250	151	117	20
10	anodized	0.92	1289	188	11750	148	119	20
10	uncoated	0.92	1308	190	20000	167	131	24
10	uncoated	0.92	1391	202	15500	183	147	26
10	anodized	0.92	1455	212	14000	150	118	21
10	anodized	0.92	1681	245	16750	167	131	24
20	uncoated	0.89	107	8	3250	74	52	1.0
20	uncoated	0.89	172	13	6500	85	59	1.4
20	uncoated	0.91	174	13	6250	87	61	2.2
20	anodized	0.89	182	14	4000	95	66	1.4
20	uncoated	0.91	324	24	10000	121	86	3.7
20	uncoated	0.89	336	25	10500	121	85	2.5
20	anodized	0.89	348	26	3500	137	105	2.6
20	anodized	0.89	354	27	8500	131	91	2.5
20	uncoated	0.89	359	27	7000	131	94	2.7
20	uncoated	0.91	470	34	12000	143	105	4.9

ppi	Coating	ε	$\mathrm{Re_C}$ $\left(\frac{U_f \rho_f D_h}{\mu_f}\right)$	$\mathrm{Re_P}$ $\left(\frac{\rho_f U_f d_P}{\varepsilon \mu}\right)$	h_{vol} $\left(\frac{W}{m^3 \cdot K}\right)$	$\overline{h_w^{\bullet}}$ $\left(\frac{W}{m^2 \cdot K}\right)$	$\overline{h_w}$ $\left(\frac{W}{m^2 \cdot K}\right)$	$\xi_{\dot{Q}} \times 10^{-3}$
20	uncoated	0.89	526	40	7000	152	116	3.6
20	uncoated	0.89	528	40	12750	154	110	3.6
20	anodized	0.89	561	42	11500	155	111	3.4
20	uncoated	0.91	679	50	14250	166	122	6.4
20	uncoated	0.89	739	56	17750	170	123	4.4
20	uncoated	0.91	809	59	13250	171	134	6.9
20	anodized	0.89	854	64	14250	174	128	4.3
40	uncoated	0.92	103	4	3250	67	47	0.86
40	anodized	0.91	173	6	4250	90	64	1.1
40	uncoated	0.92	175	6	4500	94	66	1.4
40	anodized	0.91	179	7	3000	88	64	1.1
40	uncoated	0.92	188	7	6500	94	65	1.5
40	uncoated	0.92	322	12	9250	127	90	2.4
40	uncoated	0.92	326	12	5500	126	91	2.4
40	anodized	0.91	350	13	5750	118	84	1.9
40	anodized	0.91	358	13	6500	113	83	1.8
40	anodized	0.91	528	19	7500	146	106	2.6
40	anodized	0.91	549	20	6000	138	102	2.5
40	uncoated	0.92	551	20	8500	140	104	3.1
40	uncoated	0.92	672	24	14250	177	130	4.1
40	anodized	0.91	697	26	8250	147	114	2.9

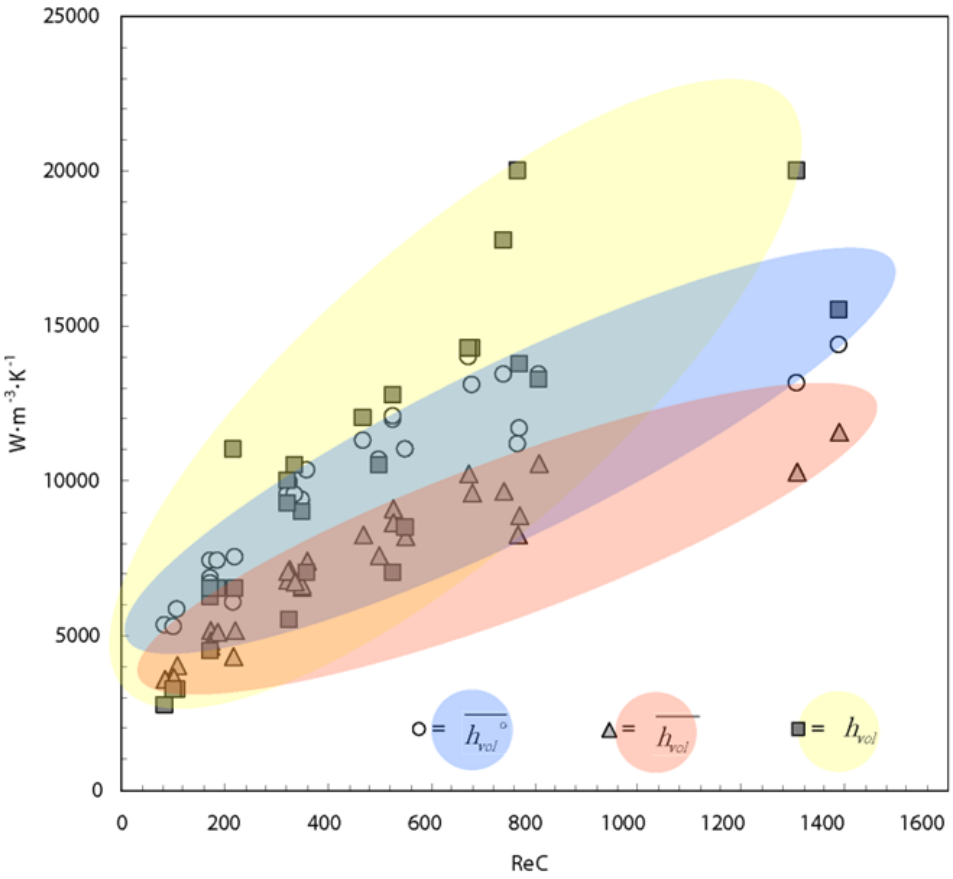

Figure 49: Estimated volumetric convection coefficient obtained via extrapolation of wall-convection data described in Equation (5.6) circled in blue, Equation (5.7) circled in red and via model fitting as described in Section 5.3.1 circled in yellow (colour regions applied manually as visual aides).

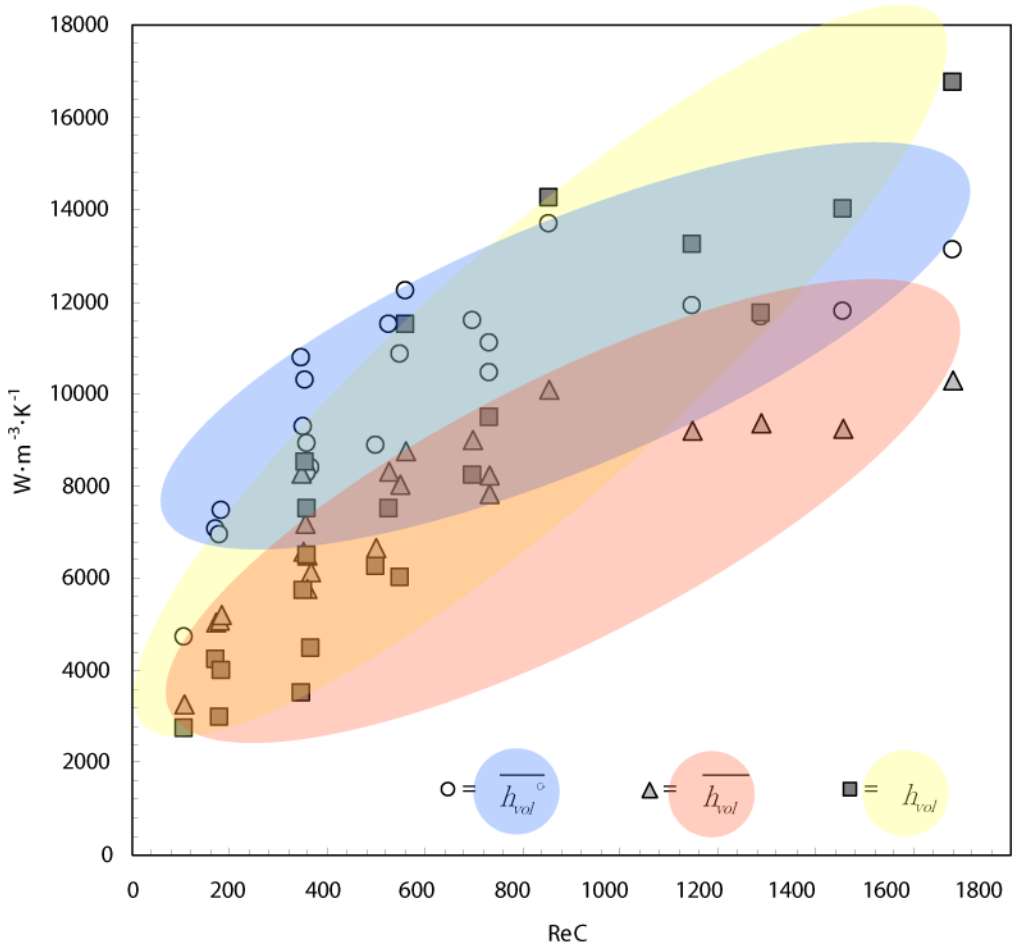

Figure 50: Estimated volumetric convection coefficient for anodized aluminium foams via extrapolation of wall-convection data described in Equation (5.6) circled in blue, Equation (5.7) circled in red and via model fitting as described in Section 5.3.1 circled in yellow (colour regions applied manually as visual aides).

The coefficient comparisons of Figure 49 and Figure 50 show the importance of accounting for the temperature of the solid and fluid phases throughout the entire monolith in order to account for convection driving force throughout the entire experimental domain (as opposed to using wall temperatures to determine the average driving force for convection). As evidenced by experimental observation (Figure 37 of Section 5.3.1), even the solid-phase temperature profile at the fluid entrance shows significant solid-phase thermal gradients such that the driving force for convection is not adequately described by the solid-phase temperature at the wall where the heater and monolith are in contact. The development of a steady-state method to calculate h_{vol}

rather than $\overline{h_{vol}^{\cdot}}$ or $\overline{h_{vol}}$ provides a scalable convection parameter that might be used to fit local convective coefficients to the local velocity within a domain under investigation. This information is the required parameter for complex reactor designs of non-isothermal coupled heat-momentum-mass transfer systems of practical interest (Chapter 6).

5.3.6 Comparisons of Experimental h_{vol} with Scalable Literature Values

The experimental values of h_{vol} for the uncoated 10 ppi metal foam (reported in Table 5) are comparable to those determined by Hwang using a non-steady-state method [57], which is reported as an experimentally validated correlation.

The heat-transfer literature for these materials does not consider the low bulk-flow regimes required for practical heterocatalytic mass-transfer designs that this work investigates, so the comparison is made via comparable pore scale Nusselt numbers at equivalent pore-scale Reynolds number regimes in Figure 51 as per Equation (5.3) and Equation (5.8) where d_P is the average pore diameter of the foam sample [86] andI k_{eff} is the solid-phase conductive heat transfer coefficient.

$$Nu_P = h_{vol} \cdot d_P \cdot k_{eff}^{-1} \tag{5.8}$$

At the bulk scale, the lowest-flow Hwang foam under test was a 10 ppi foam with $\varepsilon = 0.95$ under an $Re_C = 1900$ flow regime, which yielded a reported h_{vol} of 27,000 $W \cdot m^{-3} \cdot K^{-1}$. This compares with an experimental 10 ppi foam with $\varepsilon = 0.92$ under $Re_C = 1681$ with a recovered h_{vol} of 16,750 $W \cdot m^{-3} \cdot K^{-1}$. Other results in the literature (using different materials such as ceramics) are taken from substantially higher Reynolds flows. The large body of literature results for wall-convection extrapolated values of $\overline{h_{vol}}$ are not scalable and are not suitable for comparison with this work (see Section 5.5.2).

This work is the first (to the author's knowledge) to consider the convective transport effects of the catalyst support layer (the anodized layer) on the values of h_{vol}. It is notable that in comparison to the Hwang results for equivalent uncoated foams that pore-scale Nusselt numbers are substantially reduced at equivalent Reynolds flows, consistent with findings reported in [57].

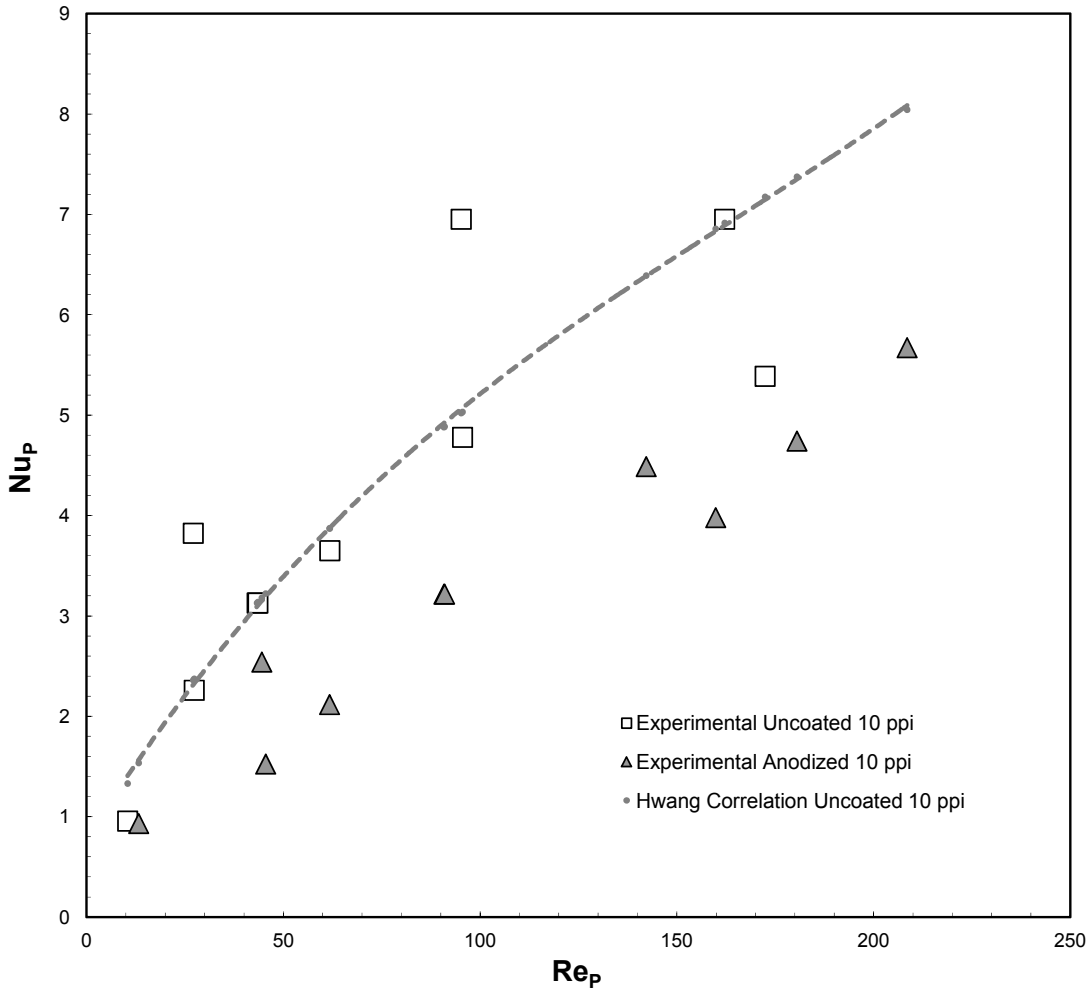

Figure 51: Comparison of experimental heat transfer values for 10 ppi foam of $\varepsilon = 0.917$ against Hwang's pore-scale heat transfer correlation for 10 ppi foam of $\varepsilon = 0.95$ (correlation experimentally validated between $Re_P = 70$ and $Re_P = 300$).

5.3.7 Useful h_{vol} Correlations for Reactor Design

The experimental values of h_{vol} for the anodized 10 ppi, 20 ppi and 40 ppi metal foams are reported in Figure 52, Figure 53 and Figure 54 with simple correlations to the pore Reynolds number (in air). This empirical data is useful, because it can be used to model local convective heat transfer within a non-isothermal, non-isobaric system with known (local) coolant flow rates.

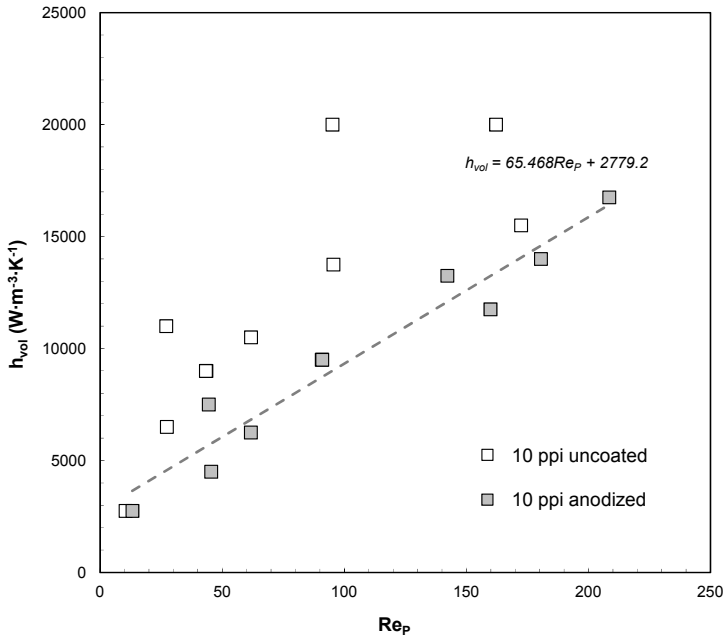

Figure 52: A correlation of experimental heat transfer values for anodized 10 ppi foam of $\varepsilon = 0.917$ at flow rates of $Re_P = 1$ to 205.

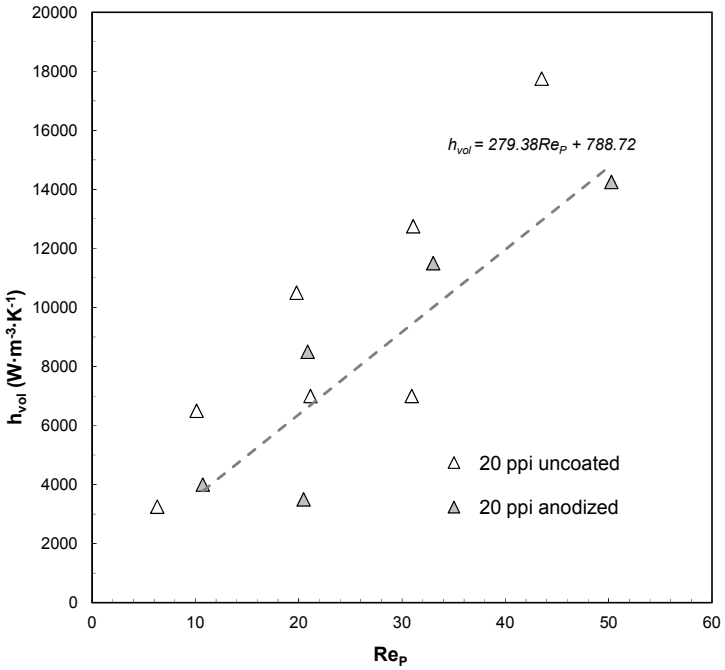

Figure 53: A correlation of experimental heat transfer values for anodized 20 ppi foam of $\varepsilon = 0.890$ to 0.910 at flow rates of $Re_P = 10$ to 50.

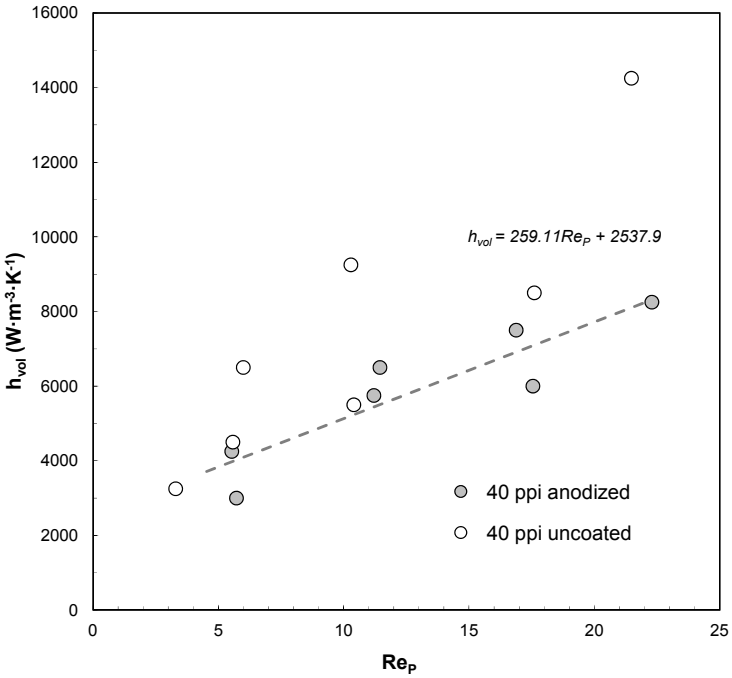

Figure 54: A correlation of experimental heat transfer values for anodized 40 ppi foam of $\varepsilon = 0.910$ to 0.920 at flow rates of $Re_P = 6$ to 22.

5.4 Thermal Efficiency

The dimensionless volumetric thermal convection efficiency parameter, $\xi_{\dot{Q}}$, was introduced in Section 2.5.5, Equation (2.11) to capture the ability of a 3D monolith to dissipate heat while minimizing pumping losses for coolant fluid and maximizing available surface area for supporting an appropriate heterocatalyst, expressed as: $\xi_{\dot{Q}} = \alpha_s^{-1} \cdot H \cdot h_{vol} \cdot k_f^{-1} \cdot \sqrt[3]{f_H}$, where α_s is the volume-specific surface area of the monolith $\left(m^2 \cdot m^{-3}\right)$, h_{vol} the volumetric heat transfer coefficient, $\left(W \cdot m^{-3} \cdot K^{-1}\right)$, H is the characteristic diameter for the monolith domain, k_f is the thermal conductivity of the heat-transfer fluid $\left(W \cdot m^{-1} \cdot K^{-1}\right)$, and f_H is the friction factor for fluid passing through a monolith-domain channel.

It follows that a large-pore foam will have lower pump losses (lower friction factor) and lower specific surface area than a small-pore foam and will thus have a higher thermal efficiency if it can transport the same amount of heat as higher-surface-area monolith at a given rate of flow. The plot of thermal efficiencies (Page 93) shows (as determined by our heat-transfer vs. pump-loss criteria), the 10 ppi foam has superior thermal transfer characteristics due to the very low friction factor associated with air flow through this foam. Anodization of the foam slightly reduces the thermal efficiency, but not as severely as changes in pore diameter. In a reaction-engineering design, a very clear choice between pump (or blower) losses and active surface area must be made – higher surface areas will entail greater pumping losses. Wherever the fluid in question is strictly used for heat transport away from a diffusive foam surface, a large-pore foam will be preferable in order to minimize pump (or blower) losses. Wherever a reactive fluid is limited by available catalyst, a small-pore foam will be preferred (at the cost of increased pumping losses).

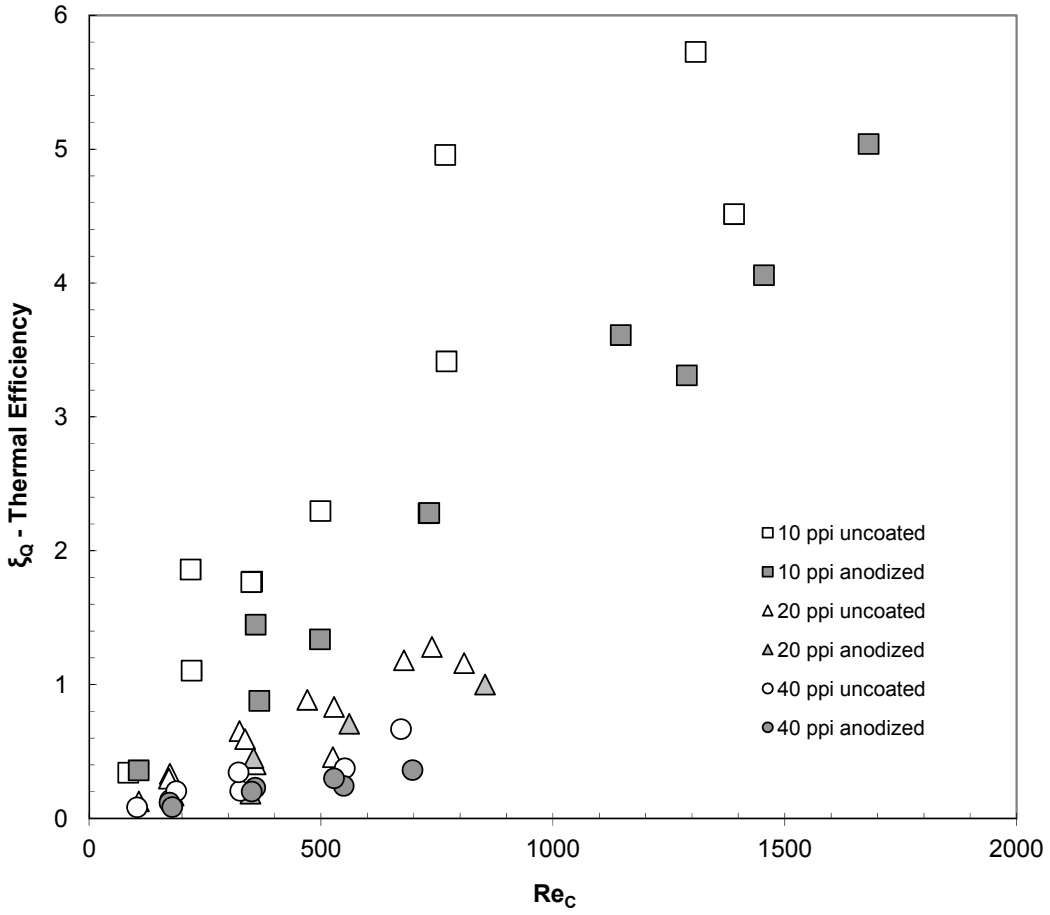

Figure 55: Thermal efficiency (as defined in Section 2.5.5) for tested foam monoliths as a function of Reynolds number.

5.5 Assessment of Methodology for Convective Heat Transfer Coefficient Determination

5.5.1 Experimental Considerations

The steady-state method proposed in this work can be used to determine the convection-transfer effects of a coating on a metal monolith. Experimental noise poses greater impacts on measurement precision when used on smaller scale monoliths and at lower flow rates (i.e., the noise-to signal ratio increases as the Reynolds number decreases). Some noise may be attributed to the potential for heat losses to the channel walls and the lack of accounting for convective fluid-phase thermal mixing in the model used to fit the volumetric convection parameter (see Section 5.5.3.2). Similar trends in noise-to-signal occurs for estimating convective heat exchange

coefficients in packed beds, even with lumped parameter models where convection phenomena are treated through third-kind boundary conditions [87].

The wall-convection coefficient estimate described by Tian and others has the advantage of lower experimental noise since local temperatures inside the monolith domain are measured strictly within the solid-phase (by drilling small-bore thermal wells into the heater/monolith boundary just beneath the heater/monolith boundary) where there is no possibility of convective thermal mixing [8, 18, 47]. However, while the wall-convection method is useful for heat-sink applications and for volumetric applications at very small scales or low Reynolds numbers (where solid-phase thermal gradients perpendicular to coolant flow are small), the resulting convection coefficients are not scaleable. Figure 49 shows how the wall-bounded methods of Equations (5.6) and (5.7) tend to overestimate the volumetric convection coefficient at low Reynolds numbers and underestimate the volumetric convection coefficient at higher Reynolds numbers for uncoated foams. The divergence in values is due to the tendency of the wall-bounded method to 1) overestimate convective driving force, ΔT_{avg}, in the heat-exchange system where the true solid phase at $y>0$ may be cooler than the corresponding solid-phase wall temperature or where coolant at $y>0$ is hotter than the inlet fluid at $y=0$ and 2) to underestimate ΔT_{avg} in the heat-exchange system at low flow rates where the fluid phase may be much hotter at $y>0$ than the temperature predicted by the simple bulk coolant temperature drop. As the flow rate increases the actual fluid and solid phase temperature profiles between $y=0$ and $y=H$ are more pronounced (particularly in the fluid phase), which reduces the true value of ΔT_{avg} while the extrapolated driving force, ΔT_{avg}, is much higher than the more-realistic physical system described in Chapter 3. The tendency of the wall-convection experiment to overestimate ΔT_{avg} at higher flow rates leads to an underestimation of the volumetric heat transfer coefficient.

The experimental method most likely to produce low noise parameters that are fully scalable would be the embedding of thermocouple probes into the solid monolith domain (at the

boundaries and within the domain). This type of measurement would be limited by the scale of the experiment (i.e., must be large enough to prevent significant coolant flow disruption due to thermocouple placement) [51].

5.5.2 Experimental Scalability

In previous work by Alvarez-Hernandez, the wall-convection coefficient was measured for a 0.0762 m ×0.0762 m × 0.0762 m 10 ppi foam sample [47]. The work reported a wall-convection coefficient, $\overline{h_w}$, of 376.41 $W{\cdot}m^{-2}{\cdot}K^{-1}$ at a flow velocity of 45 $ft^3{\cdot}min^{-1}$ (equivalent to $Re_C = 83$) The application in question in Alvarez-Hernandez was surface-heat exchange and the wall-bounded method was properly suited to this purpose. However, in volumetric application, an extrapolation of the wall-convection value would correspond to a wall-bounded volumetric coefficient, $\overline{h_{vol}}$, of 5,070 $W{\cdot}m^{-3}{\cdot}K^{-1}$, which would overestimate the values for a similar 10 ppi foam under the same flow condition in this study, where the wall-convection coefficient, $\overline{h_w}$, was 45 $W{\cdot}m^{-2}{\cdot}K^{-1}$ *(with no insulating layer, similar to the Alvarez experiment),* with a wall-extrapolated volumetric coefficient, $\overline{h_{vol}}$, of 3,570 $W{\cdot}m^{-3}{\cdot}K^{-1}$, and a model-fitted volumetric convection coefficient, h_{vol}, of 2,750 $W{\cdot}m^{-3}{\cdot}K^{-1}$. To compare flow conditions at the pore size length scale of the Alvarez 10 ppi foam flow condition ($Re_P = 3$), the most comparable comparable flow condition of this work would be the 40 ppi foam with $Re_C = 103$ and $Re_P = 3.7$, which yielded a wall-convection coefficient, $\overline{h_w}$, of 47 $W{\cdot}m^{-2}{\cdot}K^{-1}$ *(with no insulating layer, similar to the Alvarez experiment),* with a wall-extrapolated volumetric coefficient, $\overline{h_{vol}}$, of 3,700 $W{\cdot}m^{-3}{\cdot}K^{-1}$, and a model-fitted volumetric convection coefficient, h_{vol}, of 3,250 $W{\cdot}m^{-3}{\cdot}K^{-1}$.

A second convection experiment on 10 ppi foam (ε =0.914) with dimensions 0.0508 m × 0.1016 m × 0.2504 m yielded a value, $\overline{h_w}$ of 500 $W{\cdot}m^{-2}{\cdot}K^{-1}$ at a flow velocity of 1 $m \cdot s^{-1}$ (equivalent to $Re_C = 900$). In volumetric application, the same value would correspond to a wall-bounded volumetric coefficient, $\overline{h_{vol}}$, of 2,000 $W{\cdot}m^{-3}{\cdot}K^{-1}$, which is an extreme underestimate

of the values for a similar 10 ppi in this work (at an even lower Reynolds number of 771) where the wall-convection coefficient, $\overline{h_w}$, was 113 $W \cdot m^{-2} \cdot K^{-1}$ *(with no insulating layer, similar to the Alvarez experiment),* with a wall-extrapolated volumetric coefficient, $\overline{h_{vol}}$, of 8,900 $W \cdot m^{-3} \cdot K^{-1}$, and a model-fitted volumetric convection coefficient, h_{vol} of 13,750 $W \cdot m^{-3} \cdot K^{-1}$.

It is quite evident that the wall-convection method cannot yield scalable estimates of volumetric convection coefficients for volumetric application. A "full-volume" method of model fitting the forced convection coefficient, as described in Section 5.3.1, allows the experimentalist to overcome the tendency to over estimate ΔT_{avg} in fluid-heating applications and underestimate ΔT_{avg} in fluid-cooling (and thereby overestimating the volumetric heat transfer coefficient in the cooling case). The method of this work allows for more accurate estimates of heat-convection transport in monoliths with complex geometries, or in monoliths undergoing heat-coupled mass-transfer phenomena.

5.5.3 Sensitivity of Experimental Results to Modelling Parameters

The experimentally determined values of h_{vol} in this work are dependent on the fit between a set of physically observed data (Chapter 4) and a model prediction of the heat transfer phenomena under study (Chapter 3). It is not appropriate to assume that the physical model can capture all information about the experimental system, thus the effects of model parameter changes are important to determining model sensitivity to errors in experimental parameters. Among the assumptions most pertinent to the physical model are those governing the heat flux (or lack thereof) through boundaries, including:

- No substantial changes to the distribution of $y=0$ diffusive heat flux due to use of a "thermal diffuser" as shown in Figure 26, Page 58, where the copper-steel slug is used to eliminate diffusive "hot spots" due to small imperfections in the heat source or its contact surface with the steel foam.

- Pure diffusive (conductive) heat flux from the heat source into the *y=0* solid phase of the monolith and not into the *y=0* fluid phase, which is physically equivalent to having all convective heat exchange between the monolith and coolant with no convective exchange between the surface of the heater and the coolant (B.C. 7 of Section 3.3.7).
- Zero diffusive heat flux through an insulating layer (B.C. 8, 10 and 11 of Section 3.3.7).

5.5.3.1 Addition of a Thermal Diffuser

The inclusion of a steel thermal diffuser between the heat source and the solid monolith in the model does not materially change the integrative boundary assumption (B.C. 7 of Section 3.3.7). However, the presence of a refractive influence (for series resistors) has a small impact on the temperature distribution of the monolith at *y=0* (*Figure 19* on Page 45), which is exemplified by the solid-phase temperature distribution for the model of this effect in Figure 64 on Page 107. Changes to the distribution of heat exchange within the monolith (assuming perfect insulation) have a potential impact on the recovered value of h_{vol} as described in Section 4.5 because of slight distortion to the solid phase temperature heat flux compared to the simple model of Chapter 3.

The model-fitting method of Section 4.5 was applied for all experimental samples, with the model modified to include the copper-steel integrator between the strip heater surface and the metal foam monolith used in the experiments described in Section 4.5. From the results shown in Figure 56 it was concluded that the inclusion of the steel diffuser has a negligible impact on the determination of h_{vol} from model-fitted experimental data.

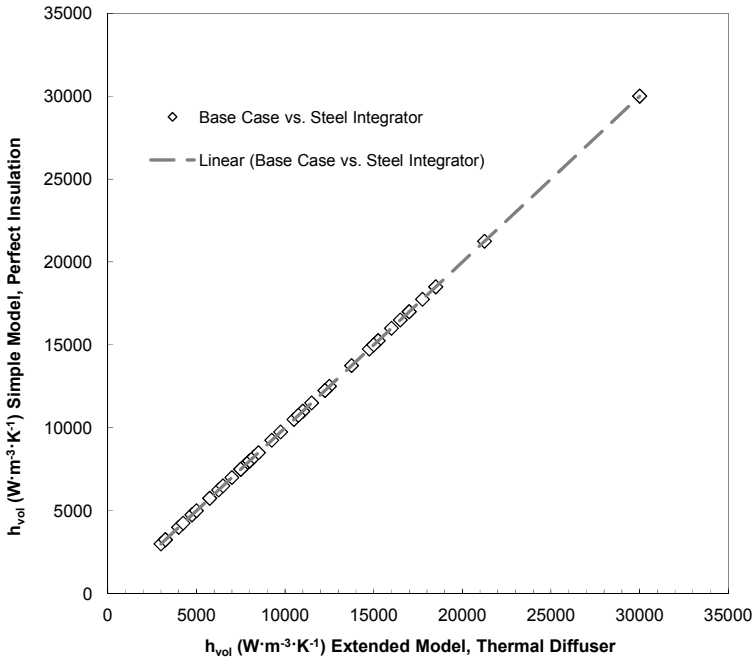

Figure 56: The effect of adding the thermal diffuser to the model is shown to be insignificant.

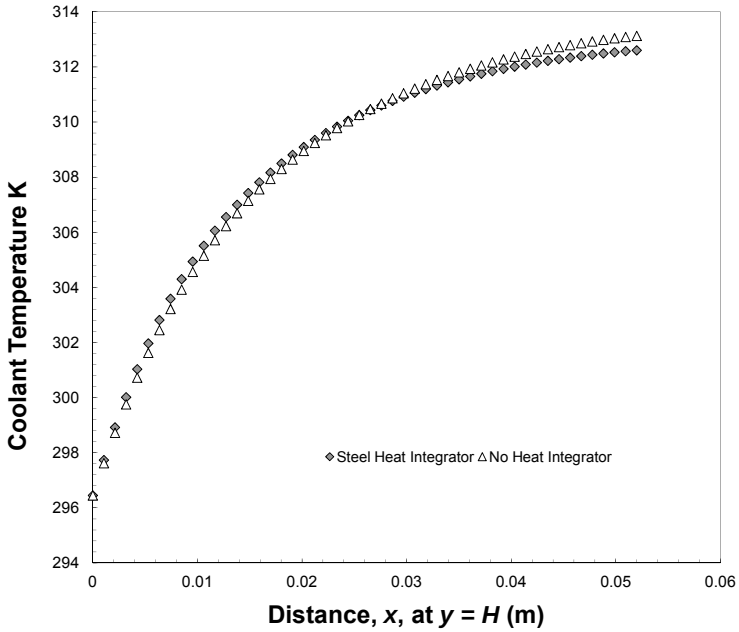

Figure 57: The impact of adding a heat integrator on the y=H coolant temperature is shown to be minor with respect to the distribution of coolant temperature within the domain of interest (with insignificant consequences to the recovered convective heat transfer coefficient).

5.5.3.2 Heater-Foam Boundary: Effect of Heat Flux-Split Ratio between Foam Monolith and Fluid (Air)

The assumption of the heat-transfer model in Section 3.3.7 (B.C. 7) states that all heat forced into the fluid-monolith system enters via diffusive flux (conduction) into the solid monolith at *y=0* (*Figure 19*), i.e., no heat is transferred from the heater to the fluid. This assumes that the area of the exposed heating surface is insignificant compared with that of the monolith and that the heater must not act as a significant site of convective heat transfer to the coolant passing over it. It also assumes, in the case of a heater insulated system (i.e., with refractive-cement barrier sealing the pores, as per Figure 28 on Page 59), that the heating surface can be perfectly insulated from the coolant – forcing all heat flux into the solid monolith as per B.C. 7. If the model assumption is wrong and a significant portion of the convective transfer occurs between the heating surface and the coolant (the surface of the steel copper integrator at *y=0*), then the total heat exchange burden between the monolith and the coolant fluid (air) must be reduced throughout the monolith domain since a significant portion of total energy conservation will be due to convection directly into the coolant at the *y=0* boundary. In such a case, since the net energy transferred must be conserved, the model estimate of h_{vol} must increase above its true value (i.e., the convective efficiency of the monolith must be overestimated in order for the model to account for energy conservation in the case where much of the unaccounted convective transfer occurred between the heating surface and the coolant as implied in Equation (5.9)).

$$h_{vol}^{true}(T_s - T_f) + h_{h.surf.}^{est} A_{h.surf.}(T_s - T_f) = h_{vol}^{est}(T_s - T_f) \tag{5.9}$$

To test the sensitivity of the model to direct heater-to-coolant convective heat exchange, the ratio of the total heat flux into the coolant at *y=0* is varied from 0% to 100% while the experimental data are fit in the method of Section 4.5.

Figure 58 (on Page 101) shows the modelled heat profile at *y=H* when the fraction of heat transferred into the monolith at *y=0* is varied. In the case where no heat is exchanged to the fluid from the heater at *y=0* (when the split ratio is 0%), all of the heat must be removed via

convective transfer in the bulk of the foam and the average temperature of the fluid stream must be slightly higher at $y=H$.

The most important impact of changing heat flux split ratio is apparent in Figure 59 on Page 102 where the experimental data are fit to the model (with varied amounts of solid phase vs. fluid phase diffusive flux at $y=0$). The recovered values of h_{vol} are sensitive to the relative distribution of heat flux into the solid phase vs. fluid phase. In several cases where experimental results at low Reynolds numbers are fitted to a model with all diffusive heat transferred to the fluid phase at $y=0$, the estimated value of h_{vol} is increased by a factor of 0.3 (Figure 60). The magnitude of this effect is not changed significantly when an insulating layer (refractory cement putty) is used to thermally isolate the heating surface from the coolant (air), but it is greater in the case of anodized monoliths than in uncoated monoliths. The increased sensitivity in results for the anodized monoliths is a consequence of the relationship expressed in Equation (5.9) where a lower value for h_{vol}^{true} must lead to a higher value of h_{vol}^{est} as the value of $h_{h.surf.}^{est}$ increases.

Given the non-homogeneous contact between the experimental heating surface and the monolith due to the non-regular texture of the monolith (Figure 28), the experimental inability to fully isolate convective transfer from heating surface-to-fluid from monolith-to-fluid poses an important contribution to experimental uncertainty as the heat-transfer assumptions may not reflect the local experimental phenomena at $y=0$. However, the sensitivity of h_{vol} to these uncertainties shows that this experimental issue poses the most significant problem in recovering accurate physical parameters for the processes in question. Nonetheless, it is remarkable that despite the difficulty in perfectly isolating the heating surface from the fluid, the maximum error in estimated volumetric heat transfer co-efficient is 30%. If a split ratio of 50% is assumed, the error in estimated heat transfer coefficient is less than 10% for nearly the whole range of Reynolds numbers examined.

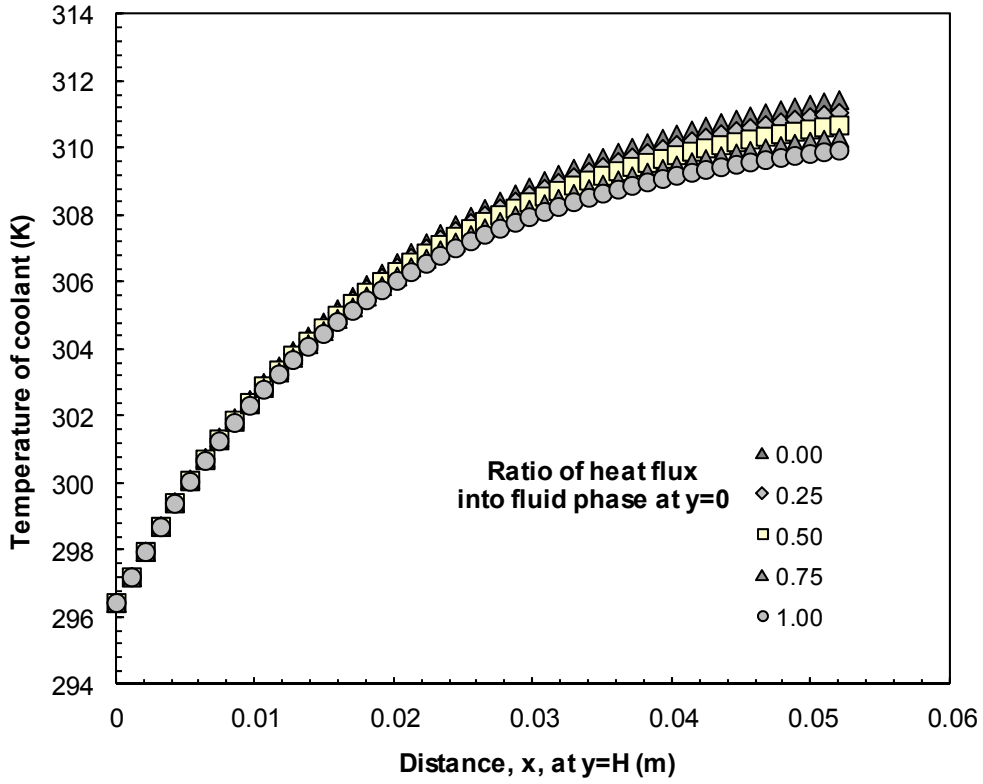

Figure 58: Effect of heat-flux split ratio (fluid phase) at y=0 on model coolant temperatures measured at y=H

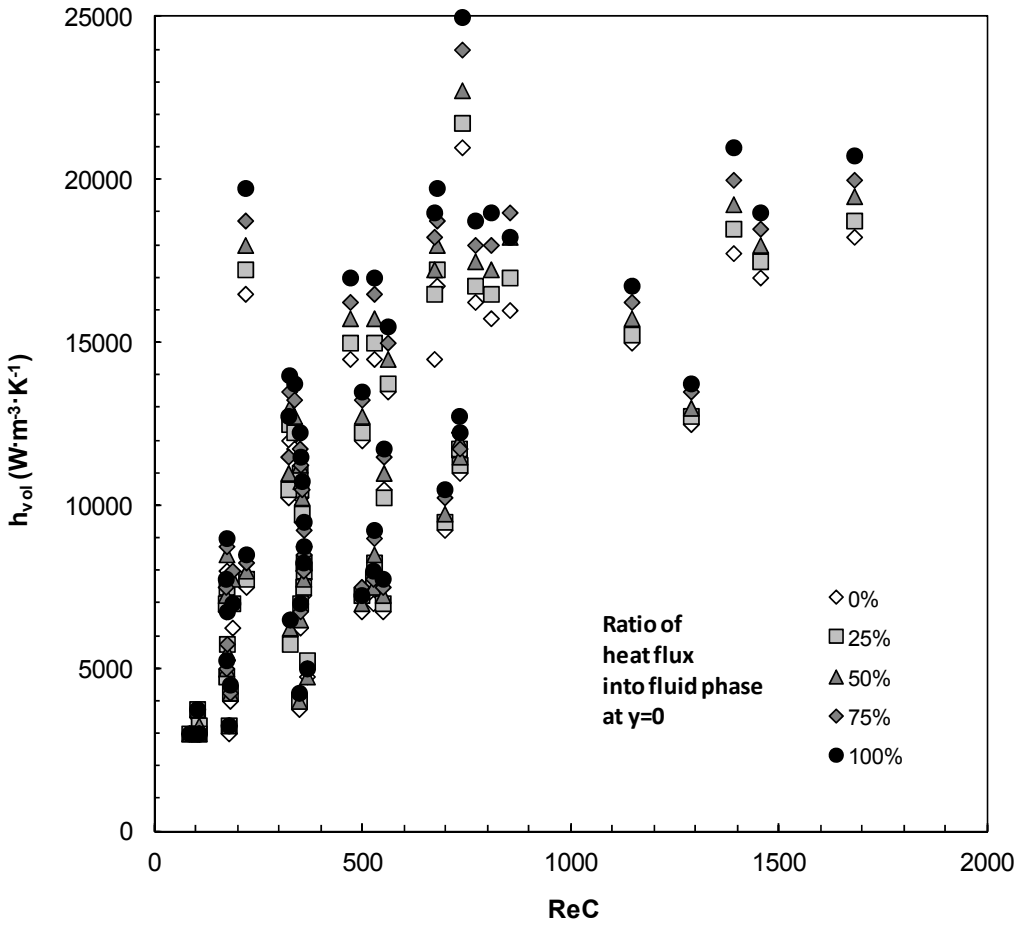

Figure 59: Volumetric convective heat transfer coefficients change substantially depending on the fraction of total heat diffused into the monolith at y=0 (vs. heat convected away directly at the heating surface).

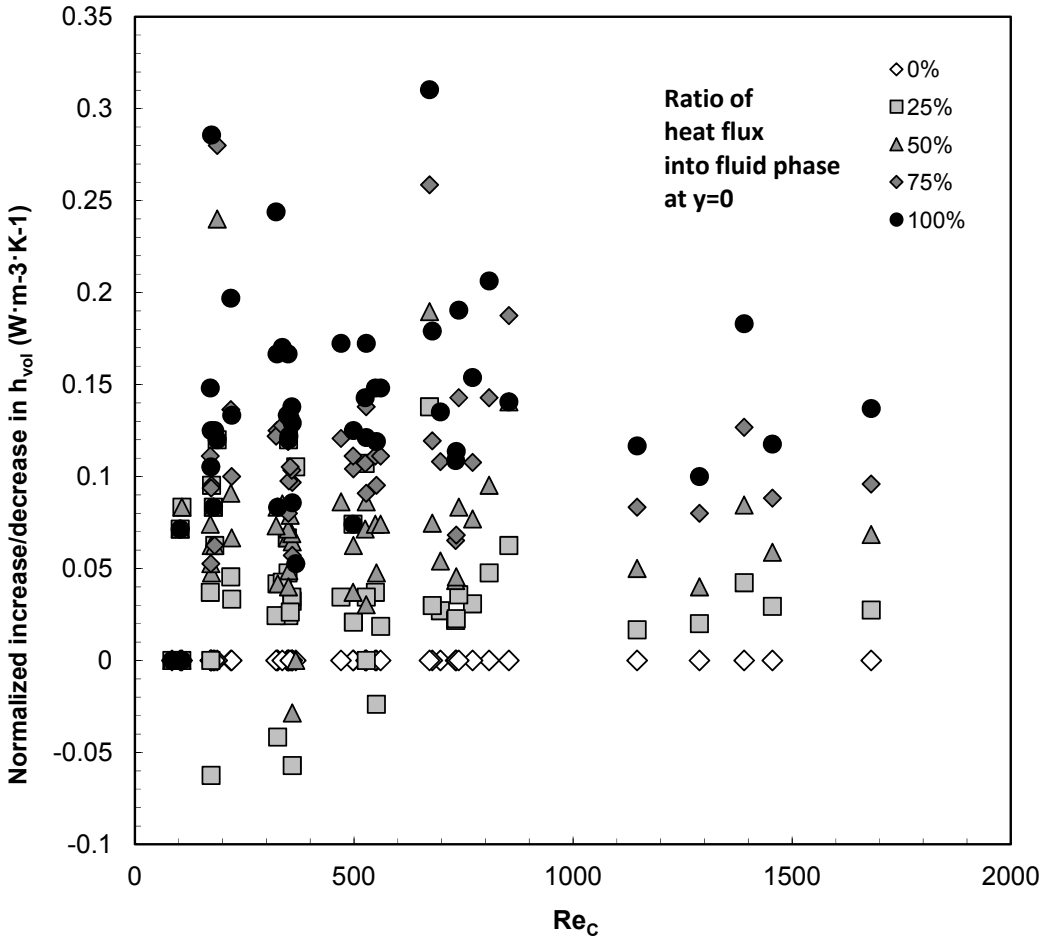

Figure 60: The fractional increase (or decrease) in fitted estimates of h_{vol} for coated/anodized foam monoliths plotted as a function of channel Reynolds number for different heat flux ratio ranging 0-100%

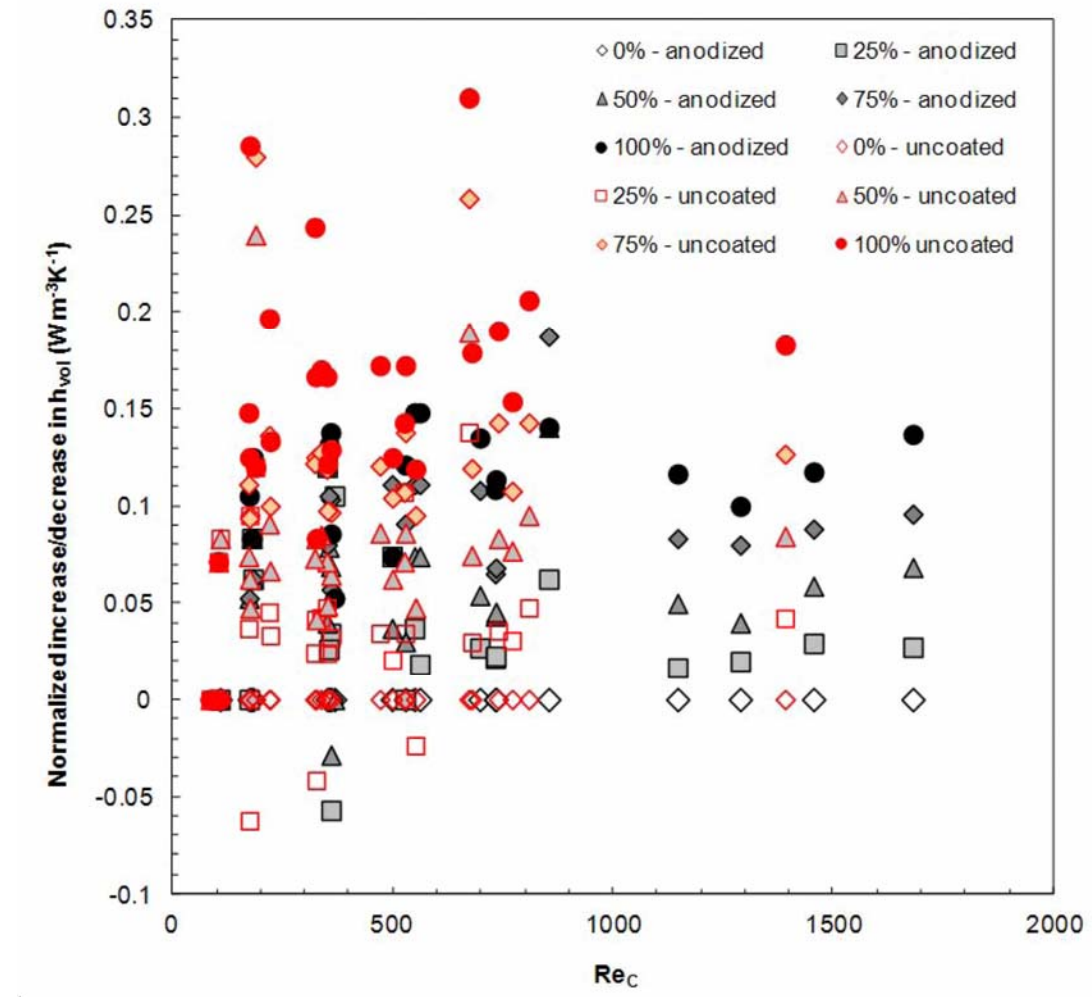

Figure 61: The fractional increase (or decrease) in fitted estimates of volumetric convection coefficients is larger for uncoated monoliths than for anodized monoliths as the modelled heat diffused into the fluid phase at y=0 increases from 0% to 100%

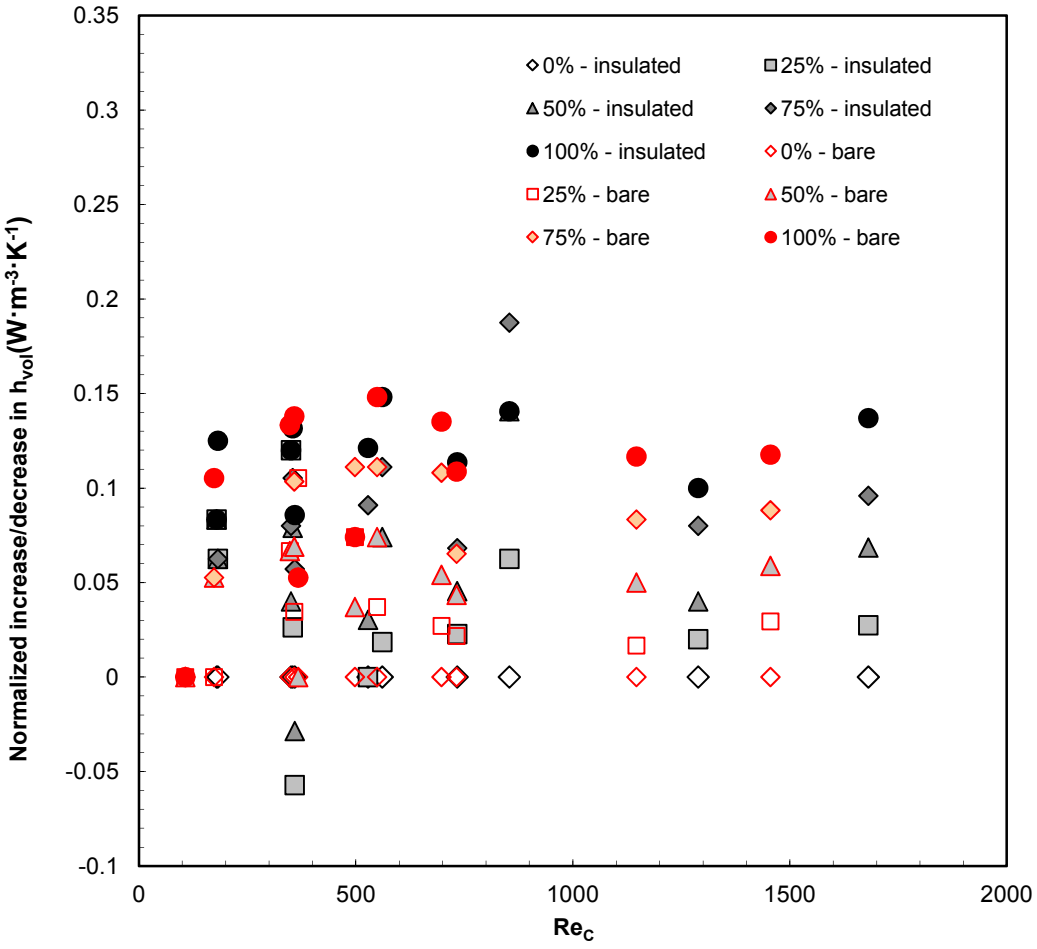

Figure 62: The fractional increase (or decrease) in fitted estimates of h_{vol} for anodized monoliths, with and without an insulating barrier between the heater and the monolith (Figure 28), as the modelled heat diffused into the fluid phase at y=0 increases from 0% to 100%.

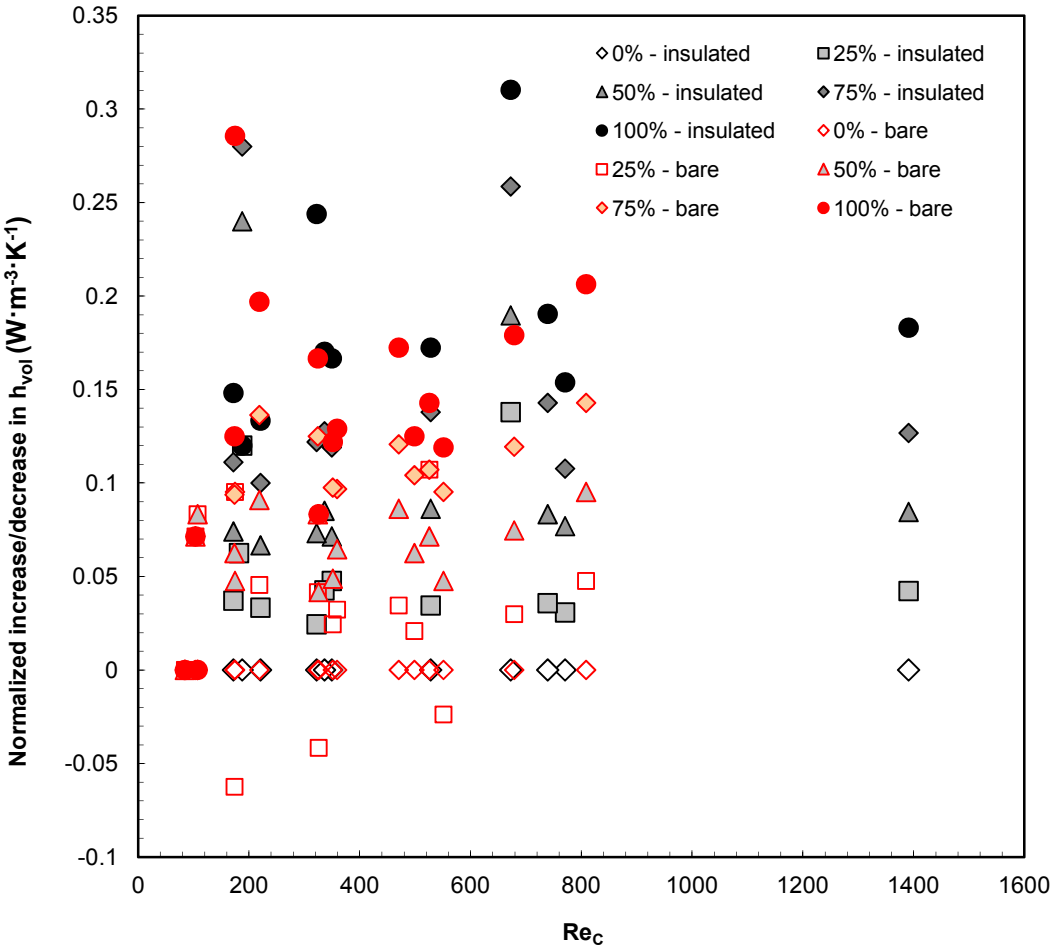

Figure 63: The fractional increase (or decrease) in fitted estimates of volumetric convection coefficients for uncoated monoliths with and without an insulating barrier between the heater and the monolith (Figure 28), as the modelled heat diffused into the fluid phase at y=0 increases from 0% to 100%

5.5.3.3 Considering the Effect of Imperfect Insulating Materials

The insulating material used to construct the walls of the experimental apparatus has a reported conductive coefficient of less than 0.1 $W \cdot m^{-1} \cdot K^{-1}$. Under the boundary assumptions of Section *3.3.7*, the polystyrene material is assumed to be a perfect insulator. If the insulation did conduct heat at an appreciable rate, it would have an impact on the thermal gradient in the heating body and the monolith (and hence a potential impact on the recovered convective coefficient). The test case of fitting experimental data to a model with 5 $W \cdot m^{-1} \cdot K^{-1}$ conducting material is shown in Figure 64 at the insulating boundaries. Figure 65 shows that the recovered

values of h_{vol} in the case of very poor insulation do not deviate significantly from the estimated value of h_{vol} under the assumed experimental conditions of non-conductive containment walls (i.e., changes to the internal solid-phase heat gradients and subsequent distribution of convective exchange are minor).

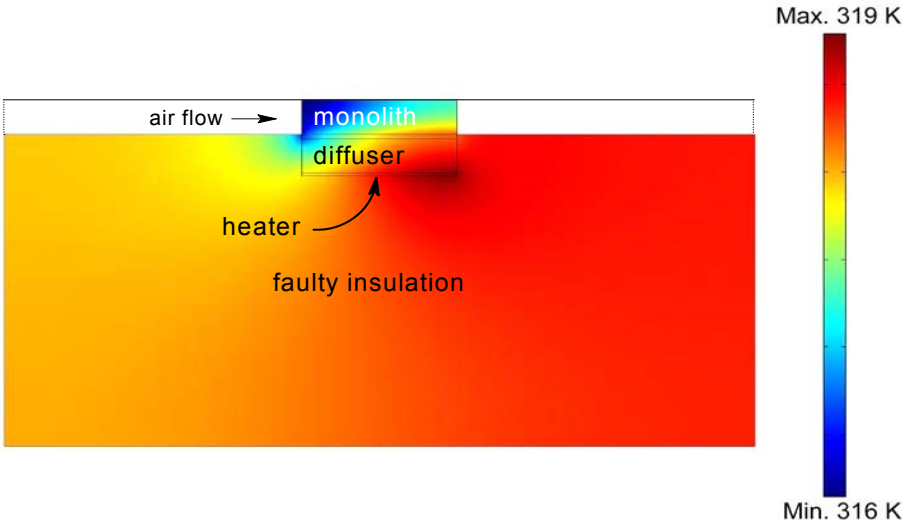

Figure 64: A modified version of the heat-exchange model (solid-phase temperatures) with an added steel integrator and a "faulty" insulation layer (5 $Wm^{-1}K^{-1}$)

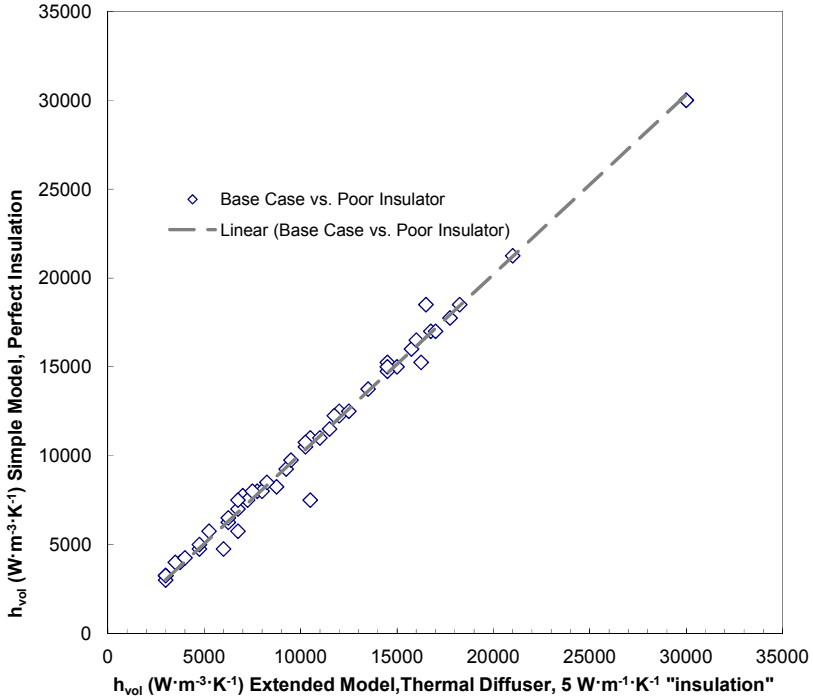

Figure 65: Introduction of insulation failure into the model has negligible impact on recovered values of h_{vol}.

5.5.3.4 Potential Impact of Boundary Effects on Model Predictions

As seen in Figure 39, the *y=H* fluid temperatures collected in the experiment tend to overestimate model-generated temperature values in the first half of the monolith (*x=0..x=L/2*) and underestimate model-generated values in the second half of the monolith (*x=L/2..x=L*). In other words, the driving force, $T_s - T_f$ is underestimated in the first half of the monolith and overestimated in the second half portion of the monolith. This modest discrepancy suggests that the flow profile of the model is not identical to what is assumed in the model. The model described in Chapter 3 assumes a plug flow at all points in the monolith as per Equation (3.14) with no consideration of boundary slip conditions at *y=0* and *y=H,* where the experimental data is collected. However, where the Kaviany assumption of stochastic (plug) flow [88] is likely to hold for lower porosity foams at higher flow rates, Hwang [57] showed, via smoke thread studies that air flow may be continuous through a vertically oriented 0.0127 m thick ε =0.95 aluminium

foam, but not through an ε =0.70 foam, as illustrated in Figure 66, where continuous smoke threads are unable to penetrate the entrance of the lower porosity foam but pass through the high porosity foam with a modified velocity profile.

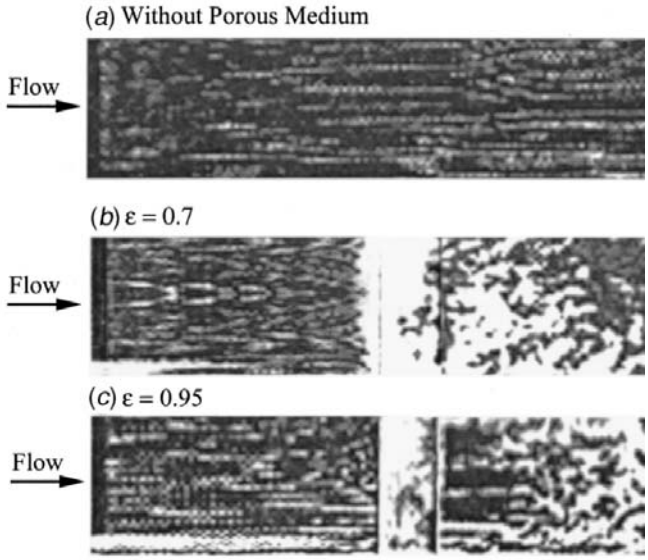

Figure 66: (Taken from Hwang et al. [57]) Smoke thread images of non-plug-flow through a thin section of aluminium foam.

When the mean plug-flow velocity predicted in this work's PDE model is re-distributed as a function of y consistent with classical turbulent flows (due to forced mixing rather than high Reynolds flow) then the predicted fluid-temperature profile is significantly altered despite the preservation of identical mass, momentum and energy balances (Figure 67 and Figure 68). Clearly, wall boundary effects and developing velocity profiles may have significant impact on model temperature profiles.

It is notable that the plug-flow model-fitting technique of this work is successful in recovering convection coefficients that are equivalent to scalable, non-steady-state experiments (Figure 51) that do not depend on momentum transfer assumptions. However, despite the accuracy of the plug-flow model, a more robust approximation of the fluid momentum transfer, especially for low Reynolds flows through highly porous monoliths would be warranted to increase the precision of

the fit between experimental observation and model prediction (see recommendations for future work in Chapter 7).

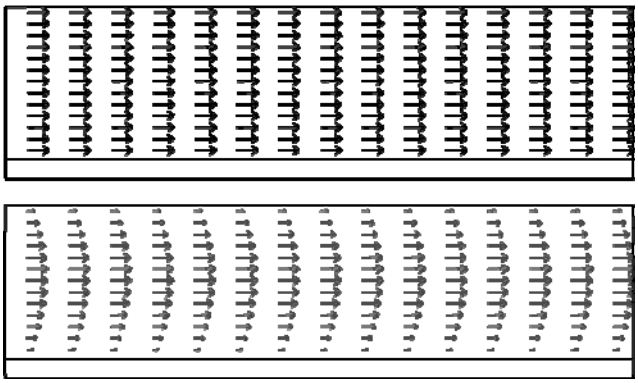

Figure 67: Velocity profiles of the experimental model system with plug flow assumption (top) and with an arbitrary fully developed turbulent flow distribution (bottom)

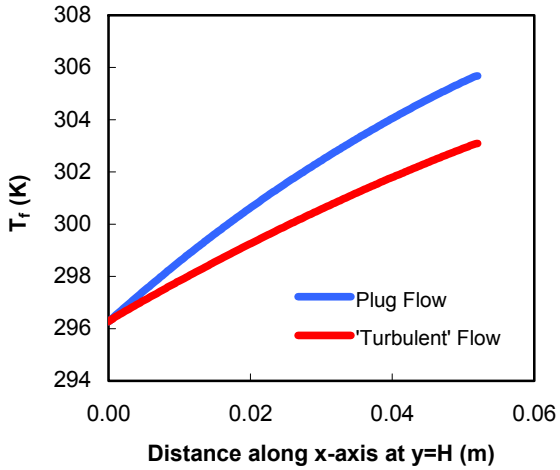

Figure 68: Fluid temperature profiles predicted by the plug flow and turbulent velocity profiles.

Chapter 6: Reactor Design Using Experimental Data

In this chapter, the results of Chapter 5 are exploited to model a simple, non-isothermal coupled heat, momentum and mass transfer system based on the postulated heat-exchanger/methanol steam reforming reactor in Chapter 1. The modelled reactor monolith solid state temperatures are assessed to determine sensitivity to the impact of convective heat transfer changes (due to presence of catalyst support coating) as are reactor yields.

6.1 A Coupled Heat-Exchange Combustion-Fired Methanol Steam Reformer

In Chapter 1.1 the concept for a coupled heat-exchange/fuel-reformer was introduced as a motivation for determining the impacts of a catalyst support coating on the convective transport efficiency of a metal foam monolithic substrate. The model system introduced in Chapter 3 is extended here to model a practical, non-isothermal device (Figure 69). In this concentric-tube system, heat evolved from a nominal combustion source is diffused through a cylindrical aluminium foam core, through a gas-impermeable copper boundary and into a concentric cylindrical aluminium foam coated with CH18HC (*CuO/ZnO* on Al_2O_3 support) catalyst. The catalyst monolith is fed a stream of pure methanol and steam (Figure 2, on Page 3). This model system includes an energy balance on the solid phase of the system, an energy balance on the gas-phase of the system, a momentum balance on the gas phase of the system, and five mass balances on the gas species: methanol, steam, hydrogen, carbon dioxide and carbon monoxide.

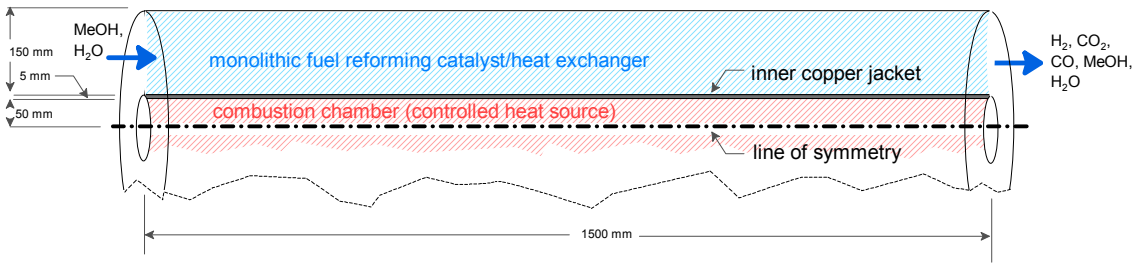

Figure 69: The model coupled heat-exchange fuel reforming system.

6.2 Domain Description

The domain under consideration is a two-dimensional slice through the concentric tube system. It is a two-phase solid-gas system, with a fixed heat-generation profile through the inner exothermic-reaction vessel and heat transfer to an outer endothermic reaction chamber with a feed stream of steam and methanol (Figure 69). The two concentric cylindrical chambers consist of an inner cylinder of aluminium foam monolith of length 1.5 m, inner diameter 0.1 m, a copper shell 0.005 m thick which jackets the inner monolith and and an outer hollow-cylinder monolith with an outer diameter of 0.31 m. The inner and outer monolith cylinders are thermally bonded (brazed) to the interior copper jacket and the external cylinder is insulated at its outer diameter. The inner monolith is the site of a nominal combustion reaction supplying heat to drive steam reforming reactions in the "shell" (reactions (6.1) through (6.3), according to the Amphlett empirical-kinetic model, which is particularly appropriate for modelling a non-isobaric, non-isothermal system such as this because of the broad temperature range for which the kinetics are validated [89, 90]. Full boundary conditions for the system are described in Figure 70 and Section 6.2.3.

$$CH_3OH + H_2O \rightleftarrows 3H_2 + CO_2 \tag{6.1}$$

$$CH_3OH \rightleftarrows CO + 2H_2 \tag{6.2}$$

$$CO + H_2O \rightleftarrows CO_2 + H_2 \tag{6.3}$$

6.2.1 Assumptions

- All assumptions of Chapter 3.3.3 hold in the reactor domain.
- Reactions take place on the surface of the monolith and the heat evolved from these reactions is transferred to the solid phase via diffusive heat transfer (as per Figure 3 on page 4). Subsequent heat transfer to the bulk fluid phase is via convection from the monolith to the fluid phase.

- Intra-catalyst mass-transfer effectiveness, η, (relative to published results for packed beds) is unity due to the relative thinness of the support layer on the metal foam [91].
- Catalyst mass density is equivalent to 20% of the solid monolith substrate, which is based on alumina loading results described in Appendix B.
- As a model approximation, CH18HC-catalyst coated aluminium monoliths of a given porosity and mass density have the same Darcy-Forchheimer permeability as the analogous anodized monoliths testing in Chapters 5 and 6.
- The gas-phase physical properties are strong functions of temperature and will behave as a mole-fraction-weighted average of the component gas species' properties.
- Gas-species follow ideal-gas behaviour under the pressure and temperature conditions assigned in the model
- The effect of mixing of the gas phase has insignificant impact over the temperatures and concentration profiles of the fluid phase at the macro length scale of the reactor (i.e., forced mixing due to tortuous flows is not considered in this model).
- Gas-diffusion is an insignificant mode of fluid transport and is set in the model at a fixed value of $1.6\times10^{-6} m^2 \cdot s^{-1}$ for all species.

6.2.2 Governing Equations

6.2.2.1 Heat Transfer in the Solid Phase

$$\nabla\bullet\left(-k_s\nabla T_s\right)=h\left(T_s-T_f\right)+\sum\left(r_i\Delta H_{rxn_i}\right) \tag{6.4}$$

6.2.2.2 Heat Transfer in the Fluid Phase

$$\nabla\bullet\left(-k_f\nabla T_f+\rho_f C_{p_f}\mathbf{v}_f T_f\right)=h\left(T_f-T_s\right) \tag{6.5}$$

6.2.2.3 Momentum Transfer in the Fluid Phase Including Source Coefficient, S_p, to Account for Change in Number of Gas Species (within a fixed/specified pressure drop regime).

$$\nabla\bullet\left(\frac{2\rho_f}{\frac{\mu}{\mathrm{K}}+\sqrt{\left(\frac{\mu}{\mathrm{K}}\right)^2+4C_F|\nabla\mathbf{P}|}}(-\nabla\mathbf{P})\right)-S_p=0$$

$$where\ S_p=\frac{\Delta n_f}{n_f}RT_f \tag{6.6}$$

6.2.2.4 Mass Transfer of the Fluid-Phase Species, i, Where D_i is the Species Diffusion Constant, R_i is the Species Consumption/Generation Source Term and c_i is the Species Concentration:

$$\nabla\bullet\left(-D_i\nabla c_i\right)=R_i-\nabla\bullet\left(\mathbf{v}c_i\right),$$

$$where\ \mathbf{v}=\frac{-2\nabla\mathbf{P}}{\frac{\mu}{\mathrm{K}}+\sqrt{\left(\frac{\mu}{\mathrm{K}}\right)^2+4C_F|\nabla\mathbf{P}|}}\cdot S_p \tag{6.7}$$

6.2.3 Boundary Conditions

The following boundary conditions are imposed on the above model. All boundary conditions chosen are physically meaningful and/or experimentally realizable. The domain boundaries and the flow directions are shown in Figure 70 below:

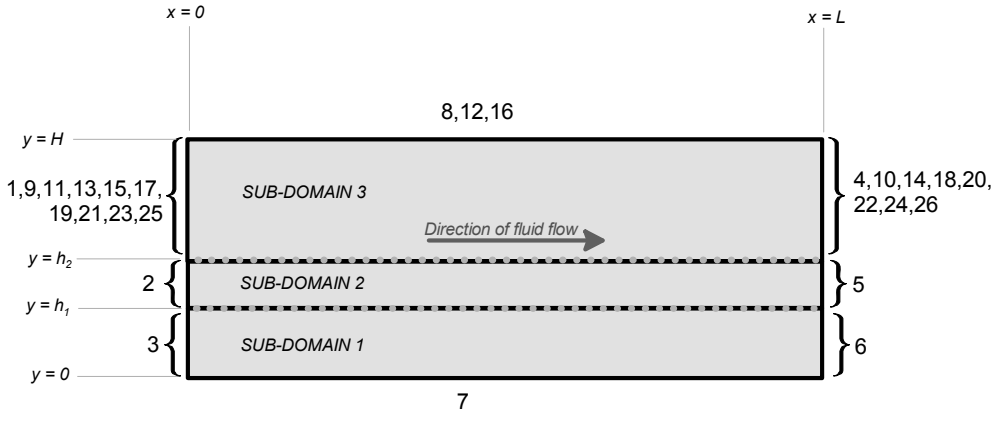

Figure 70: Boundary conditions imposed on the reactive two-phase forced convection model for methanol steam reforming in a catalyst coated aluminum foam monolith.

6.2.3.1 Solid Phase Energy Balance Boundary Conditions

B.C. 1-3 (Zero convective transfer [solid phase])

$$\rho_s C_p \mathbf{v}_s \nabla T_s \Big|_{x=0} = 0$$

B.C. 4-6 (Zero convective transfer [solid phase])

$$\rho_s C_p \mathbf{v}_s \nabla T_s \Big|_{x=L} = 0$$

B.C. 7 (Symmetry plane)

$$-k_s \frac{dT_s}{dy}\bigg|_{y=0} = 0$$

B.C. 8 (Insulation)

$$-k_s \frac{dT_s}{dy}\bigg|_{y=H} = 0$$

6.2.3.2 Fluid Phase Energy Balance

B.C. 9 (Temperature of Fluid Phase specified)

$$T_f \Big|_{x=0,y=h_2}^{x=0,y=H} = T_{f_{in}}$$

B.C. 10 (Heat removed from the system in the fluid phase is equal to heat generated in sub-domain 1)

$$\int_{x=L,y=h_2}^{x=L,y=H} \rho_f C_{p_f} \mathbf{v}_f \nabla T_f dy - \int_{x=0,y=h_2}^{x=0,y=H} \rho_f C_{p_f} \mathbf{v}_f \nabla T_f dy = \int_{y=0}^{y=h_1} \int_{x=0}^{x=L} Q_{vol} dx dy$$

B.C. 11 (Zero convective or diffusive heat transfer into sub-domain 3)

$$\left(\rho_f C_{p_f} \mathbf{v}_f \nabla T_f - k_f \nabla T_f\right)\Big|_{y=h_2} = 0$$

B.C. 12 (Zero convective or diffusive heat transfer into sub-domain 3)

$$\left(\rho_f C_{p_f} \mathbf{v}_f \nabla T_f - k_f \nabla T_f\right)\Big|_{y=H} = 0$$

6.2.3.3 Momentum Balance

B.C. 13 (Known pressure at inlet)

$$p\big|_{x=0} = p_{in}$$

B.C. 14 (Known pressure at outlet)

$$p\big|_{x=L} = p_{out}$$

B.C. 15 (Zero normal-pressure gradient at wall)

$$\left.\frac{dp}{dy}\right|_{y=0} = 0$$

B.C. 16 (Zero normal-pressure gradient at wall)

$$\left.\frac{dp}{dy}\right|_{y=0} = 0$$

6.2.3.4 Mass Balances

B.C. 17 (Known inlet concentration)

$$c_{CH_3OH}\Big|_{x=0,y=h_2}^{x=0,y=H} = c_{CH_3OH_{in}}$$

B.C. 18 (Convective flux at outlet equal to net generation in Sub-Domain 3)

$$\int_{x=L,y=h_2}^{x=L,y=H} \mathbf{v}_f \nabla c_{CH_3OH} dy - \int_{x=0,y=h_2}^{x=0,y=H} \mathbf{v}_f \nabla c_{CH_3OH} dy = \int_{y=0}^{y=h_1} \int_{x=0}^{x=L} R_{CH_3OH} dx dy$$

B.C. 19 (Known inlet concentration)

$$c_{H_2O}\Big|_{x=0,y=h_2}^{x=0,y=H} = c_{H_2O_{in}}$$

B.C. 20 (Convective flux at outlet equal to net generation in Sub-Domain 3)

$$\int_{x=L,y=h_2}^{x=L,y=H} \mathbf{v}_f \nabla c_{H_2O} dy - \int_{x=0,y=h_2}^{x=0,y=H} \mathbf{v}_f \nabla c_{H_2O} dy = \int_{y=0}^{y=h_1} \int_{x=0}^{x=L} R_{H_2O} dxdy$$

B.C. 21 (Known inlet concentration)

$$c_{H_2}\Big|_{x=0,y=h_2}^{x=0,y=H} = c_{H_{2in}}$$

B.C. 22 (Convective flux at outlet equal to net generation in Sub-Domain 3)

$$\int_{x=L,y=h_2}^{x=L,y=H} \mathbf{v}_f \nabla c_{H_2} dy - \int_{x=0,y=h_2}^{x=0,y=H} \mathbf{v}_f \nabla c_{H_2} dy = \int_{y=0}^{y=h_1} \int_{x=0}^{x=L} R_{H_2} dxdy$$

B.C. 23 (Known inlet concentration)

$$c_{CO_2}\Big|_{x=0,y=h_2}^{x=0,y=H} = c_{CO_{2in}}$$

B.C. 24 (Convective flux at outlet equal to net generation in Sub-Domain 3)

$$\int_{x=L,y=h_2}^{x=L,y=H} \mathbf{v}_f \nabla c_{CO_2} dy - \int_{x=0,y=h_2}^{x=0,y=H} \mathbf{v}_f \nabla c_{CO_2} dy = \int_{y=0}^{y=h_1} \int_{x=0}^{x=L} R_{CO_2} dxdy$$

B.C. 25 (Known inlet concentration)

$$c_{CO}\Big|_{x=0,y=h_2}^{x=0,y=H} = c_{CO_{in}}$$

B.C. 26 (Convective flux at outlet equal to net generation in Sub-Domain 3)

$$\int_{x=L,y=h_2}^{x=L,y=H} \mathbf{v}_f \nabla c_{CO} dy - \int_{x=0,y=h_2}^{x=0,y=H} \mathbf{v}_f \nabla c_{CO} dy = \int_{y=0}^{y=h_1} \int_{x=0}^{x=L} R_{CO} dxdy$$

6.3 Kinetics

The volumetric mass-transfer R_i, is a function of reaction rate, which is in turn modelled by the semi-empirical model developed by Amphlett et al. for steam reforming of methanol on the commercial low-temperature shift catalyst CH18HC (CuO/ZnO on Al_2O_3 support), which was experimentally validated for temperatures between 433 K to 493 K and pressures of 1 to 3 atm.

The rates of reaction for each species are determined by Equations (6.8) through (6.12) [90]. The reverse water gas shift (WGS) of Equation (6.3) is treated as insignificant with respect to the forward reaction.

$$r_{CH_3OH} = -k_1 c_{CH_3OH} - k_2 \tag{6.8}$$

$$r_{H_2O} = -k_1 c_{CH_3OH} \tag{6.9}$$

$$r_{H_2} = 3k_1 c_{CH_3OH} + 2k_2 \tag{6.10}$$

$$r_{CO_2} = k_1 c_{CH_3OH} \tag{6.11}$$

$$r_{CO} = k_2 \tag{6.12}$$

The rate constants k_1 and k_2 are given in Equation (6.13) and (6.14), with parameters in Table 6 where ρ_{CH18HC} is the mass density of catalyst in the monolith.

$$k_1 = \frac{\left[A_1 + B_1 \ln\left(\frac{S}{M}\right)\right] \exp\left(\frac{-E_1}{RT}\right)}{p^{D_1}} \rho_{CH18HC} \tag{6.13}$$

$$k_2 = \frac{A_2 \exp\left(\frac{-E_2}{RT}\right)}{p^{D_2}} \rho_{CH18HC} \tag{6.14}$$

Table 6: Parameters for rate constants (Amphlett et al.)

Parameter	Value	Units
A1	1.15×10^{6}	$m^{3}\cdot s^{-1}\cdot kg^{-1}$
B1	9.41×10^{5}	$m^{3}\cdot s^{-1}\cdot kg^{-1}$
E1	8.41×10^{4}	$J\cdot mol^{-1}$
D1	1.46×10^{0}	
A2	7.09×10^{7}	$mol\cdot s^{-1}\cdot kg^{-1}$
E2	1.112×10^{5}	$J\cdot mol^{-1}$
D2	3.00×10^{-1}	

6.4 Physical Properties

Physical properties for the solid phase are identical to those introduced in Chapter 3. Fluid-phase physical properties in Equations (6.15),(6.17) and (6.23) are taken from NIST data and from Fenghour [92] Teske [93] and Xiang [94]. The correlation of h_{vol} from the modelled fluid regime (steam reforming species) to the experimental fluid regime (air) is taken from standard dimensional analysis of convective transfer for laminar regimes, where the average convective transfer is proportional to $Cp^{0.33}$ [95]. This relationship can be exploited to estimate h_{vol} for a gas mixture based on experimental h_{vol} for air at the same flow regime (see correlation function in Figure 71). The gas diffusion coefficients, D_i, are fixed for all gas species as described in Section 6.2.1.

$$\rho_f = \sum \rho_i \tag{6.15}$$

$$\rho_i = MW_i \frac{p_i}{RT} \tag{6.16}$$

$$C_{p_f} = \sum \left[\left(\frac{\rho_i}{\rho_f} \right) C_{p_i} \right] \tag{6.17}$$

$$Cp_{CH_3OH} = -8.00\times10^{-5}T_f^3 + 1.124\times10^{-1}T_f^2 - 5.1544\times10^{1}T_f + 9.3611\times10^{3} \quad (6.18)$$

$$Cp_{H_2} = 2.00\times10^{-5}T_f^3 - 2.930\times10^{-2}T_f^2 + 1.4117\times10^{1}T_f + 1.2197\times10^{3} \quad (6.19)$$

$$Cp_{H_2O} = -7.00\times10^{-5}T_f^3 + 1.072\times10^{-1}T_f^2 - 5.2773\times10^{1}T_f + 1.0618\times10^{4} \quad (6.20)$$

$$Cp_{CO_2} = 6.00\times10^{-7}T_f^3 - 1.6\times10^{-3}T_f^2 + 1.7708\times10^{0}T_f + 4.4679\times10^{2} \quad (6.21)$$

$$Cp_{CO} = -6.00\times10^{-9}T_f^3 - 7.00\times10^{-4}T_f^2 + 1.3158\times10^{0}T_f + 5.522\times10^{2} \quad (6.22)$$

$$\mu_f = \sum\left[\left(\frac{ci}{c_f}\right)\mu_i\right] \quad (6.23)$$

$$\mu_{CH_3OH} = 3.00\times10^{-8}T_f - 8.00\times10^{-7} \quad (6.24)$$

$$\mu_{H_2} = 2.00\times10^{-8}T_f + 4.00\times10^{-6} \quad (6.25)$$

$$\mu_{H_2O} = 4\times10^{-8}T_f - 3\times10^{-6} \quad (6.26)$$

$$\mu_{CO_2} = 4.00\times10^{-8}T_f + 2.00\times10^{-6} \quad (6.27)$$

$$\mu_{CO} = 3.4\times10^{-2}T_f + 8.257\times10^{-1} \quad (6.28)$$

$$h_{vol_f} = f\left(\mathbf{v}_{air}\right)\left(\frac{Cp_{mix}^{0.33}}{Cp_{air}^{0.33}}\right) \quad (6.29)$$

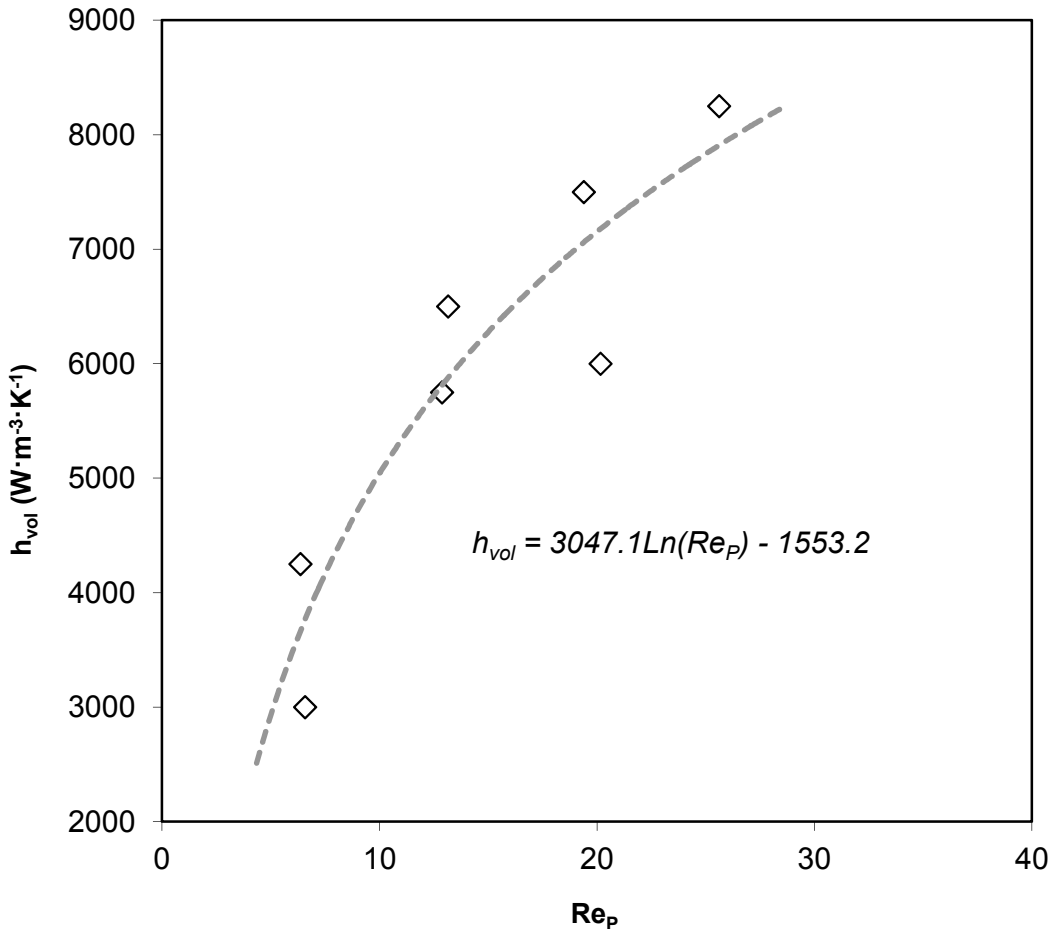

Figure 71: A simple correlation of experimental h_{vol} for air-cooled 40 ppi anodized foams across a range of pore-scale Reynolds numbers.

6.5 Solution Method

The governing equations along with the boundary conditions, were solved using COMSOL. The UMFPACK linear direct numerical solver is used on an 842-node domain composed of three sub-domains as described in Figure 70 on Page 114.

6.6 Model Predictions

Example results of the model predictions are shown in Figure 72. As the model does not account for mixing due to the tortuous path of gases through the monolith, the model captures the spatial dependence of species concentration and temperature distribution throughout the

reaction domain as a function of (Darcian) momentum transport, mass and heat transport. In Figure 73 the impact of local velocity changes and gas-composition on h_{vol} is apparent. In Figure 74 the impact of forcing a uniform value of h_{vol} on the maximum monolith temperature (reaction side) is reported. This type of sensitivity prediction is critically important for the design of reactors based on aluminium substrates where melting temperatures approaching 900 K will lead to material failure. In Figure 75 the impact of forcing a uniform value of h_{vol} on the total yield of hydrogen in the steam-reforming chamber is (modestly) sensitive to the convective heat transfer effects of the catalyst support. As h_{vol} decreases, the steady-state surface temperature of the monolith at any given point increases (and the local reaction rate for the endothermic steam reforming process rises). This model result demonstrates that the thermal distribution of the reactor is sensitive to the catalyst coating and that the impact of coating on h_{vol} is an important design parameter (it could be a critically important consideration for aluminium-foam reactors using a catalyst operating close to the temperature limits for an aluminium monolith). In an optimized non-isothermal model, it is clear that the shape/conformity of the reactor would be used to accomplish temperature distribution and yield targets – design that would not be available without the scalable parameter, h_{vol}.

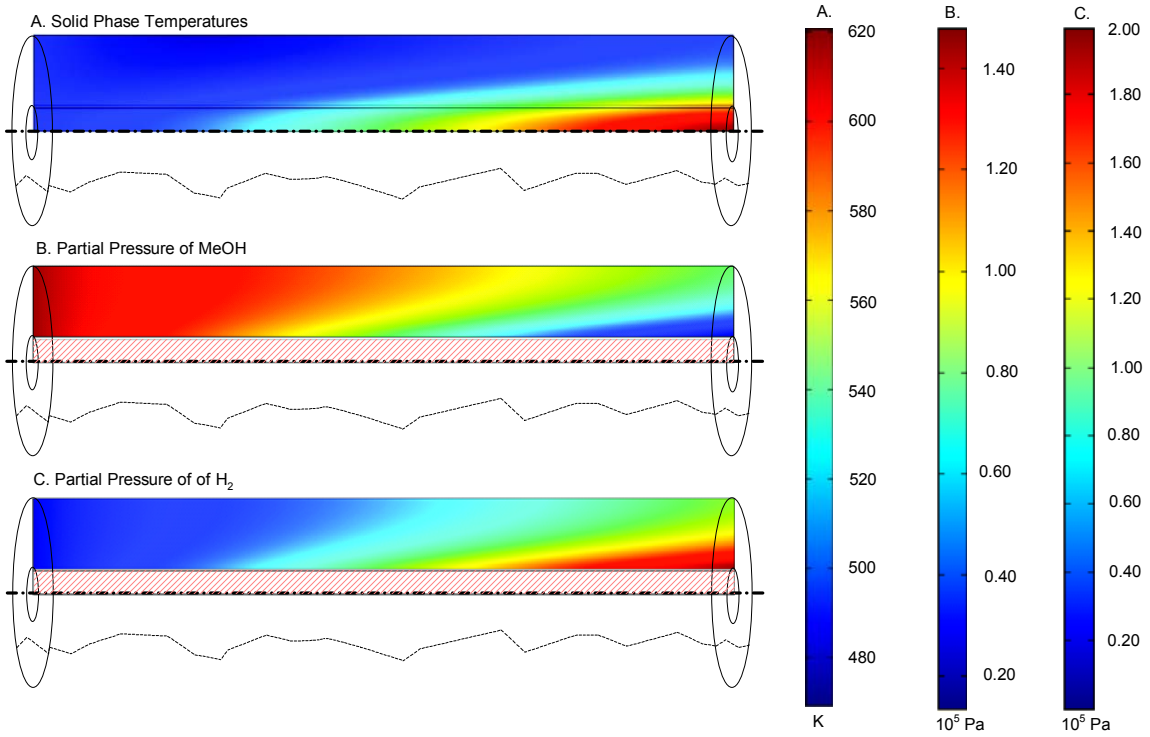

Figure 72: Sample physical values from model CH18HC coated aluminium monolith reactor running at with a 50-50 feed of MeOH and H2O at 300 kPa and a pressure drop of 5 Pa.

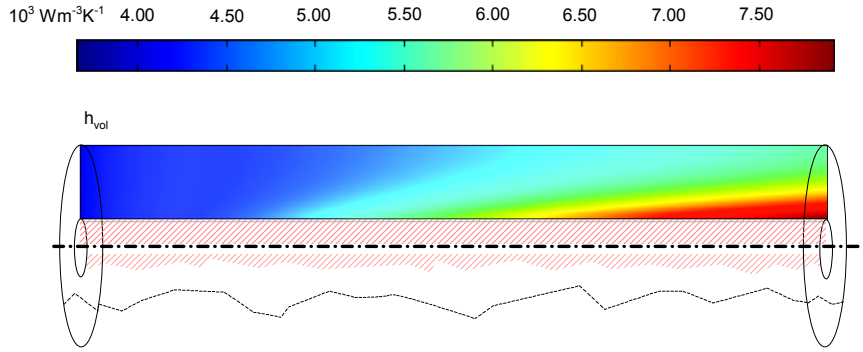

Figure 73: Distribution of values for the volumetric heat transfer coefficient throughout the reactive monolith.

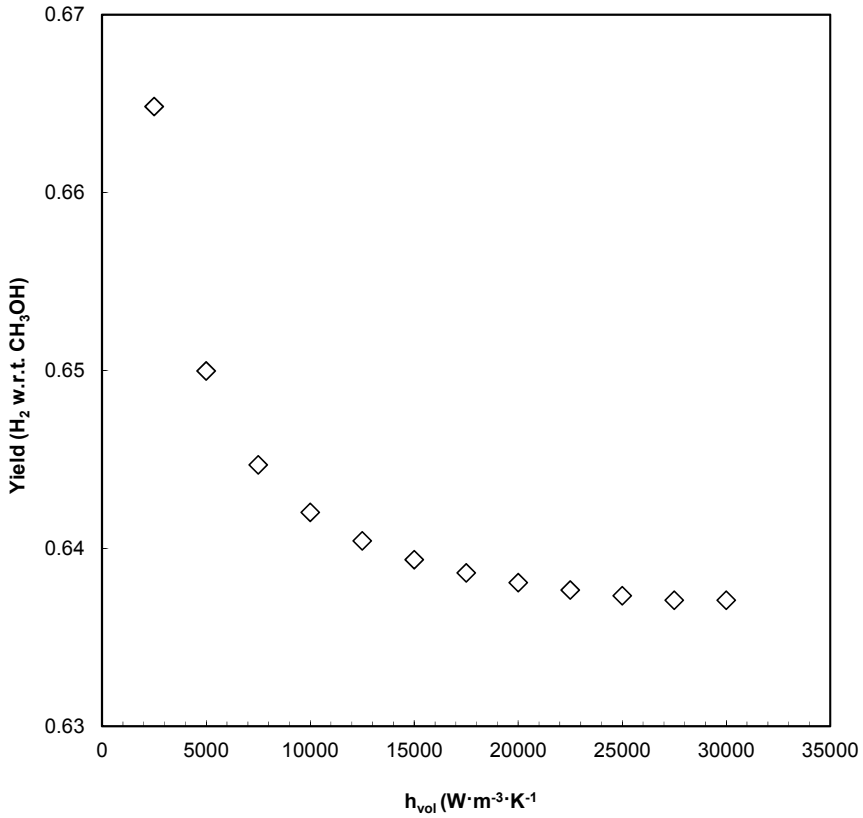

Figure 74: Maximum monolith temperature (x=L, y=h2 as per Figure 70) in the simulated reactor at varied "forced" values of the convective exchange coefficient, h_{vol}

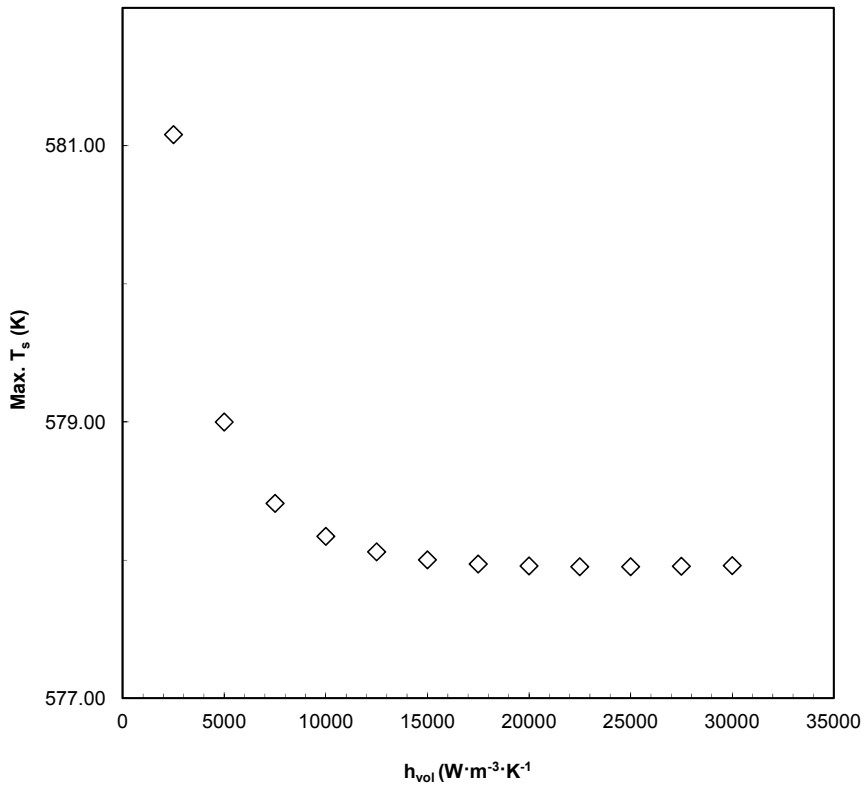

Figure 75: Yields of hydrogen from methanol feedstock in the simulated reactor at varied "forced" values of the convective exchange coefficient, h_{vol}

The conversion rates noted in this model are low as a consequence of the comparatively low amount of catalyst loading that is feasible on a typical metal foam (assuming that the comparative effectiveness factor, η, is unity). However, the ability to model a spatially distributed convective heat exchange coefficient (as in Figure 73) is a very important consideration for non-isothermal reactor systems where the local heat capacity of the fluid stream will be sensitive to the mass transfer rate.

Chapter 7: Conclusions and Recommendations

This work was performed to assess the heat, momentum and mass-transport effects of coating an open cell aluminium foam with a suitable catalyst support, with particular attention to the impact on convective interstitial transport between the fluid and solid phases of a monolith system. The determination of h_{vol} in the coated-foam system was motivated by design requirements for a reactive system, particularly a non-isothermal methanol steam reformer heat-coupled to a combustion chamber such that it would be possible to physically separate highly exothermic processes from highly endothermic processes and still accomplish net-autothermal process regimes. In order to recover h_{vol} at Reynolds numbers that are suitable for reactor systems, a novel steady-state experiment for bare monoliths as well as coated monoliths was designed to operate at low-flow conditions. To the author's knowledge, no scalable experimentation has been previously performed to assess the impact on h_{vol} of adding catalyst support to a metal foam monolith. No comparable work in metal foam has been previously tailored to low-flow regimes consistent with the use of metal foam substrates in "slow-kinetics" chemical process designs. This work proposed a surface-weighted dimensionless efficiency parameter for coated monoliths, $\xi_{\dot{Q}}$, which considers the pump/blower performance, convective/conductive transport balance and the specific area available for heterocatalyst support.

An experimental system was developed to recover suitable physical parameters for momentum transport, conductive heat transfer and subsequently, convective heat transport. Three experimental apparatuses were designed, built and used to determine the value of momentum and heat transfer parameters K, C_F, k_{eff}, required to isolate h_{vol} based on observation of an experimental forced-convection system assessed against a model prediction of temperature profiles of the system at steady-state. Two of the three apparatuses were novel prototypes: 1) The experiment to deduce k_{eff} included a minor improvement in the chosen thermal observations used

to allow the user to validate self-consistency of flux within 4130 steel controls, as illustrated in Figure 33 on Page 67 of this work. 2) The forced convection experiment described in this work is the first conjugate model-fitted steady-state experiment capable of recovering a fully scalable convection coefficient, h_{vol}. This system has the advantage of avoiding spatially dependent dynamic mixing interferences that may occure in non-steady-state systems that have previously been used to determine scalable values of h_{vol}. This experiment also obviates the need to treat entrance/exit thermal profiles as a model artifact rather than an experimental observation.

The permeability, K, of metal foam monoliths in this work ranged between 2.7 and 9.1×10^{-8} m^2 and decreased very slightly with a 76-micron catalyst-support coating and substantially with decreasing average pore size. The friction factor, C_F, was not significantly affected by catalyst coating but increased substantially with decreasing average pore size, but was slightly elevated at low-flow conditions vs. high-flow conditions reported in the literature.

The effective thermal conductivities, k_{eff}, of the metal foams under test ranged between 7 and 9 $W{\cdot}m^{-1}{\cdot}K^{-1}$ and were a strong function of the relative density of the foam under test. The manufacturer's correlation was determined to be a reliable source of thermal conductivity data for subsequent testing.

A thin layer of alumina coating on a metal-foam monolith decreased its solid-fluid interstitial convection coefficient, h_{vol}, relative to an uncoated monolith, and decreased its area-weighted efficiency of convective heat transfer, $\xi_{\dot{Q}}$, relative to an uncoated monolith in forced convection regimes ranging from $Re_C = 100$ to $Re_C = 1,700$ where values of h_{vol} ranged from 2,750 to 20,000 $W{\cdot}m^{-3}{\cdot}K^{-1}$.

The values of h_{vol} recovered in this work are much more scalable than steady-state wall-convection coefficients reported in existing literature and are comparable, at the pore scale, to results recovered from non-steady-state experiments conducted at higher bulk flow rates. The

recovered values of h_{vol} for a foam of given physical parameters were correlated as a strong function of the pore-scale Reynolds number for subsequent modelling in a non-isobaric, non-isothermal reactor system.

Model predictions of the observed effects of catalyst coating on a reactive monolith show that the local value of volumetric heat transfer, h_{vol}, impacts the thermal distribution within the reactor system as well as reactor yields. For the conditions considered in Chapter 6 the impact is minor and h_{vol} would not be a significant consideration for design purposes in the modelled feeds, temperature and pressure regime. The value of h_{vol} is most likely to have significance where local temperature variations are slightly below (or above) critical thermal kinetic barriers (i.e., activation energies). In such cases, the impact of h_{vol} may be quite significant.

Further studies using the described methodology of this work should strive to more precisely characterize momentum transport wall-boundary phenomena in order to improve the reliability of fitting experimental to model data. It is apparent that the counter-axial fluid-momentum distribution at the chosen foam scales is not uniform (as per a perfect plug flow). An improved empirical momentum relationship that can capture more complex boundary effects is desirable. Improvements to the momentum transport model could be accompanied by: 1) Scaling the experiment (dimensions of the monolith and flow conditions) such that wall-boundary effects will have minimal impact on the recovered value of h_{vol}. In such a case it would be sensible to convert the governing equations and boundary conditions for momentum and heat transfer to their dimensionless forms to facilitate interrogation of modelled scale effects on the system. 2) Choosing an empirical modelling method that will describe more fully the boundary effects on fluid momentum transport (coupled with heat transport) – Brinkmann, $k-\varepsilon$ turbulence models or uncoupled Lattice Boltzmann approximations of momentum transport may be more efficient at capturing this information.

References

1. Cybulski, A. and J.A. Moulijn, *Structured Catalysts and Reactors*, in *Unconventional Catalysts for Gas-Phase Reactions*. 1998, CRC Press. p. 179-193.

2. Heck, R., S. Gulati, and J. Farrauto, *The applicaiton of monoliths for gas phase catalytic reactions*. Chemical Engineering Journal, 2001. **82**: p. 149-156.

3. Horny, C., A. Kiwi-Minsker, and A. Renken, *Micro-structured string-reactor for autothermal production of hydrogen.* Chemical Engineering Journal, 2004. **101**(1-3): p. 3-9.

4. Tonkovich, A., et al., *Microchannel reactors for fuel processing applications. I. Water gas shift reactor.* Chemical Engineering Science, 1999. **54**: p. 2947-2951.

5. Yang, K.S., J.S. Choi, and J.S. Chung, *Evaluation of wire-mesh honeycomb containing porous Al/Al2O3 layer for catalytic combustion of ethyl acetate in air.* Catalysis Today, 2004. **97**: p. 159-165.

6. Nijhuis, T., et al., *Preparation of monolithic catalysts.* Catalysis Reviews, 2002. **43**(4): p. 345-380.

7. *Duocel aluminium foam - product specification brochure*. 2005, ERG Aerospace Corporation. p. 4.

8. Tian, et al., *On the thermal performance of wire-screen meshes as heat exchanger material.* International Journal of Heat and Mass Transfer, 2007. **50**: p. 1141–1154.

9. Ahlstrom-Silversand, A.F. and C.U.I. Odenbrand, *Modelling catalytic combustion of carbon monoxide and hydrocarbons over catalytically active wire meshes.* Chemical Engineering Journal, 1999. **73**: p. 205-216.

10. Flytzani-Stephanopoulos, M., G. Voecks, and T. Charng, *Modelling of heat transfer in non-adiabatic monolith reactors and experimental comparisons of metal monoliths with packed beds.* Chemical Engineering Science, 1986. **41**(5): p. 1203-1212.

11. Giani, L., et al., *Washcoating method for Pd/γ-Al2O3 deposition on metallic foams.* Applied Catalysis B, 2006. **62**: p. 121-131.

12. Giani, L., G. Groppi, and E. Tronconi, *Mass-transfer characterization of metallic foams as supports for structured catalysts.* Ind. Eng. Chem. Res., 2005. **44**: p. 4993-5002.

13. Giroux, T., et al., *Monolithic structures as alternatives to particulate catalysts for the reforming of hydrocarbons for hydrogen generation.* Applied Catalysis B: Environmental, 2005. **56**(1-2): p. 95-110.

14. Ismagilov, Z.R., et al., *A catalytic heat-exchanging tubular reactor for combining of high temperature exothermic and endothermic reactions.* Chemical Engineering Journal, 2001. **82**: p. 355-360.

15. Korurtakis, K., et al., *Reticulated ceramic foam catalysts for synthesis gas production*, in *US6630078*. 2003.

16. Pestryakov, A.N., et al., *Foam metal catalysts with inermediate support for deep oxidation of hydrocarbons.* React. Kinet. Catal. Lett., 1994. **53**(2): p. 347-352.

17. Pestryakov, A.N., E.N. Yurchenko, and A.E. Feofilov, *Foam -metal catalysts for purification of waste gases and neutralization of automotive emissions.* Catalysis Today, 1996. **29**: p. 67-70.

18. Tian, J., et al., *The effects of topology upon fluid flow and heat-transfer within celluar copper structures.* International Journal of Heat and Mass Transfer, 2004. **47**: p. 3171-3186.

19. Boomsma, K. and D. Poulikakos, *On the effective thermal conductiity of a three-dimensionally structured fluid-saturated metal foam.* Int. J. Heat Mass Transfer, 2001. **44**: p. 827-836.

20. Babjak, J., V.A. Ettel, and V. Paserin, *Method of forming nickel foam*, in *US4957543*. 1990. p. 1-12.

21. Paserin, V., et al., *CVD technique for Inco nickel foam production.* Advanced Engineering Materials, 2004. **6**(6): p. 454-459.

22. Shi, K., Z. Qian, and M. Zhuang, *Microstructure and properties of sprayed ceramic coatings.* J. Am. Ceram. Soc., 1988. **71**: p. 924-929.

23. Moser, W.R., ed. *Advanced Catalysis and Nanostructured Materials: Modern Synthetic Methods*. 1996, Academic Press: San Deigo. 100-102.

24. Giani, L., et al., *Washcoating method for Pd/γ-Al2O3 deposition on metallic foams.* Applied Catalysis B, 2006: p. 121-131.

25. Ferrari, B., A.J. Sánchez-Herencia, and R. Moreno, *Nickel–alumina graded coatings obtained by dipping and EPD on nickel substrates.* Journal of the European Ceramic Society, 2006. **26**: p. 2205-2212.

26. Wu, X., et al., *Structure and performance of γ-alumina washcoat deposited by plasma spraying* Surface and Coatings Technology, 2001. **145**: p. 226-232.

27. Gal-Or, L., I. Silberman, and R. Chaim, *Electrolytic ZrO2 coatings Part 1: Electrochemical Aspects*. Journal of the Electrochemical Society, 2005. **138**(7): p. 1939-1941.

28. Switzer, J.A., *The n-silicon/thallium(III) oxide heterojunction photoelectrochemical solar cell.* Journal of the Electrochemical Society: Electrochemical Science and Technology, 1986. **133**(4): p. 722-728.

29. Konno, H., et al., *Electrochemical formation of A-site substituted perovskite structure La1-xMxCrO3 oxide coatings*. Electrochimica Acta, 2001. **37**(13): p. 2421-2426.

30. Habazaki, H., et al., *The incorporation and mobility of chromium species in anodic alumina films.* Corrosion Science, 1997. **39**(4): p. 719-730.

31. Suzuki, Y., J. Saito, and N. Kasagi, *Development of micro catalytic combustor with Pt/Al`2O`3 thin films.* JSME international journal. Ser. B, 2004. **47**(3): p. 522-527.

32. Sungkono, I.E., H. Kameyama, and T. Koya, *Development of catalytic combustion technology of VOC materials by anodic oxidation catalyst.* Applied Surface Science, 1997. **121-122**: p. 425-428.

33. Spieker, W.A. and J.R. Regalbuto, *A fundamental model of platinum impregnation onto alumina.* Chemical Engineering Science, 2001. **56**: p. 3491-3504.

34. Sadykov, V.A., et al., *Oxidative dehydrogenation of propane over monoliths at short contact times*. Catalysis Today, 2000. **61**: p. 93-99.

35. Suzuki, Y., J. Saito, and N. Kasagi, *Development of micro catalytic combustor with Pt/Al2O3 thin films*. JSME International Journal. Ser. B, 2004. **47**(3): p. 522-527.

36. Gibson, L. and M. Ashby, *Cellular Solids: Structure and Properties*. Cambridge Solid State Science. 1997: Cambridge University Press.

37. Weaire, D.L., ed. *The Kelvin problem: foam structures of minimal surface area*. 1997, CRC Press. 173.

38. Thomson, S., *On the division of space with minimal partitional area.* Philos. Mag., 1887. **5**: p. 645–654.

39. Weaire, D., *Foam physics.* Advanced Engineering Materials, 2002. **4**(10): p. 723-725.

40. Ashby, M.F., H. Shercliff, and D. Cebon, *Materials- engineering science processing and design.* Butterworth-Heinemann, 2007: p. 71.

41. Boomsma, K., *Metal foams as compact high performance heat exchangers.* Mechanics of Materials, 2003. **35**(12): p. 1161-1176.

42. ERG, *Duocelff aluminium foam - product specification brochure.* Marketing material: p. 4.

43. Queheillalt, D., *Synthesis of stochastic open cell Ni-based foams.* Scripta Materialia, 2004. **50**(3): p. 313-317.

44. Leong, K.C. and L.W. Jin, *Characteristics of oscillating flow through a channel filled with open-cell metal foam.* International Journal of Heat and Fluid Flow, 2006. **27**: p. 144-153.

45. Bhattacharya, Calmidi, and Mahajan, *Thermophysical properties of high porosity metal foams.* International Journal of Heat and Mass Transfer, 2002. **45** p. 1017-1031.

46. Antohe, B., et al., *Experimental determination of permeability and inertia coefficients of mechanically compressed aluminum porous matrices.* Journal of Fluids Engineering, 1997. **119**: p. 404-412.

47. Alvarez-Hernandez, A.R., *Combined flow and heat transfer characterization of open cell aluminum foams*, in *Thesis (M.Sc.)*. 2005, University of Puerto Rico. p. 107.

48. Boomsma, K. and D. Poulikakos, *The effects of compression and pore size variations on the liquid flow characteristics in metal foams.* Journal of Fluids Engineering, 2002. **124**(March): p. 263-272.

49. Calmidi, V.V. and R.L. Mahajan, *Forced Convection in High Porosity Metal Foams.* Journal of Heat Transfer, 2000. **122**(August): p. 557-565.

50. Dukhan, N., *Correlations for the pressure drop for flow through metal foam.* Experiments in Fluids, 2006. **41**: p. 665-672.

51. Dukhan, N. and K.C. Chen, *Heat transfer measurements in metal foam subjected to constant heat flux.* Experimental Thermal and Fluid Science, 2007. **32**: p. 624-631.

52. Hwang, J., et al., *Measurement of intersitial convective heat transfer and frictional drag for flow across metal foams.* Journal of Heat Transfer, 2002. **124**: p. 120-129.

53. Paek, J., et al., *Effective thermal conductivity and permeability of aluminum foam materials.* International Journal of Thermophysics, 2000. **2**: p. 453-464.

54. Salas, K.I. and A.M. Waas, *Convective heat transfer in open cell metal foams.* Journal of Heat Transfer, 2007. **129**: p. 1217-1229.

55. Tian, J., et al., *The effects of topology upon fluid-flow and heat-transfer within cellular copper structures.* International Journal of Heat and Mass Transfer, 2004. **47**(14-16): p. 3171-3186.

56. Kaviany, M., *Principles of heat transfer in porous media, 2nd Edition.* Springer Mechanical Engineering Series, 1995: p. 709.

57. Hwang, J.-J., et al., *Measurement of intersitial convective heat transfer and frictional drag for flow across metal foams.* Journal of Heat Transfer, 2002. **124**: p. 120-129.

58. Vafai, K. and C.L. Tien, *Boundary and inertia Effects on flow and heat transfer in porous media.* Int. J. Heat Mass Transfer, 1981. **24**: p. 195-203.

59. Cheng, P. and C. Hsu, *Thermal dispersion in a porous medium.* International Journal of Heat and Mass Transfer, 1990. **33**(8): p. 1587-1597.

60. Nithiarasu, P., K.N. Seetharamu, and T. Sundararajan, *Natural convective heat transfer in a fluid saturated variable porosity medium.* International Journal of Heat and Mass Transfer, 1997. **40**(16): p. 3955-3967.

61. Tadd, A., B. Gould, and J. Schwank, *Packed bed versus microreactor performance in autothermal reforming of isooctane.* Catalysis Today, 2005. **110**: p. 68-75.

62. Zumbrunnen, D.A., R. Viskanta, and F.P. Incropera, *Heat transfer through porous solids with complex internal geometries*. International Journal of Heat and Mass Transfer, 1996. **29**(2): p. 275-284.

63. Lu, T.J., H.A. Stone, and M.F. Ashby, *Heat transfer in open cell metal foams*. Acta mater., 1998. **46**(10): p. 3619-3635.

64. Tzeng, S. and T. Jeng, *Convective heat transfer in porous channels with 90-deg turned flow.* International Journal of Heat and Mass Transfer, 2006. **49**(7-8): p. 1452-1461.

65. Fuller, et al., *Measurement and interpretation of the heat transfer coefficients of metal foams* Journal of Mechanical Engineering Science 2005. **219**(Proc. IMechE. Part C): p. 183-191.

66. Paek, J.W., et al., *Effective thermal conductivity and permeability of aluminum foam materials*. International Journal of Thermophysics, 2000. **2**: p. 453-464.

67. Collishaw and Evans, *An assessment of expressions for the apparent thermal conductivity of cellular materials.* Journal of Materials Science, 1994. **29**: p. 486-498

68. Guo, Z., *Lattice Boltzmann model for incompressible flows through porous media*. Phys. Rev. E, 2002. **66**(3): p. 9.

69. Dukhan, N., et al., *One-dimensional heat transfer analysis in open-cell 10-ppi metal foam.* International Journal of Heat and Mass Transfer, 2005. **48**: p. 5112-5120.

70. Dukhan, N., R. Picon-Feliciano, and A. Alvarez-Hernandez, *Heat transfer analysis in metal foams with low-conductivity fluids.* Journal of Heat Transfer, 2006. **128**(August): p. 784-792.

71. Angirasa, D., *Forced convective heat transfer in metallic fibrous materials.* Journal of Heat Transfer, 2002. **124**(August): p. 739-745.

72. Kim, T., et al., *Convective heat dissipation with lattice-frame materials.* Mechanics of Materials, 2004. **36**(8): p. 767-780.

73. Morini, G., *Single-phase convective heat transfer in microchannels: a review of experimental results*. International Journal of Thermal Sciences, 2004. **43**(7): p. 631-651.

74. Wen, T., et al., *Forced convection in metallic honeycomb structures.* International Journal of Heat and Mass Transfer, 2006. **49**(19-20): p. 3313-3324.

75. Tian, Wen, and Lu, *Forced convection in metallic honeycomb structures* Int. J. Heat Mass Transfer, 2006. **49**: p. 3313-3324.

76. Moffat, R., J. Eaton, and A. Onstad, *A Method for Determining the Heat Transfer Properties of Foam-Fins*. Journal of Heat Transfer, 2009. **131**(011603).

77. Younis, L.B. and R. Viskanta, *Experimental determination of the volumetric heat transfer coefficient between stream of air and ceramic foam.* International Journal of Heat and Mass Transfer, 1993. **36**(6): p. 1425-1434.

78. Golombok, Jariwala, and Shirvill, *Gas-solid heat exchange in a fibrous metallic material measured by a heat regenerator technique.* International Journal of Heat and Mass Transfer, 1990. **33**(2): p. 243-252.

79. Jeng, T.-M., L.-K. Liu, and Y.-H. Hung, *A novel semi-empirical model for evaluating thermal performance of porous metallic foam heat sinks.* Journal of Electronic Packaging, 2005. **127**(September): p. 223-234.

80. Amao, A., *Mathematical model for Darcy Forchheimer flow with applications to well performance analysis*. Masters Thesis - Texas Tech, 2007.

81. Jamiolahmady, M., et al., *Flow around a rock perforation surrounded by crushed zone: Experiments vs. theory*. Journal of Petroleum Science and Engineering, 2006. **50**: p. 102-114.

82. Aulisa, E., et al. *Mathematical frame-work for productivity index of the well for fast Forchheimer (non-Darcy) flow in porous media*. in *Proceedings of the COMSOL Users Conference*. 2006. Boston: COMSOL Inc.

83. Harris, D.C., *Quantitative Chemical Analysis*. 6th ed. 2003, New York: W. H. Freeman and Company.

84. Dixon, W.J. and R.B. Dean, *Simplified statistics for small numbers of observations.* Anal. Chem., 1951. **23** (4): p. 636–638.

85. Rorabacher, D.B., *Statistical treatment for rejection of deviant values: critical values of Dixon Q parameter and related subrange ratios at the 95 percent confidence level.* Anal. Chem., 1991. **63**(2): p. 139–146.

86. ERG, *Duocelff aluminium foam - product specification brochure*. 2005. p. 4.

87. Tsotsas, E., M. Winterberg, and A. Krischke, *A simple and coherent set of coefficients for modelling of heat and mass transport with and without chemical reaction in tubes filled with spheres.* Chemical Engineering Science, 2000. **55**: p. 967-979.

88. Kaviany, M., *Principles of heat transfer in porous media, 2nd Edition*. Springer Mechanical Engineering Series. 1995: Springer. 709.

89. Park, H., et al., *Methanol steam reformer on a silicon wafer*. Journal of Microelectromechanical Systems, 2006. **15**(4): p. 976-985.

90. Amphlett, J., et al., *Hydrogen production by steam reforming of methanol for polymer electrolyte fuel cells*. International Journal of Hydrogen Energy, 1994. **19**(2): p. 131-137.

91. Thurgood, et al., *A comparison between ceramic foam catalyst and packed-beds for methanol steam reforming*, in *A.I.Ch.E National Meeting*. 2005: Cincinnati. p. 1-12.

92. Fenghour, A., W. Wakeham, and V. Vesovic, *The viscosity of carbon dioxide.* Journal of Physical and Chemical Reference Data, 1998. **27**(1): p. 31-44.

93. Teske, V. and E. Vogel, *Viscosity Measurements on Methanol Vapor and Their Evaluation.* J. Chem. Eng. Data, 2006. **51**: p. 628-635.

94. Xiang, H., A. Laesecke, and M. Huber, *A new reference correlation for the viscosity of methanol.* Journal of Physical and Chemical Reference Data, 2006. **34**(5): p. 1597-1620.

95. Incropera, F., *Fundamentals of Heat and Mass Transfer*. 2002, New York: Wiley.

96. Watanabe, M., M. Uchida, and S. Motoo, *Preparation of highly dispersed Pt + Ru alloy clusters and the activity for the electrooxidation of methanol.* J. Electroanal. Chem., 1987. **229**: p. 395-406.

97. Pfrengle, A., et al., *Electrophoretic deposition and sintering of zirconia layers on microstructured steel substrates.* Journal of the European Ceramic Society, 2006. **26**(13): p. 2633-2638.

98. Lankin, M. and K. Karan, *Fabrication of thin-layer electrolytes for solid oxide fuel cell applications by electrophoretic deposition (EPD)*, in *Thesis (MSc.)*. 2006, Queen's University.

99. Sulka, G.D., et al., *Synthesis of well-ordered alumina nanopores by anodizing aluminum foils in sulfuric acid.* J. of the Electrochem. Soc., 2002. **149**(7): p. D97-D103.

100. Parsons, B., *Catalyst coated micro-structured reactor monoliths*, in *Thesis (BSc.Eng.)* 2007, Queen's University.

101. Imamura, S., et al., *Decomposition of methanol on Pt-loaded ceria.* Catalysis Today, 1999. **50**(2): p. 369-380.

Appendix A:
A Finite-Element Routine for Fitting h_{vol} to Experimental Data

COMSOL Script (in MATLAB) of Heat Transfer Model Fitting of Experimental Data

(with statistical records of model vs. experimental data)

This model is based on the boundary conditions and governing equations in Chapter 3:

```
% COMSOL Multiphysics Model M-file
% Generated by COMSOL 3.2


%preliminary stuff

AirTempStorage=[];
FoamTempStorage=[];
SSEStorage=[];
vhvolStorage=[];
RSquareStorage=[];
minSSEindex=[];

%Loop through each experiment
for trialx=[1:1:51];

inletfit=polyfit([coeffs(12,trialx) coeffs(13,trialx) coeffs(14,trialx)],[[coeffs(16,trialx)
coeffs(17,trialx) coeffs(18,trialx)]],2);

% Local (inside the loop) storage of SSE
SSETemp=[];


% hvol increments loop
for vhvol=[250:250:20000]


flclear fem

% COMSOL version
clear vrsn
vrsn.name = 'COMSOL 3.2';
vrsn.ext = '';
vrsn.major = 0;
vrsn.build = 222;
vrsn.rcs = '$Name:  $';
vrsn.date = '$Date: 2005/09/01 18:02:30 $';
fem.version = vrsn;

% Geometry
g1=rect2('0.052','0.0127','base','corner','pos',–'0','0'″,'rot','0');
g2=rect2('0.052','0.0015875','base','corner','pos',–'0','-0.0015875'″,'rot','0');
clear s
```

```
s.objs=–g1,g2″;
s.name=–'R1','R2'″;
s.tags=–'g1','g2'″;

fem.draw=struct('s',s);
fem.geom=geomcsg(fem);

% Initialize mesh
fem.mesh=meshinit(fem);

% (Default values are not included)

% Application mode 1
clear appl
appl.mode.class = 'FlConvCond';
appl.assignsuffix = '˙cc';
clear prop
prop.analysis='static';
appl.prop = prop;
clear bnd
bnd.type = –'q0','cont','T','T','q','T'″;%last T was a q
bnd.T0 = –0,0,'Tfoamin','Tcopperin',0,'Tcopperout'″;
bnd.q0 = –0,0,0,0,'bottomflux',0″;
bnd.ind = [4,5,3,2,1,6,6];
appl.bnd = bnd;
clear equ
equ.k = –388,'kfoam'″;
equ.init = –0,'Tcopperin'″;%changed from (0,350)
equ.rho = –8700,'rhofoam'″;
equ.C = –385,'Cpfoam'″;
equ.Q = –0,'convect'″;
equ.ind = [1,2];
appl.equ = equ;
fem.appl–1″ = appl;

% Application mode 2
clear appl
appl.mode.class = 'FlConvCond';
appl.dim = –'T2'″;
appl.name = 'cc2';
appl.assignsuffix = '˙cc2';
clear prop
prop.analysis='static';
clear weakconstr
weakconstr.value = 'off';
weakconstr.dim = –'lm2'″;
prop.weakconstr = weakconstr;
appl.prop = prop;
clear bnd
bnd.type = –'cont','q0','T','qc'″;
bnd.T0 = –0,0,'Tairin',0″;
bnd.ind = [1,1,3,2,2,1,4];
appl.bnd = bnd;
clear equ
equ.k = –0.025,'kair'″;
equ.init = –0,'Tairin'″;%changed from (0,250)
```

```
equ.rho = –1.205,'rhoair'″;
equ.C = –1006,'Cpair'″;
equ.Q = –0,'airconvect'″;
equ.v = –0,'vely'″;
equ.u = –0,'velx'″;
equ.usage = –0,1″;
equ.ind = [1,2];
appl.equ = equ;
fem.appl–2″ = appl;

% Application mode 3
clear appl
appl.mode.class = 'FlPDEC';
appl.dim = –'p','p˙t'″;
appl.name = 'PDE';
appl.shape = –'shlag(2,''p'')','shlag(2,''lm3'')'″;
appl.gporder = –4,4″;
appl.assignsuffix = ''PDE';
clear prop
clear weakconstr
weakconstr.value = 'off';%changed from ideal
weakconstr.dim = –'lm3','lm4'″;
prop.weakconstr = weakconstr;
appl.prop = prop;
clear pnt
pnt.wcshape = 2;
pnt.ind = [1,1,1,1,1,1];
appl.pnt = pnt;
clear bnd
bnd.r = –0,0,'pin','pout'″;
bnd.type = –'dir','neu','dir','dir'″;
bnd.wcgporder = 2;
bnd.wcshape = 2;
bnd.ind = [1,1,3,2,2,1,4];
appl.bnd = bnd;
clear equ
equ.init = –0,–100000;0″″;
equ.wcgporder = 2;
equ.shape = 1;
equ.c = –1,'funcv*rhoair'″;
equ.wcshape = 2;
equ.da = –1,0″;
equ.f = –1,0″;
equ.usage = –0,1″;
equ.dinit = –0,–100;0″″;
equ.ind = [1,2];
appl.equ = equ;
fem.appl–3″ = appl;
fem.border = 1;
fem.outform = 'general';
fem.units = 'SI';

% Global expressions
fem.expr = –'funcv','2/((muair/K)+((muair/K)^2+4*Forch*rhoairlocal*absgradP)^0.5)', ...
  'rhoair','epsilon*p*28.8e-3/8.314/T2', ...
  'muair','(-7.887E-12*T2^2+4.427E-08*T2+5.204E-06)', ...
```

```
  'K',coeffs(54,trialx), ...
  'absgradP','(px^2+py^2)^0.5', ...
  'Forch',coeffs(53,trialx), ...
  'convect','hvol*(T2-T)', ...
  'airconvect','hvol*(T-T2)', ...
  'kair','10^(0.8616*log10(abs(T2))-3.7142)', ...
  'Cpair','0.0769*T2+1076.9', ...
  'funcDF','(2*(K/muair))/(1+(1+4*Forch*rhoairlocal*(K/muair)^2*absgradP)^0.5)', ...
  'velx','-funcv*px', ...
  'vely','-funcv*py', ...
  'hvol',vhvol, ...
  'epsilon',1-coeffs(11,trialx), ...
  'rhoairlocal','p*28.8e-3/8.314/T2', ...
  'Tairin',coeffs(42,trialx), ...
  'Tairout',coeffs(43,trialx), ...
  'Tfoamin','inletfit1*y^2+inletfit2*y+inletfit3', ...
  'Tfoamout',coeffs(41,trialx), ...
  'Tcopperin',coeffs(40,trialx), ...
  'Tcopperout',coeffs(41,trialx), ...
  'kfoam',coeffs(44,trialx), ...
  'rhofoam',coeffs(45,trialx), ...
  'Cpfoam',coeffs(46,trialx), ...
  'pin',coeffs(49,trialx), ...
  'pout',coeffs(50,trialx), ...
  'bottomflux',coeffs(52,trialx), ...
  'inletfit1',inletfit(1), ...
  'inletfit2',inletfit(2), ...
  'inletfit3',inletfit(3)";


%inletfit(1)*'y'^2+inletfit(2)*'y'+inletfit(3) is the expression I want to
%use for Tfoamin


% Multiphysics
fem=multiphysics(fem);

% Extend mesh
fem.xmesh=meshextend(fem);

% Solve problem
fem.sol=femnlin(fem, ...
              'solcomp',–'T','p','T2'", ...
              'outcomp',–'T','p','T2'");

% fem.sol=femnlin(fem, ...
%               'solcomp',–'lm3','T','p','T2'", ...
%               'outcomp',–'lm3','T','p','T2'");

% Save current fem structure for restart purposes
fem0=fem;

%Collect output data
xcoordinates=[0 0.001   0.002   0.003   0.004   0.005   0.006   0.007   0.008   0.009   0.01
        0.011   0.012   0.013   0.014   0.015   0.016   0.017   0.018   0.019   0.02    0.021
        0.022   0.023   0.024   0.025   0.026   0.027   0.028   0.029   0.03    0.031   0.032
```

```
        0.033   0.034   0.035   0.036   0.037   0.038   0.039   0.04    0.041   0.042   0.043
        0.044   0.045   0.046   0.047   0.048   0.049   0.05    0.051   0.052];
ycoordinates=[0.0127    0.0127  0.0127  0.0127  0.0127  0.0127  0.0127  0.0127  0.0127  0.0127
        0.0127  0.0127  0.0127  0.0127  0.0127  0.0127  0.0127  0.0127  0.0127  0.0127  0.0127
        0.0127  0.0127  0.0127  0.0127  0.0127  0.0127  0.0127  0.0127  0.0127  0.0127  0.0127
        0.0127  0.0127  0.0127  0.0127  0.0127  0.0127  0.0127  0.0127  0.0127  0.0127  0.0127
        0.0127  0.0127  0.0127  0.0127  0.0127  0.0127  0.0127  0.0127  0.0127  0.0127];



%start gathering statistics
TestSSE=(postinterp(fem,'T2',[0;0.0127])-
coeffs(31,trialx))^2+(postinterp(fem,'T2',[0.0083;0.0127])-
coeffs(32,trialx))^2+(postinterp(fem,'T2',[0.0167;0.0127])-
coeffs(33,trialx))^2+(postinterp(fem,'T2',[0.0225;0.0127])-
coeffs(34,trialx))^2+(postinterp(fem,'T2',[0.0301;0.0127])-
coeffs(35,trialx))^2+(postinterp(fem,'T2',[0.0373;0.0127])-
coeffs(36,trialx))^2+(postinterp(fem,'T2',[0.0437;0.0127])-
coeffs(37,trialx))^2+(postinterp(fem,'T2',[0.0520;0.0127])-coeffs(38,trialx))^2;
MeanExpTair=mean(coeffs([31:38],4));
TestSSR=(postinterp(fem,'T2',[0;0.0127])-
MeanExpTair)^2+(postinterp(fem,'T2',[0.0083;0.0127])-
MeanExpTair)^2+(postinterp(fem,'T2',[0.0167;0.0127])-
MeanExpTair)^2+(postinterp(fem,'T2',[0.0225;0.0127])-
MeanExpTair)^2+(postinterp(fem,'T2',[0.0301;0.0127])-
MeanExpTair)^2+(postinterp(fem,'T2',[0.0373;0.0127])-
MeanExpTair)^2+(postinterp(fem,'T2',[0.0437;0.0127])-
MeanExpTair)^2+(postinterp(fem,'T2',[0.0520;0.0127])-MeanExpTair)^2;
TestSST=(MeanExpTair-coeffs(31,trialx))^2+(MeanExpTair-coeffs(32,trialx))^2+(MeanExpTair-
coeffs(33,trialx))^2+(MeanExpTair-coeffs(34,trialx))^2+(MeanExpTair-
coeffs(35,trialx))^2+(MeanExpTair-coeffs(36,trialx))^2+(MeanExpTair-
coeffs(37,trialx))^2+(MeanExpTair-coeffs(38,trialx))^2;
TestRSquare=TestSSR/TestSST;
TestMSRoMSE=TestSSR/(2-1)/TestSSE/(8-2);  %need to think this through: am I 2 parameters
minus 1 and 8 data points minus 2 parameters?

AirTemp=postinterp(fem,'T2',[xcoordinates;ycoordinates]);
FoamTemp=postinterp(fem,'T',[xcoordinates;ycoordinates]);

vhvolStorage=[vhvolStorage;vhvol];
SSEStorage=[SSEStorage;TestSSE];
RSquareStorage=[RSquareStorage;TestRSquare];

%Local storage
SSETemp=[SSETemp;TestSSE];

AirTempStorage=[AirTempStorage;AirTemp];
FoamTempStorage=[FoamTempStorage;FoamTemp];



end

%Clunky labelling routine
```

```
AirTempStorage=[AirTempStorage;[coeffs(2,trialx) 0 0 0 0 0 0 0 0 0 0 0 0 0 0 0 0 0 0 0 0 0 0 0 0
0 0 0 0 0 0 0 0 0 0 0 0 0 0 0 0 0 0 0 0 0 0 0 0 0 0 0 0]];
FoamTempStorage=[FoamTempStorage;[coeffs(2,trialx) 0 0 0 0 0 0 0 0 0 0 0 0 0 0 0 0 0 0 0 0 0 0
0 0 0 0 0 0 0 0 0 0 0 0 0 0 0 0 0 0 0 0 0 0 0 0 0 0 0 0 0 0]];


SSEStorage=[SSEStorage;coeffs(2,trialx)];
RSquareStorage=[RSquareStorage;coeffs(2,trialx)];

%Tracking the location of the minimum SSE
[minSSE,indexminSSE]=min(SSETemp);
minSSEindex=[minSSEindex;indexminSSE];

%Loop through each experiment
end

%*************************************************************************
%***********************OK, Now to do the Q-Ratio Test on all the data*********
%***************************************************************************


%preliminary stuff

Qstorage=[];

%Loop through each experiment
for trialx=[1:1:51];

inletfit=polyfit([coeffs(12,trialx) coeffs(13,trialx) coeffs(14,trialx)],[[coeffs(16,trialx)
coeffs(17,trialx) coeffs(18,trialx)]],2);


%Pick the correct value of the index
vhvol=vhvolStorage(minSSEindex(trialx));


flclear fem

% COMSOL version
clear vrsn
vrsn.name = 'COMSOL 3.2';
vrsn.ext = '';
vrsn.major = 0;
vrsn.build = 222;
vrsn.rcs = '$Name: $';
vrsn.date = '$Date: 2005/09/01 18:02:30 $';
fem.version = vrsn;

% Geometry
g1=rect2('0.052','0.0127','base','corner','pos',–'0','0'”,'rot','0');
g2=rect2('0.052','0.0015875','base','corner','pos',–'0','-0.0015875'”,'rot','0');
clear s
s.objs=–g1,g2”;
s.name=–'R1','R2'”;
s.tags=–'g1','g2'”;
```

```
fem.draw=struct('s',s);
fem.geom=geomcsg(fem);

% Initialize mesh
fem.mesh=meshinit(fem);

% (Default values are not included)

% Application mode 1
clear appl
appl.mode.class = 'FlConvCond';
appl.assignsuffix = 'cc';
clear prop
prop.analysis='static';
appl.prop = prop;
clear bnd
bnd.type = {'q0','cont','T','T','q','T'};%last T was a q
bnd.T0 = {0,0,'Tfoamin','Tcopperin',0,'Tcopperout'};
bnd.q0 = {0,0,0,0,'bottomflux',0};
bnd.ind = [4,5,3,2,1,6,6];
appl.bnd = bnd;
clear equ
equ.k = {388,'kfoam'};
equ.init = {0,'Tcopperin'};%changed from (0,350)
equ.rho = {8700,'rhofoam'};
equ.C = {385,'Cpfoam'};
equ.Q = {0,'convect'};
equ.ind = [1,2];
appl.equ = equ;
fem.appl{1} = appl;

% Application mode 2
clear appl
appl.mode.class = 'FlConvCond';
appl.dim = {'T2'};
appl.name = 'cc2';
appl.assignsuffix = 'cc2';
clear prop
prop.analysis='static';
clear weakconstr
weakconstr.value = 'off';
weakconstr.dim = {'lm2'};
prop.weakconstr = weakconstr;
appl.prop = prop;
clear bnd
bnd.type = {'cont','q0','T','qc'};
bnd.T0 = {0,0,'Tairin',0};
bnd.ind = [1,1,3,2,2,1,4];
appl.bnd = bnd;
clear equ
equ.k = {0.025,'kair'};
equ.init = {0,'Tairin'};%changed from (0,250)
equ.rho = {1.205,'rhoair'};
equ.C = {1006,'Cpair'};
equ.Q = {0,'airconvect'};
equ.v = {0,'vely'};
```

```
equ.u = –0,'velx'″;
equ.usage = –0,1″;
equ.ind = [1,2];
appl.equ = equ;
fem.appl–2″ = appl;

% Application mode 3
clear appl
appl.mode.class = 'FlPDEC';
appl.dim = –'p','p't'″;
appl.name = 'PDE';
appl.shape = –'shlag(2,''p'')','shlag(2,''lm3'')'″;
appl.gporder = –4,4″;
appl.assignsuffix = ''PDE';
clear prop
clear weakconstr
weakconstr.value = 'off';%changed from ideal
weakconstr.dim = –'lm3','lm4'″;
prop.weakconstr = weakconstr;
appl.prop = prop;
clear pnt
pnt.wcshape = 2;
pnt.ind = [1,1,1,1,1,1];
appl.pnt = pnt;
clear bnd
bnd.r = –0,0,'pin','pout'″;
bnd.type = –'dir','neu','dir','dir'″;
bnd.wcgporder = 2;
bnd.wcshape = 2;
bnd.ind = [1,1,3,2,2,1,4];
appl.bnd = bnd;
clear equ
equ.init = –0,–100000;0″″;
equ.wcgporder = 2;
equ.shape = 1;
equ.c = –1,'funcv*rhoair'″;
equ.wcshape = 2;
equ.da = –1,0″;
equ.f = –1,0″;
equ.usage = –0,1″;
equ.dinit = –0,–100;0″″;
equ.ind = [1,2];
appl.equ = equ;
fem.appl–3″ = appl;
fem.border = 1;
fem.outform = 'general';
fem.units = 'SI';

% Global expressions
fem.expr = –'funcv','2/((muair/K)+((muair/K)^2+4*Forch*rhoairlocal*absgradP)^0.5)', ...
  'rhoair','epsilon*p*28.8e-3/8.314/T2', ...
  'muair','(-7.887E-12*T2^2+4.427E-08*T2+5.204E-06)', ...
  'K',coeffs(54,trialx), ...
  'absgradP','(px^2+py^2)^0.5', ...
  'Forch',coeffs(53,trialx), ...
  'convect','hvol*(T2-T)', ...
```

```
  'airconvect','hvol*(T-T2)', ...
  'kair','10^(0.8616*log10(abs(T2))-3.7142)', ...
  'Cpair','0.0769*T2+1076.9', ...
  'funcDF','(2*(K/muair))/(1+(1+4*Forch*rhoairlocal*(K/muair)^2*absgradP)^0.5)', ...
  'velx','-funcv*px', ...
  'vely','-funcv*py', ...
  'hvol',vhvol, ...
  'epsilon',1-coeffs(11,trialx), ...
  'rhoairlocal','p*28.8e-3/8.314/T2', ...
  'Tairin',coeffs(42,trialx), ...
  'Tairout',coeffs(43,trialx), ...
  'Tfoamin','inletfit1*y^2+inletfit2*y+inletfit3', ...
  'Tfoamout',coeffs(41,trialx), ...
  'Tcopperin',coeffs(40,trialx), ...
  'Tcopperout',coeffs(41,trialx), ...
  'kfoam',coeffs(44,trialx), ...
  'rhofoam',coeffs(45,trialx), ...
  'Cpfoam',coeffs(46,trialx), ...
  'pin',coeffs(49,trialx), ...
  'pout',coeffs(50,trialx), ...
  'bottomflux',coeffs(52,trialx), ...
  'inletfit1',inletfit(1), ...
  'inletfit2',inletfit(2), ...
  'inletfit3',inletfit(3)″;



% Multiphysics
fem=multiphysics(fem);

% Extend mesh
fem.xmesh=meshextend(fem);

% Solve problem
fem.sol=femnlin(fem, ...
              'solcomp',–'T','p','T2'″, ...
              'outcomp',–'T','p','T2'″);

% fem.sol=femnlin(fem, ...
%               'solcomp',–'lm3','T','p','T2'″, ...
%               'outcomp',–'lm3','T','p','T2'″);

% Save current fem structure for restart purposes
fem0=fem;

%Collect output data
xcoordinates=[0 0.001   0.002   0.003   0.004   0.005   0.006   0.007   0.008   0.009   0.01
        0.011   0.012   0.013   0.014   0.015   0.016   0.017   0.018   0.019   0.02    0.021
        0.022   0.023   0.024   0.025   0.026   0.027   0.028   0.029   0.03    0.031   0.032
        0.033   0.034   0.035   0.036   0.037   0.038   0.039   0.04    0.041   0.042   0.043
        0.044   0.045   0.046   0.047   0.048   0.049   0.05    0.051   0.052];
ycoordinates=[0.0127    0.0127  0.0127  0.0127  0.0127  0.0127  0.0127  0.0127  0.0127  0.0127
        0.0127  0.0127  0.0127  0.0127  0.0127  0.0127  0.0127  0.0127  0.0127  0.0127  0.0127
        0.0127  0.0127  0.0127  0.0127  0.0127  0.0127  0.0127  0.0127  0.0127  0.0127  0.0127
        0.0127  0.0127  0.0127  0.0127  0.0127  0.0127  0.0127  0.0127  0.0127  0.0127  0.0127
        0.0127  0.0127  0.0127  0.0127  0.0127  0.0127  0.0127  0.0127  0.0127  0.0127];
```

```
%start gathering statistics

Egap1=abs(postinterp(fem,'T2',[0;0.0127])-coeffs(31,trialx));
Egap2=abs(postinterp(fem,'T2',[0.0083;0.0127])-coeffs(32,trialx));
Egap3=abs(postinterp(fem,'T2',[0.0167;0.0127])-coeffs(33,trialx));
Egap4=abs(postinterp(fem,'T2',[0.0225;0.0127])-coeffs(34,trialx));
Egap5=abs(postinterp(fem,'T2',[0.0301;0.0127])-coeffs(35,trialx));
Egap6=abs(postinterp(fem,'T2',[0.0373;0.0127])-coeffs(36,trialx));
Egap7=abs(postinterp(fem,'T2',[0.0437;0.0127])-coeffs(37,trialx));
Egap8=abs(postinterp(fem,'T2',[0.0520;0.0127])-coeffs(38,trialx));

ErrorStorage=[Egap1 1;Egap2 2;Egap3 3;Egap4 4;Egap5 5;Egap6 6;Egap7 7;Egap8 8];
ErrorStorage=sortrows(ErrorStorage,1);

Q1=0; %assumed to not be in error
Q2=abs(ErrorStorage(2,1)-ErrorStorage(3,1))/range(ErrorStorage(1:8));
Q3=abs(ErrorStorage(3,1)-ErrorStorage(4,1))/range(ErrorStorage(1:8));
Q4=abs(ErrorStorage(4,1)-ErrorStorage(5,1))/range(ErrorStorage(1:8));
Q5=abs(ErrorStorage(5,1)-ErrorStorage(6,1))/range(ErrorStorage(1:8));
Q6=abs(ErrorStorage(6,1)-ErrorStorage(7,1))/range(ErrorStorage(1:8));
Q7=abs(ErrorStorage(7,1)-ErrorStorage(8,1))/range(ErrorStorage(1:8));
Q8=0; %assumed to not be in error

if (Q1¿0.468)
    Qstorage(trialx,ErrorStorage(1,2))=false;
else
   Qstorage(trialx,ErrorStorage(1,2))=true;
end

if (Q2¿0.468)
    Qstorage(trialx,ErrorStorage(2,2))=false;
else
    Qstorage(trialx,ErrorStorage(2,2))=true;
end

if (Q3¿0.468)
    Qstorage(trialx,ErrorStorage(3,2))=false;
else
    Qstorage(trialx,ErrorStorage(3,2))=true;
end

if (Q4¿0.468)
    Qstorage(trialx,ErrorStorage(4,2))=false;
else
    Qstorage(trialx,ErrorStorage(4,2))=true;
end

if (Q5¿0.468)
    Qstorage(trialx,ErrorStorage(5,2))=false;
else
    Qstorage(trialx,ErrorStorage(5,2))=true;
end

if (Q6¿0.468)
```

```
    Qstorage(trialx,ErrorStorage(6,2))=false;
else
    Qstorage(trialx,ErrorStorage(6,2))=true;
end

if (Q7¿0.468)
    Qstorage(trialx,ErrorStorage(7,2))=false;
else
    Qstorage(trialx,ErrorStorage(7,2))=true;
end

if (Q8¿0.468)
    Qstorage(trialx,ErrorStorage(8,2))=false;
else
    Qstorage(trialx,ErrorStorage(8,2))=true;
end



%Loop through each experiment
end


%*************************************************************************
%*********Armed with Q-ratios, recalculate SSE and best-fit models**********
%*************************************************************************

%preliminary stuff

Qfilterederrors=[];

AirTempStorageQ=[];
FoamTempStorageQ=[];
SSEStorageQ=[];
vhvolStorageQ=[];
RSquareStorageQ=[];
minSSEindexQ=[];
MeanExpErrTair=[];


%Loop through each experiment
for trialx=[1:1:51];

inletfit=polyfit([coeffs(12,trialx) coeffs(13,trialx) coeffs(14,trialx)],[[coeffs(16,trialx)
coeffs(17,trialx) coeffs(18,trialx)]],2);

% Local (inside the loop) storage of SSE
SSETemp=[];


% hvol increments loop
for vhvol=[250:250:20000]


flclear fem
```

```
% COMSOL version
clear vrsn
vrsn.name = 'COMSOL 3.2';
vrsn.ext = '';
vrsn.major = 0;
vrsn.build = 222;
vrsn.rcs = '$Name:  $';
vrsn.date = '$Date: 2005/09/01 18:02:30 $';
fem.version = vrsn;

% Geometry
g1=rect2('0.052','0.0127','base','corner','pos',{'0','0'},'rot','0');
g2=rect2('0.052','0.0015875','base','corner','pos',{'0','-0.0015875'},'rot','0');
clear s
s.objs={g1,g2};
s.name={'R1','R2'};
s.tags={'g1','g2'};

fem.draw=struct('s',s);
fem.geom=geomcsg(fem);

% Initialize mesh
fem.mesh=meshinit(fem);

% (Default values are not included)

% Application mode 1
clear appl
appl.mode.class = 'FlConvCond';
appl.assignsuffix = 'cc';
clear prop
prop.analysis='static';
appl.prop = prop;
clear bnd
bnd.type = {'q0','cont','T','T','q','T'};%last T was a q
bnd.T0 = {0,'Tfoamin','Tcopperin',0,'Tcopperout'};
bnd.q0 = {0,0,0,0,'bottomflux',0};
bnd.ind = [4,5,3,2,1,6,6];
appl.bnd = bnd;
clear equ
equ.k = {388,'kfoam'};
equ.init = {0,'Tcopperin'};%changed from (0,350)
equ.rho = {8700,'rhofoam'};
equ.C = {385,'Cpfoam'};
equ.Q = {0,'convect'};
equ.ind = [1,2];
appl.equ = equ;
fem.appl{1} = appl;

% Application mode 2
clear appl
appl.mode.class = 'FlConvCond';
appl.dim = {'T2'};
appl.name = 'cc2';
appl.assignsuffix = 'cc2';
clear prop
```

```
prop.analysis='static';
clear weakconstr
weakconstr.value = 'off';
weakconstr.dim = {'lm2'};
prop.weakconstr = weakconstr;
appl.prop = prop;
clear bnd
bnd.type = {'cont','q0','T','qc'};
bnd.T0 = {0,0,'Tairin',0};
bnd.ind = [1,1,3,2,2,1,4];
appl.bnd = bnd;
clear equ
equ.k = {0.025,'kair'};
equ.init = {0,'Tairin'};%changed from (0,250)
equ.rho = {1.205,'rhoair'};
equ.C = {1006,'Cpair'};
equ.Q = {0,'airconvect'};
equ.v = {0,'vely'};
equ.u = {0,'velx'};
equ.usage = {0,1};
equ.ind = [1,2];
appl.equ = equ;
fem.appl{2} = appl;

% Application mode 3
clear appl
appl.mode.class = 'FlPDEC';
appl.dim = {'p','p.t'};
appl.name = 'PDE';
appl.shape = {'shlag(2,''p'')','shlag(2,''lm3'')'};
appl.gporder = {4,4};
appl.assignsuffix = '_PDE';
clear prop
clear weakconstr
weakconstr.value = 'off';%changed from ideal
weakconstr.dim = {'lm3','lm4'};
prop.weakconstr = weakconstr;
appl.prop = prop;
clear pnt
pnt.wcshape = 2;
pnt.ind = [1,1,1,1,1,1];
appl.pnt = pnt;
clear bnd
bnd.r = {0,0,'pin','pout'};
bnd.type = {'dir','neu','dir','dir'};
bnd.wcgporder = 2;
bnd.wcshape = 2;
bnd.ind = [1,1,3,2,2,1,4];
appl.bnd = bnd;
clear equ
equ.init = {0,-100000;0};
equ.wcgporder = 2;
equ.shape = 1;
equ.c = {1,'funcv*rhoair'};
equ.wcshape = 2;
equ.da = {1,0};
```

```
equ.f = –1,0″;
equ.usage = –0,1″;
equ.dinit = –0,–100;0″″;
equ.ind = [1,2];
appl.equ = equ;
fem.appl–3″ = appl;
fem.border = 1;
fem.outform = 'general';
fem.units = 'SI';

% Global expressions
fem.expr = –'funcv','2/((muair/K)+((muair/K)^2+4*Forch*rhoairlocal*absgradP)^0.5)', ...
  'rhoair','epsilon*p*28.8e-3/8.314/T2', ...
  'muair','(-7.887E-12*T2^2+4.427E-08*T2+5.204E-06)', ...
  'K',coeffs(54,trialx), ...
  'absgradP','(px^2+py^2)^0.5', ...
  'Forch',coeffs(53,trialx), ...
  'convect','hvol*(T2-T)', ...
  'airconvect','hvol*(T-T2)', ...
  'kair','10^(0.8616*log10(abs(T2))-3.7142)', ...
  'Cpair','0.0769*T2+1076.9', ...
  'funcDF','(2*(K/muair))/(1+(1+4*Forch*rhoairlocal*(K/muair)^2*absgradP)^0.5)', ...
  'velx','-funcv*px', ...
  'vely','-funcv*py', ...
  'hvol',vhvol, ...
  'epsilon',1-coeffs(11,trialx), ...
  'rhoairlocal','p*28.8e-3/8.314/T2', ...
  'Tairin',coeffs(42,trialx), ...
  'Tairout',coeffs(43,trialx), ...
  'Tfoamin','inletfit1*y^2+inletfit2*y+inletfit3', ...
  'Tfoamout',coeffs(41,trialx), ...
  'Tcopperin',coeffs(40,trialx), ...
  'Tcopperout',coeffs(41,trialx), ...
  'kfoam',coeffs(44,trialx), ...
  'rhofoam',coeffs(45,trialx), ...
  'Cpfoam',coeffs(46,trialx), ...
  'pin',coeffs(49,trialx), ...
  'pout',coeffs(50,trialx), ...
  'bottomflux',coeffs(52,trialx), ...
  'inletfit1',inletfit(1), ...
  'inletfit2',inletfit(2), ...
  'inletfit3',inletfit(3)″;


%inletfit(1)*'y'^2+inletfit(2)*'y'+inletfit(3) is the expression I want to
%use for Tfoamin


% Multiphysics
fem=multiphysics(fem);

% Extend mesh
fem.xmesh=meshextend(fem);

% Solve problem
fem.sol=femnlin(fem, ...
```

```
            'solcomp',–'T','p','T2'″, ...
            'outcomp',–'T','p','T2'″);

% fem.sol=femnlin(fem, ...
%              'solcomp',–'lm3','T','p','T2'″, ...
%              'outcomp',–'lm3','T','p','T2'″);

% Save current fem structure for restart purposes
fem0=fem;

%Collect output data
xcoordinates=[0 0.001  0.002  0.003  0.004  0.005  0.006  0.007  0.008  0.009  0.01
        0.011  0.012  0.013  0.014  0.015  0.016  0.017  0.018  0.019  0.02  0.021
        0.022  0.023  0.024  0.025  0.026  0.027  0.028  0.029  0.03  0.031  0.032
        0.033  0.034  0.035  0.036  0.037  0.038  0.039  0.04  0.041  0.042  0.043
        0.044  0.045  0.046  0.047  0.048  0.049  0.05  0.051  0.052];
ycoordinates=[0.0127  0.0127  0.0127  0.0127  0.0127  0.0127  0.0127  0.0127  0.0127  0.0127
        0.0127  0.0127  0.0127  0.0127  0.0127  0.0127  0.0127  0.0127  0.0127  0.0127  0.0127
        0.0127  0.0127  0.0127  0.0127  0.0127  0.0127  0.0127  0.0127  0.0127  0.0127  0.0127
        0.0127  0.0127  0.0127  0.0127  0.0127  0.0127  0.0127  0.0127  0.0127  0.0127  0.0127
        0.0127  0.0127  0.0127  0.0127  0.0127  0.0127  0.0127  0.0127  0.0127  0.0127];


n=0

if(Qstorage(trialx,1)==true)
    Qfilterederrors(trialx,1)=(postinterp(fem,'T2',[0;0.0127])-coeffs(31,trialx));
    n=n+1;
else
    Qfilterederrors(trialx,1)=0;
    n=n+0;
end

if(Qstorage(trialx,2)==true)
    Qfilterederrors(trialx,2)=(postinterp(fem,'T2',[0.0083;0.0127])-coeffs(32,trialx));
    n=n+1;
else
    Qfilterederrors(trialx,2)=0;
    n=n+0;
end

if(Qstorage(trialx,3)==true)
    Qfilterederrors(trialx,3)=(postinterp(fem,'T2',[0.0167;0.0127])-coeffs(33,trialx));
    n=n+1;
else
    Qfilterederrors(trialx,3)=0;
    n=n+0;
end

if(Qstorage(trialx,4)==true)
    Qfilterederrors(trialx,4)=(postinterp(fem,'T2',[0.0225;0.0127])-coeffs(34,trialx));
    n=n+1;
else
    Qfilterederrors(trialx,4)=0;
    n=n+0;
end
```

```
if(Qstorage(trialx,5)==true)
    Qfilterederrors(trialx,5)=(postinterp(fem,'T2',[0.0301;0.0127])-coeffs(35,trialx));
    n=n+1;
else
    Qfilterederrors(trialx,5)=0;
    n=n+0;
end

if(Qstorage(trialx,6)==true)
    Qfilterederrors(trialx,6)=(postinterp(fem,'T2',[0.0373;0.0127])-coeffs(36,trialx));
    n=n+1;
else
    Qfilterederrors(trialx,6)=0;
    n=n+0;
end

if(Qstorage(trialx,7)==true)
    Qfilterederrors(trialx,7)=(postinterp(fem,'T2',[0.0437;0.0127])-coeffs(37,trialx));
    n=n+1;
else
    Qfilterederrors(trialx,7)=0;
    n=n+0;
end

if(Qstorage(trialx,8)==true)
    Qfilterederrors(trialx,8)=(postinterp(fem,'T2',[0.0520;0.0127])-coeffs(38,trialx));
    n=n+1;
else
    Qfilterederrors(trialx,8)=0;
    n=n+0;
end


%Get SSE and MEAN AIR ERROR TEMPs
TestSSE=(Qfilterederrors(trialx,1))^2+(Qfilterederrors(trialx,2))^2+(Qfilterederrors(trialx,3))^2
+(Qfilterederrors(trialx,4))^2+(Qfilterederrors(trialx,5))^2+(Qfilterederrors(trialx,6))^2+(Qfiltere
derrors(trialx,7))^2+(Qfilterederrors(trialx,8))^2;
MeanExpErrTair=sum(Qfilterederrors(trialx,1:8))/n;
MeanExpTair=mean(coeffs([31:38],4));


TestSSR=0

if(Qstorage(trialx,1)==true)
   TestSSR=TestSSR+(Qfilterederrors(trialx,1)-MeanExpErrTair)^2;
else
    TestSSR=TestSSR+0;
end

if(Qstorage(trialx,2)==true)
   TestSSR=TestSSR+(Qfilterederrors(trialx,2)-MeanExpErrTair)^2;
else
    TestSSR=TestSSR+0;
end
```

```
if(Qstorage(trialx,3)==true)
   TestSSR=TestSSR+(Qfilterederrors(trialx,3)-MeanExpErrTair)^2;
else
    TestSSR=TestSSR+0;
end

if(Qstorage(trialx,4)==true)
   TestSSR=TestSSR+(Qfilterederrors(trialx,4)-MeanExpErrTair)^2;
else
    TestSSR=TestSSR+0;
end

if(Qstorage(trialx,5)==true)
   TestSSR=TestSSR+(Qfilterederrors(trialx,5)-MeanExpErrTair)^2;
else
    TestSSR=TestSSR+0;
end

if(Qstorage(trialx,6)==true)
   TestSSR=TestSSR+(Qfilterederrors(trialx,6)-MeanExpErrTair)^2;
else
    TestSSR=TestSSR+0;
end

if(Qstorage(trialx,7)==true)
   TestSSR=TestSSR+(Qfilterederrors(trialx,7)-MeanExpErrTair)^2;
else
    TestSSR=TestSSR+0;
end

if(Qstorage(trialx,8)==true)
   TestSSR=TestSSR+(Qfilterederrors(trialx,8)-MeanExpErrTair)^2;
else
    TestSSR=TestSSR+0;
end


TestSST=0

if(Qstorage(trialx,1)==true)
   TestSST=TestSST+(MeanExpTair-coeffs(31,trialx))^2;
else
    TestSST=TestSST+0;
end

if(Qstorage(trialx,2)==true)
   TestSST=TestSST+(MeanExpTair-coeffs(32,trialx))^2;
else
    TestSST=TestSST+0;
end

if(Qstorage(trialx,3)==true)
   TestSST=TestSST+(MeanExpTair-coeffs(33,trialx))^2;
else
    TestSST=TestSST+0;
end
```

```
if(Qstorage(trialx,4)==true)
   TestSST=TestSST+(MeanExpTair-coeffs(34,trialx))^2;
else
    TestSST=TestSST+0;
end

if(Qstorage(trialx,5)==true)
   TestSST=TestSST+(MeanExpTair-coeffs(35,trialx))^2;
else
    TestSST=TestSST+0;
end

if(Qstorage(trialx,6)==true)
   TestSST=TestSST+(MeanExpTair-coeffs(36,trialx))^2;
else
    TestSST=TestSST+0;
end

if(Qstorage(trialx,7)==true)
   TestSST=TestSST+(MeanExpTair-coeffs(37,trialx))^2;
else
    TestSST=TestSST+0;
end

if(Qstorage(trialx,8)==true)
   TestSST=TestSST+(MeanExpTair-coeffs(38,trialx))^2;
else
    TestSST=TestSST+0;
end

TestRSquare=TestSSR/TestSST;
TestMSRoMSE=TestSSR/(2-1)/TestSSE/(n-2);  %need to think this through: am I 2
parameters minus 1 and 8 data points minus 2 parameters?


AirTemp=postinterp(fem,'T2',[xcoordinates;ycoordinates]);
FoamTemp=postinterp(fem,'T',[xcoordinates;ycoordinates]);

vhvolStorageQ=[vhvolStorageQ;vhvol];
SSEStorageQ=[SSEStorageQ;TestSSE];
RSquareStorageQ=[RSquareStorageQ;TestRSquare];

%Local storage
SSETemp=[SSETemp;TestSSE];

AirTempStorageQ=[AirTempStorageQ;AirTemp];
FoamTempStorageQ=[FoamTempStorageQ;FoamTemp];



end

%Clunky labelling routine
AirTempStorageQ=[AirTempStorageQ;[coeffs(2,trialx) 0 0 0 0 0 0 0 0 0 0 0 0 0 0 0 0 0 0 0 0 0 0
0 0 0 0 0 0 0 0 0 0 0 0 0 0 0 0 0 0 0 0 0 0 0 0 0 0 0 0 0 0 0 0 0 0 0 0 0 0 0 0 0 0 0 0 0 0 0]];
```

```
FoamTempStorageQ=[FoamTempStorageQ;[coeffs(2,trialx) 0 0 0 0 0 0 0 0 0 0 0 0 0 0 0 0 0 0 0 0
0 0 0 0 0 0 0 0 0 0 0 0 0 0 0 0 0 0 0 0 0 0 0 0 0 0 0 0 0 0 0 0]];


SSEStorageQ=[SSEStorageQ;coeffs(2,trialx)];
RSquareStorageQ=[RSquareStorageQ;coeffs(2,trialx)];

%Tracking the location of the minimum SSE
[minSSE,indexminSSE]=min(SSETemp);
minSSEindexQ=[minSSEindexQ;indexminSSE];

%Loop through each experiment
end

%% Plot solution
%postplot(fem, ...
%         ’tridata’,–’T’,’cont’,’internal’”, ...
%         ’trimap’,’jet(1024)’, ...
%         ’title’,’Surface: Temperature  [K]’, ...
%         ’refine’,4, ...
%         ’axis’,[-0.0260812737642586,0.100938688212928,-0.0312500000000001,0.03125,-1,1]);
```

Appendix B: Deployment of a Reactive Metal Foam Monolith for Fuel Reforming

B 1 Deployment of a Reactive Metal Foam Monolith for Fuel Reforming

Depending on the type of monolith, the fabrication of a catalyst coated monolith is expected to follow one of the following sequences of processing/manufacturing steps:

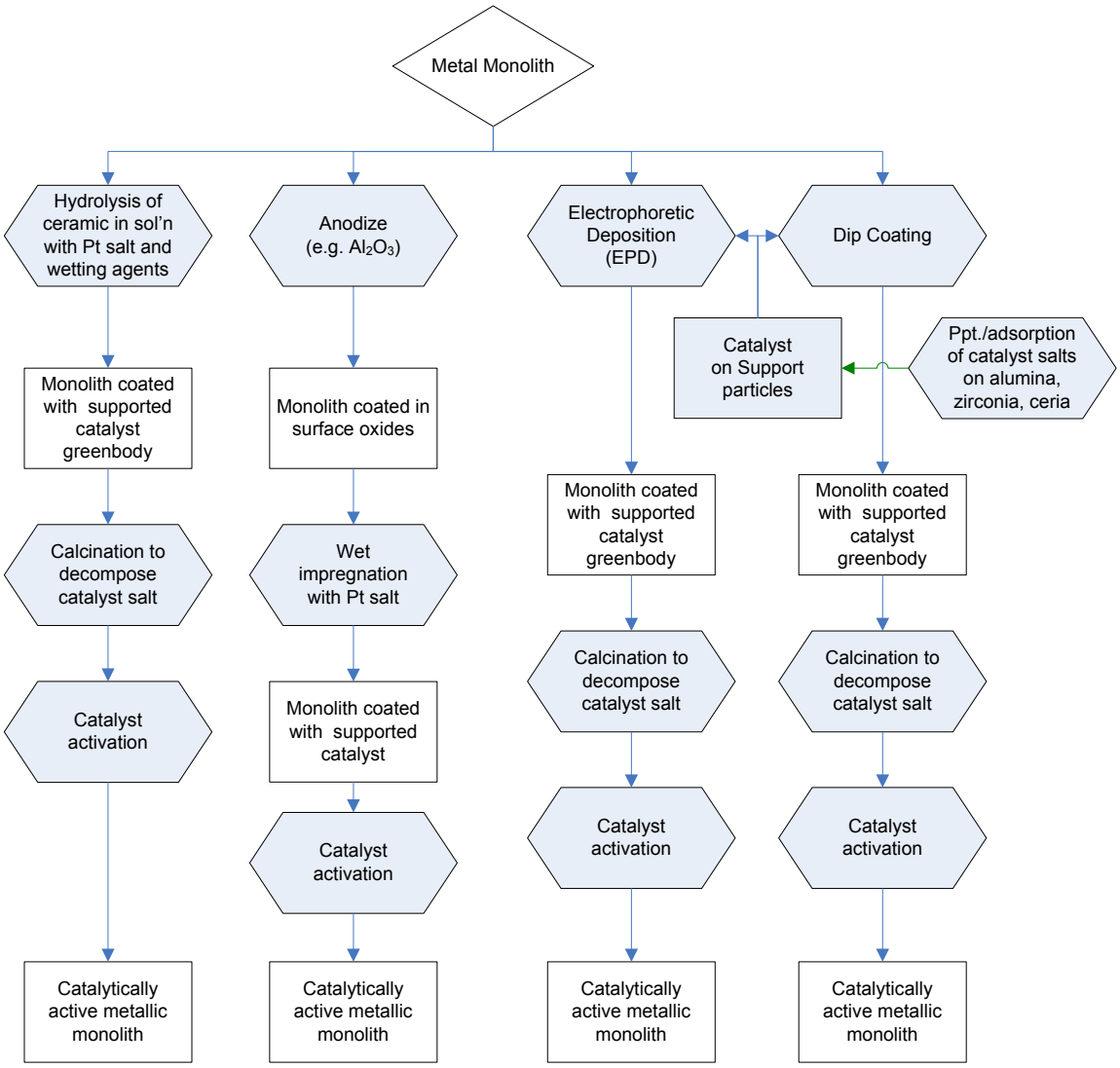

Figure 76: Sequence of steps for the production of catalytically active metallic monoliths. Processes are shown in shaded hexagonal entries and production artifacts in rectangular boxes.

As shown above, the nature of the monolithic substrate dictates the catalyst deployment methodology, which may involve one or more techniques such as dip coating, washcoating, electrophoretic deposition (EPD), wet impregnation or other chemical methods.

B.1.1 Catalyst Preparation

A suitable catalytically active material needs to be prepared before it is introduced onto the metallic monolith underneath. In this study, we have chosen Platinum as the active catalyst. Several methods of introducing platinum metal catalyst particles on to a ceramic support (Figure 77) are discussed. The combined platinum/support can then be used to coat the monolith.

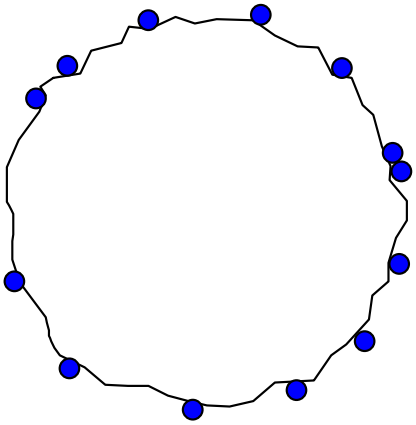

Figure 77: Schematic representation of platinum catalyst nanoparticles (blue) supported on a single ceramic particle (white).

B 1.1.1 Wet Impregnation

Wet impregnation processes are one of the simplest methods of deploying nano-particle catalysts to an underlying support. Wet impregnation relies on the direct physisorption of complex salts to the support surface (e.g., alumina, ceria, zirconia). The salts are then treated in place to leave only the catalytically active metal adsorbed on the support.

Alumina particles are amphoteric, exhibiting substantial charge separation. When alumina particles are placed in aqueous medium, their isoelectric point resides between pH of 4-6.

Dropping the pH to 2 leads to substantial charge separation, which provides some electrostatic attraction between the alumina surface and a negatively charged $\left[HPtCl_6\right]^{-1}$ anion. Nitric acid may be used to keep aqueous suspensions of alumina below the isoelectric point. Dihydrogen hexachloroplatinic acid (CPA,$\left[H_2PtCl_6\right]$) is then introduced into the solution and mixed until $\left[HPtCl_6\right]^{-1}$ anions adsorb onto free alumina surfaces. After drying the alumina with CPA particles on its surface, the supported salt is calcined at 600˚C to decompose the CPA, leaving small particles of agglomerated PtO_2 on the surface. The supported oxide is subsequently reduced to its active form in a packed bed reactor.

One complication of using wet impregnation on a pre-coated aluminium monolith is the reactivity of the metal with CPA to create $AlCl_3$. Since the ceramic coatings are porous, it is not possible to prevent this reaction in such cases – rendering wet-impregnation impractical for this application.

B 1.1.2 Co-reduction and Precipitation Method (Watanabe Method)

A process for the co-reduction and precipitation of finely dispersed platinum-ruthenium catalyst alloy supported on carbon black was described by Watanabe *et al [96]*. The procedure relies on the chemical reduction of the noble metal salts and their subsequent precipitation as surface-bound oxides on the carbon supports.

A modified version of Watanabe's process for co-precipitation of $PtRu$ catalysts on carbon has been applied to take advantage of an acidic byproduct in the sodium bisulfite reduction of CPA. Performing this two-step reduction of the platinum salt in the presence of alumina allows the physisorption of the platinum-sulfite salt prior to its oxidation to PtO_2. The aqueous medium drops well below the isoelectric point of alumina and the recovered ceramic support can be dried, calcined and reduced to activate the platinum catalyst. The activity of the dried, supported catalyst has been observed experimentally.

The key reaction steps of the platinum precipitation method are outlined below:

i. $$H_2PtCl_6 + 3\ NaHSO_2 + H_2O \rightleftharpoons H_3Pt\left(SO_3\right)_2 OH + Na_2SO_4 + NaCl + 5\ HCl$$

ii. $$H_3Pt\left(SO_3\right)_2 OH + 3\ H_2O_2 \rightleftharpoons PtO_2 + 3\ H_2O\ + 2\ H_2SO_4$$

B1.1.3 Modified Watanabe Method

Further modifications of Watanabe's process may allow for a nanoparticulate binary alloy of PtRu on alumina, ceria, zirconia, etc. The binary alloy would suffer less carbon-monoxide poisoning at low temperatures than platinum-only catalysts.

B 1.2 Catalyst Support Coating

This section describes methods for coating of ceramic support or coating of catalyst dispersed on ceramic support.

The most successful method of ceramic coating for flattened woven meshes has thus far been electrophoretic deposition (EPD). Modestly successful results for foam coating have been achieved by covering monoliths with a liquid-phase ceramic precursor, such as zirconium n-propoxide. An attempt was also made to oxidize a thin-layer of Al_2O_3 onto a high-purity aluminium electrode in mildly caustic solution by applying a potential of 73 V in sodium pentaborate (0.01 M). For monoliths below 60 ppi porosity, spray coating of catalyst/support particles onto the surface with subsequent calcination proved practical. For monoliths below 40 ppi, dip coating of ceramic particles onto the surface worked well.

B 1.2.1 Electrophoretic Deposition (EPD)

Basic Principle: Electrophoresis is the movement of suspended particles through a fluid due to the application of an electric field. The stable surface charge on the particles experience a force in the field, and the particles must accelerate to balance that force. In almost all cases the particles reach terminal velocity within a few microns of their rest position. As a consequence, an even flux of solid particles can be made to flow inside the electric field between an anode and cathode. In a

non-conducting solution with a potential applied between these electrodes, the uni-directional flux of solid particles can be used to coat one of these electrodes. This process is called electrophoretic deposition (EPD).

Results: Experiments were carried out by applying a 20 V potential across two electrodes in a suspension of α-alumina in ethanol. Attempts to coat metal foams failed because of the the Faraday cage effect, which prevents an electric field from penetrating deeper than a thickness of $\cong 1$ open cell. It may be possible to penetrate deeper with higher voltages. EPD was successfully applied to to coat metal microchannel monoliths [97] and metal mesh. A picture of stainless steel mesh coated with alumina is shown in Figure 78 below. While EPD offers superior coating control, it may only be suitable for monoliths with a nearly two-dimensional profile. Attempts to conform a freshly-coated two-dimensional monolith into a three-dimensional profile will be limited by the mechanical resistance of the ceramic green body to cracking and flaking.

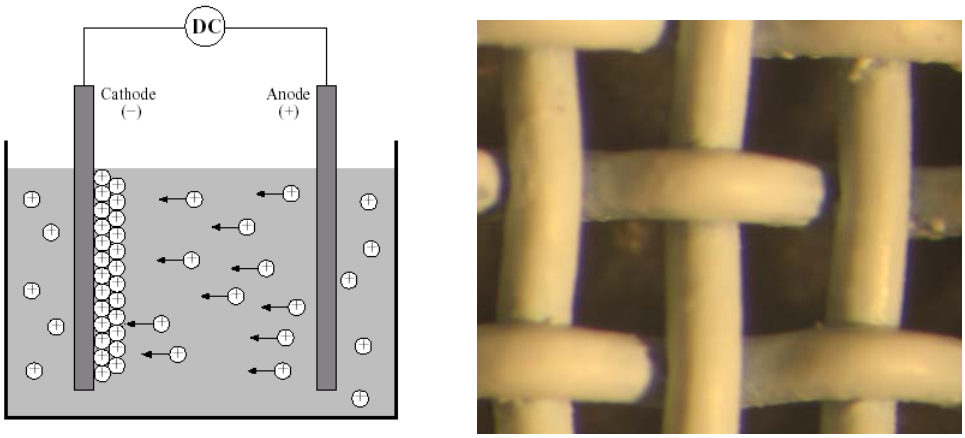

Figure 78: Left (Taken from Lankin, M. [98]): electrophoretic deposition of suspended surface-positive ceramic particles on a direct-current cathode in a non-conducting fluid. Right: 100× magnification of an 80 ppi stainless steel mesh coated in an approximately 5 micron-thick EPD coating of α-alumina.

B 1.2.2 In-Situ Reactive Coating (Alkoxide Hydrolysis)

Basic Principle: The method of in-situ reactive coating allows coating of a bare monolith with ceramic support and the active catalyst in a single step. The method uses a solution of ceramic precursor, medium-weight alcohol diluent and the platinum salt. Subsequent hydrolysis precipitates the nanoparticle ceramic, while the platinum salt is entrained. Subsequent heating

hardens the coating and decomposes the catalyst salt to an oxide. The precursor hydrolyzes spontaneously in the presence of water, precipitating nano-scale zirconia particles. If the hydrolysis takes place on the monolith surface, subsequent calcination or sintering can be used to form the ceramic as an outer shell. For an n-propoxide, the hydrolysis reaction follows:

i. $$Zr\left(O\left(CH_2\right)_2 CH_3\right)_4 + H2O \rightleftharpoons ZrO\left(O\left(CH_2\right)_2 CH_3\right)_2 + 2\left(\left(CH_2\right)_2 CH_3OH\right)$$

ii. $$ZrO\left(O\left(CH_2\right)_2 CH_3\right)_2 \rightleftharpoons ZrO_2 + Zr\left(O\left(C_2H\right)_2 CH_3\right)_4$$

Results: Liquid coatings of propanol and zirconium(IV) n-propoxide were hydrolyzed on foam and mesh monoliths with either steam or ambient moisture. The method yielded even, thin coatings on very large porous structures (20 ppi), whose pore dimensions allow for proper wetting with viscous precursor. Smaller pore monoliths (40 ppi) were also successfully coated with ambient hydrolysis. Several attempts have been made to coat 80 ppi open cell nickel foams and 80 ppi steel woven meshes this way (precursor has been diluted with excess propanol in these cases). Insufficient surface wetting has prevented effective monolith coating on the 80 ppi monoliths.

An alternative application method under consideration is to entrain the volatile precursor compound in a recirculating stream of inert gas, flow the mixture through the monolith and inject small amounts of steam into the flow stream as it passes through the monolith. Another alternative is the use of forced flow of the precursor solvent through the monolith, similar to a washcoating approach, relying on periodic exposure to air to complete hydrolysis in stages.

If a suitable non-reacting surfactant can be found to allow full wetting of the microporous foams and woven meshes (80-100 ppi), it will be possible to take advantage of the non-reactive solubility of dihydrogen hexachloroplatinic acid (H_2PtCl_6) in low-weight alcohols. A combined solution of catalyst salt, wetting agent, propanol solvent and ceramic precursor would allow for one-step monolith coating. The active catalyst could be recovered by calcining at 600□C. These

temperatures will decompose the platinum salt and the wetting agent, leaving PtO_2, which can be reduced to full activity in the working reactor.

B 1.2.3 Electro-Oxidation

Basic Principle: Electro-oxidation of aluminium is a convenient method of generating $\gamma - Al_2O_3$, a suitable support for Pt/PtO_2. The catalyst support layer can be generated by electrochemical surface oxidation to generate aluminium oxide. Sulka *et al* [99] have succeeded in using this method to create well ordered, porous, thin-layers on alumina samples, although these thin-layers have not been tested for suitability as supports for noble metal catalysts.

Results: Robust 76-micron thick oxide coatings for aluminium substrates were achieved with Type III (black finish) anodization of the bare aluminium foams (ERG anodization). The micro-porosity of such layers is not fully understood, but in principle, it is possible to maintain enough porosity to provide sufficient catalyst adhesion (and active surface area) to service a working metal-foam reactor.

B 1.2.4 Spray Coating

Basic Principle: Spray coating involves dusting the monoliths with a fine cloud of electrostatically charged ceramic/catalyst particles generated by an atomizer/spray gun. The particles can be suspended in suitable medium, e.g., alcohol, and expanded through a Venturi-tube type sprayer. Using a heat gun, the deposited particles can be rapidly dried. Further, the sample can be rotated about two axes to promote even coating. Once coated with a ceramic green-body, the monolith is calcined or sintered to harden the ceramic in place.

Results: Spray coating has proven to be a viable method for depositing catalyst on larger-pore monoliths of the 10-20 ppi range. Suspensions of Pt/Al_2O_3 in ethanol will coat the monoliths internal surfaces, but without the same uniform thicknesses as EPD or alkoxide hydrolysis methods. Spray coating also leads to significant wasted material, especially if the spray coat suspension is already supporting a catalyst.

B 1.2.5 Dip coating

Basic Principle: For this method, the ceramic is suspended in viscous glycerol and the monolith is dipped in the suspension and withdrawn at a slow rate. The suspension is dried under a lamp at approx. 90°C for 10 hours prior to calcination at 450°C for 12 hours to burn off organics.

Results: Dip coating of ceramic particles onto the surface of aluminium foams were attempted. Coatings of up to 20% of the monolith mass were achieved. The problem with dip coating in this manner is the effect on the geometry of the monolith microstructure. Viscous dipping suspensions did not fully wet the monolith surface and tended to round out junctions between individual pores (Figure 79). This led to uneven layering that should affect convective flows over the monolith. While not necessarily a drawback for industrial applications, this kind of coating could severely complicate an experimental program.

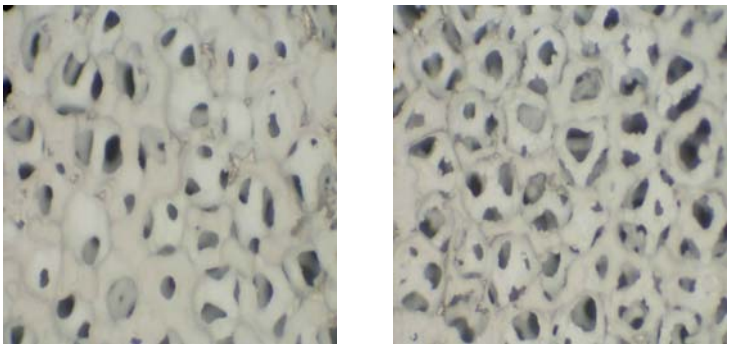

Figure 79: 40 ppi aluminium foam monoliths dip-coated in a glycerol-alumina suspension. Left, the wet green-body exhibits pooling around the edges of the cell monoliths. Right: the dried, calcined foam is coated unevenly with thickened regions where the wet green-body had pooled.

B 1.3 Post-Coating Treatments

In all catalyst coating methods in Section B 1.2, the initial "greenbody" of wet ceramic support and catalyst must be treated to activate the catalysts. The catalyst salts must be decomposed to a reducible form (e.g., PtO_2, in the case of platinum salts) and the ceramic must be hardened in place so that it will be strong enough for repeated use.

The decomposition of platinum is carried out in an open furnace at 450-500ºC for 8-12 hours. These temperatures are sufficient to bake the ceramic greenbody in place, but not hot enough to sinter it (heating to the point that individual ceramic particles adhere to each other). Although it is possible to reach sintering temperatures on metals like steel or nickel, there is a strong likelihood of also sintering catalyst particles together at such high temperatures, reducing activity substantially.

A significant consideration in the calcination-sintering treatment of these monoliths is the balance between the desired thermal heat transfer of the metal and its compatibility with high-temperature ceramic treatments and catalyst calcinations (Figure 80). A low-thermal-expansion-coefficient monolith like nickel is easily coated with calcined ceramics, but it will have much lower thermal conductivity than a high-expansion coefficient material like copper. Many aluminium alloys cannot tolerate temperatures higher than 550ºC.

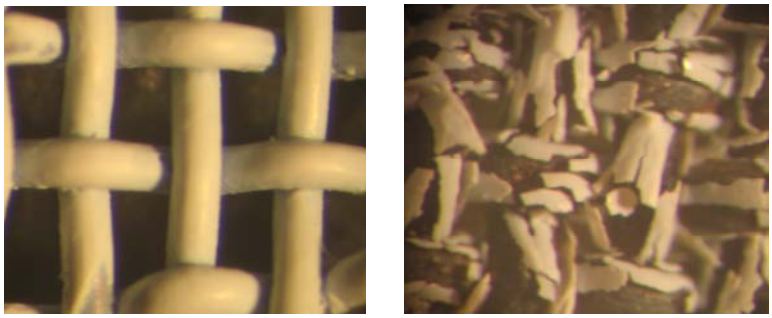

Figure 80: An 80 ppi stainless steel mesh before and after calcinations at 850 °C (raised at 2 °C/min.) Left: the green-body coating of alumina, deposited by EPD. Right: incompatible coefficients of thermal expansion between the steel and ceramic have shattered the coating.

Appendix C: Testing and Characterization of Catalyst

C 1.1 Catalyst Performance Criteria

A model reaction, methanol decomposition, has been chosen to validate and characterize the performance of catalyst for metal monoliths.

$$CH_3OH \longrightarrow 2H_2 + CO$$

The reaction has been chosen for its relative simplicity and low ratio of byproducts in the absence of water. The simple stoichiometry allows yield and selectivity analysis through the monitoring of carbon monoxide via gas chromatography or mass spectrometry.

The performance metrics of a reactive monolith are:

- Catalytic activity and deactivation (population of active catalytic sites)
- Reaction kinetics (activation energy and effective rate law)
- Selectivity of hydrogen over other side products

C 1.2 In-situ Reaction Conversion Testing

Experimental Procedure: The experimental procedure involves placing a catalyst coated cylindrical monoliths into an 8 mm ID quartz tube housed in a steel tube with a sealed fuel feed and exhaust. The entire assembly is placed in an oven. Methanol is fed to the reactor via a syringe pump and a tube loop inside the oven allows the methanol to volatilize before it enters the feed end of the reactor. Reaction products, byproducts and waste are removed through the exhaust end and any condensable wastes are collected before the remaining gas stream is fed to an in-line gas chromatography apparatus.

The resulting signal intensity can be used to determine carbon monoxide concentration in the exhaust stream (against a known standard). Conversion can be calculated at a range of temperatures to generate a "light off" curve relating catalyst activity to temperature. Loss in

conversion over time can be used to characterize catalyst degradation for a specific operating condition.

The test was performed with 7g of activated Pt/Al_2O_3 catalyst packed in a quartz tube which was loaded into a temperature-controlled oven. A methanol feed of 0.8 $\mu L/min$ was introduced into one end of the tube and the system was brought to thermal equilibrium.

Results: Methanol conversion experiments have been conducted, both on a packed bed of 1% Pt/Al_2O_3 and a spray coated 40 ppi aluminium foam monolith (Figure 81). The 3.8 cm^3 coated monolith has converted methanol with vapour phase flow rates of up to 1.35 $mL/\min$. We are currently focusing on stabilizing our gas separator to remove unacceptable noise from results. For a dedicated flow rate of 0.8 $\mu L/min$, conversion ranging from approximately 50-60% was observed in the temperature range between 152-177°C. The reaction appeared to light-off at approximately 150°C (Figure 11) [100]. Experimental results differed slightly from those of Imamura et al. for the similar test on a 2% Pt/CeO_2 [101].

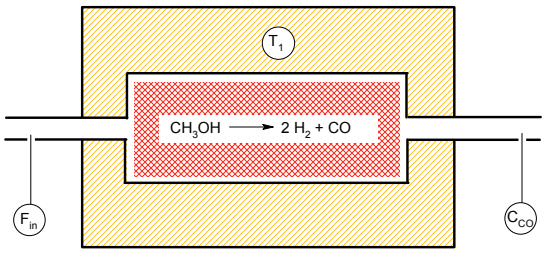

Figure 81: Apparatus for conversion of a methanol vapour stream to carbon monoxide and hydrogen gas. Typically, flow is delivered to provide 20 seconds mean residence time for unreacted species.

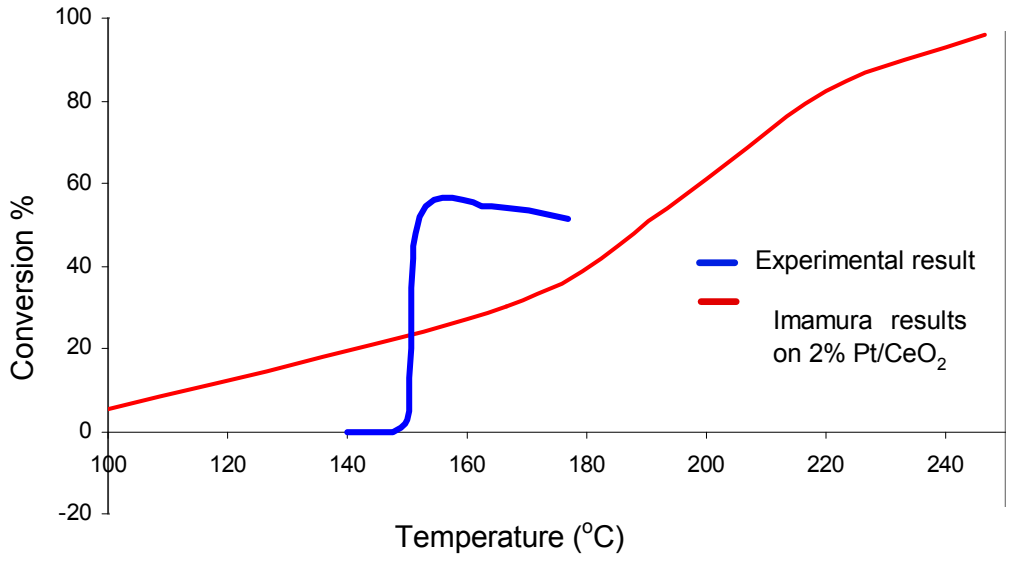

Figure 82: Comparison of experimental conversion (packed bed) vs. temperature data to Imamura et al. The light-off curve for the Pt/Al2O3 catalyst is much steeper than that for the Pt/CeO2 catalyst used by Imamura et al. [101]

C 1.3 Active Catalyst Surface Area

Basic Principle: The conversion efficiency of the catalyst needs to be correlated to its active surface area. Determination of active area can be accomplished by exposing the catalyst to pure carbon monoxide gas. At low temperatures, the gas will spontaneously adsorb onto any exposed platinum particle as a monolayer, but will not adsorb to the underlying ceramic support. As the gas is heated up, the desorption threshold will be reached. Measurement of the amount of gas desorbed over a temperature programmed desorption (TPD) will directly correlate to the exposed area of active platinum catalyst. Reductions in the strength of the integrated TCD signal will be related to deactivation mechanisms such as coking or platinum sintering.

Likewise, the total surface area of catalyst support on the same sample can be determined by adsorbing multiple layers of cold nitrogen gas on all surfaces at low temperature and desorbing at higher temperatures. The Brunauer Emmett and Teller (BET) method can be used to infer a total available surface area. Subtracting the TPD area of the catalyst gives the total area of the ceramic support.

A catalyst characterization test station (In-Situ RIG 150) with temperature programmed desorption (TPD) capability is available at Queen's University. The In-Situ RIG-150 unit is currently awaiting maintenance on a gas-flow valve. The same device is also capable of temperature programmed desorption (TPD) on an in-situ packed bed. TPD experiments for the adsorption-desorption of carbon monoxide on platinum and platinum-ruthenium catalysts could, in principle, determine active surface areas on a fully coated monolith provided that there was a large enough catalyst sample to provide a signal. The sample size required would be quite large, so an oversize sample chamber must be fabricated for this purpose.